Probing electronic phase transitions with phonons via inelastic neutron scattering: superconductivity in borocarbides, charge and magnetic order in manganites

Zur Erlangung des akademischen Grades eines
DOKTORS DER NATURWISSENSCHAFTEN
von der Fakultät für Physik der
Universität Karlsruhe (TH)

genehmigte

DISSERTATION

von
Dipl.-Phys. Frank Weber
aus Pforzheim im Enzkreis

Tag der mündlichen Prüfung: 2. November 2007
Referent: Prof. Dr. H. v. Löhneysen
Korreferent: Prof. Dr. E. Dormann

Abstract

The present thesis concentrates on the signatures of strong electron-phonon coupling in phonon properties measured by inelastic neutron scattering. The inelastic neutron scattering experiments were performed on the triple-axis spectrometers 1T and DAS PUMA at the research reactors in Saclay (France) and Munich (Germany), respectively. The work is subdivided into two separate chapters:

In the first part, we report measurements of the lattice dynamical properties, i.e. phonon frequency, linewidth and intensity, of the conventional, i.e. phonon-mediated, superconductor YNi_2B_2C of the rare-earth-borocarbid family. The detailed check of theoretical predictions for these properties, which were calculated in the theory group of our institute, was one major goal of this work. We measured phonons in the normal state, i.e. $T > T_c$, for several high symmetry directions up to 70 meV. In general, we found good agreement with the calculations for most of the measured phonon frequencies and linewidths. Only for two strong-coupling acoustic phonon branches we observed large deviations in the frequencies (for one of them) and in the phonon linewidths (both). The measured phonon intensities in different Brillouin zone also agree well with the theory.

Our study of the change of the phonon lineshape of strong coupling phonons on entering the superconducting state verifies a theory proposed by P. B. Allen et al. in 1997 in a semi-quantitative manner. We were able to extract the full temperature dependence of the superconducting energy gap $2\Delta(T)$ from our phonon scans with such accuracy that even deviations from the weak coupling BCS behaviour could be clearly observed. By measuring phonons at different wave vectors we demonstrated that phonons are sensitive to the gap anisotropy under the precondition, that different phonons get their coupling strength from different parts of the Fermi surface.

In the second part, we investigated the properties of Mn-O bond-stretching phonons in the bilayer manganite $La_{2-2x}Sr_{1+2x}Mn_2O_7$. At the doping level $x = 0.38$ this compound has an ferromagnetic groundstate and exhibits the so-called colossal magnetoresistance effect in the vicinity of the Curie temperature T_C. The atomic displacement patterns of the investigated phonons closely resemble possible Jahn-Teller distortions of the MnO_6 octahedra, which are introduced in this compound by the Jahn-Teller active Mn^{3+} ions. We observed strong renormalizations of the phonon frequencies and clear peaks of the intrinsic phonon linewidth near the order wave vector of the short-range charge and orbital order present above T_C. This low temperature effects are interpreted as precursors to the above mentioned short-range order at higher temperatures.

In an neutron powder diffraction measurement at the Hahn-Meitner Institut in Berlin, we investigated the temperature dependence of the anisotropic Debye-Waller factors of the oxygen atoms in $La_{0.7}Sr_{0.3}MnO_3$. According to the present point of view, the sudden increase of the Debye-Waller factors at T_C should be proportional to the strength of the colossal magnetoresistance effect. However, we found experimental values for $La_{0.7}Sr_{0.3}MnO_3$, which are in close vicinity or even bigger than values of compounds with a much stronger magnetoresistance effect.

Untersuchung elektronischer Phasenübergänge mit Phononen mittels inelastischer Neutronenstreuung: Supraleitung in Borokarbiden, Ladungs- und magnetische Ordnung in Manganaten

Zusammenfassung

Die vorliegende Arbeit beschäftigt sich mit den Effekten von starker Elektron-Phonon Kopplung in Messungen der Phononeneigenschaften. Phononen wurden gemessen mittels inelastischer Neutronenstreuung auf den 3-Achsen Spektrometern 1T und DAS PUMA an den Forschungsreaktoren in Saclay (Frankreich) und München (Deutschland). Die Arbeit ist in zwei voneinander unabhängige Teile gegliedert:
Im ersten Teil werden die gitterdynamischen Eigenschaften, d.h. Phononenfrequenz, -linienbreite und -intensität, eines konventionellen Supraleiters untersucht. Die detaillierte Überprüfung der von der Theoriegruppe unseres Instituts angefertigten theoretischen Vorhersagen der gitterdynamischen Eigenschaften des Supraleiters YNi_2B_2C aus der Seltenerd-Borokarbidfamilie war eines der vorrangigen Ziele dieser Arbeit. Für die hier vorliegende Arbeit wurden Phononen in verschiedenen kristallographischen Richtungen mit Energien bis zu 70 meV gemessen. Die experimentellen Werte zeigen eine im allgemeinen gute Übereinstimmung mit den gerechneten Ergebnissen für die Frequenz und Linienbreite der Phononen. Nur für zwei extrem stark koppelnde akkustische Phononen gibt es für eines eine deutliche Abweichung in der Frequenz bzw. für beide unterschätzte Linienbreiten. Die Vorhersagen für die Phononenintensitäten in verschiedenen Brillouin Zonen wurden ebenfalls gut bestätigt.
Die Untersuchung der Änderung der Phononenlinienform von stark koppelnden Phononen bei Eintritt in den supraleitenden Zustand bestätigte eine von P. B. Allen 1997 veröffentlichte Theorie in semi-quantitativer Weise. Die volle Temperaturabhängigkeit der supraleitenden Energielücke konnte aus den Phononendaten mit einer Genauigkeit ermittelt werden, dass sogar Abweichungen vom schwach-koppelndem BCS-Verhalten bestimmt werden konnten. Die Messungen ergaben, dass mit Phononen, gemessen an unterschiedlichen Punkten der Brillouin Zone, die Anisotropie der supraleitenden Energielücke gezeigt werden kann, vorausgesetzt die Phononen beziehen ihre Kopplung aus unterschiedlichen Bereichen der Fermi-Fläche.

Der zweite Teil behandelt die anomalen Eigenschaften der Mn-O Streckschwingungen in dem Zweischicht-Manganat $La_{2-2x}Sr_{1+2x}Mn_2O_7$. In der hier untersuchten Dotierung ($x = 0.38$) hat dieses Material einen ferromagnetischen Grundzustand und zeigt den sogenannten kolossalen Magnetwiderstandeffekt in der Nähe der Curie-Temperatur T_C. Die untersuchten Phononen ähneln in ihren Auslenkungsmustern möglichen Jahn-Teller Verzerrungen der MnO_6 Oktaeder, welche durch das Jahn-Teller aktive Mn^{3+} Ion eingeführt werden. Wir konnten starke Renormalisierungseffekte der Phononenfrequenzen und ein Maximum der Phononenlinienbreiten im Bereich des Ordnungsvektors der oberhalb von T_C auftretenden kurzreichweitigen Ladungs-/Orbitalordnung, $\mathbf{q} = (0.25, 0.25, 0)$, feststellen. Die Tieftemperatureffekte werden als Vorläufereffekte ('precursor') dieser kurzreichweitigen Ordnung in der Hochtemperaturphase interpretiert.

In einem Pulverdiffraktionsexperiment am Hahn-Meitner Institut in Berlin wurde die Temperaturabhängigkeit der anisotropen Debye-Waller Faktoren der Sauerstoffatoms in $La_{0.7}Sr_{0.3}MnO_3$ untersucht. Nach der aktuellen Sichtweise, sollte der plötzliche Anstieg dieser Werte bei T_C proportional zur Stärke des kolossalen Magnetwiderstandeffekts sein. Die experimentellen Werte für $La_{0.7}Sr_{0.3}MnO_3$ liegen jedoch in direkter Nachbarschaft und sind teilweise sogar grösser als in anderen Manganaten, die einen deutlich stärkeren Magnetwiderstandseffekt zeigen.

Contents

1 Introduction

Superconductivity was discovered by H. K. Onnes in 1911 during a study of the electrical resistivity of solid mercury [1]. The microscopic description was given nearly 50 years later by Bardeen, Cooper and Schrieffer in 1957 [2]. In their theory, an attractive potential leads to the formation of pairs of electrons, the so-called Cooper pairs, which are the superconducting charge carriers. For the superconductors known at that time, the origin of the attractive potential was found to be the electron-phonon coupling. However, the calculation of the superconducting transition temperature T_c from first principles has not been possible. Very recently, however, progress in density functional theory (DFT) allows one to calculate the phonon spectrum and the electron-phonon coupling strength of metals and intermetallic compounds from first principles. From these results, T_c can be finally calculated from first principles as well. In this work, we embarked on an experimental study of the phonon properties of a conventional, i.e. phonon-mediated, superconductor, for which the theoretical results were already available, to check the theoretical predictions in detail. The compound studied is YNi_2B_2C, which is an interesting candidate for such an investigation, as macroscopic measurements indicate a strong gap anisotropy of $\Delta_{max}/\Delta_{min} \approx 10$ or even larger, which would be unprecedented in phonon-mediated superconductors.
During the investigation of the lattice dynamical properties of YNi_2B_2C we observed strong changes in the phonon lineshapes on entering the superconducting state. Investigating this issue further, it developed into a project in its own right, involving very interesting physical phenomena, which had not been studied in any detail before in any compound.

The dramatic drop in electrical resistivity on applying a magnetic field, which is observed in several ferromagnetic manganites and related compounds, was named colossal magnetoresistance (CMR). It is maximum near the Curie temperature T_C of these materials. In certain compounds, a reduction of the resistivity of up to three orders of magnitude was observed. In the CMR manganites the distortion of the MnO_6 octahedra caused by the Jahn-Teller activity of the Mn^{3+} ion naturally couples the electronic and the lattice degrees of freedom. The present theoretical point of view is that above T_C, the charge carriers are self-trapped by creating localized lattice distortions of the Jahn-Teller type, called polarons.
A stringent check of formation of such polarons can be made by measuring the temperature dependence and absolute size of the atomic mean square displacements $\langle \widehat{u}^2 \rangle$ in CMR materials, which was done in this work for $La_{0.7}Sr_{0.3}MnO_3$. This compound is presently viewed as a candidate with no polaron formation, but as we will show, shows

evidence for polaron formation to the same extent as other CMR manganites.
A second topic was an inelastic neutron scattering investigation of phonon anomalies in a well known CMR compound, the bilayer manganite $La_{1.24}Sr_{1.76}Mn_2O_7$. Our aim was to link the phonon anomalies showing up at low temperatures, i.e. in the ferromagnetic state, with the short range charge/orbital order appearing above T_C known from previous studies.

2 Experimental methods

After the discovery of the neutron in 1932 by J. Chadwick, it was shown that neutrons could be Bragg diffracted by solids four years later (see ref. [3]). In the early years limited by the low neutron flux from Ra-Be sources, even inelastic scattering studies have become possible after the construction of the high-flux reactors built in the 1970s and later on. The techniques and theory of neutron scattering are widely discussed in several books [4–7]. Therefore only the basic properties of the neutron will be discussed in chapter 2.1. The instruments used for this study are described in chapters 2.2 to 2.3.

2.1 Neutrons as a probe in condensed matter physics

The neutron is an ideal tool to study condensed matter due to its unique physical properties, of which some are listed in table 2.1. Due to these properties there are four main points describing the abilities of neutron scattering:

- The de Broglie wavelength of a thermal neutron (see tab. 2.1) is similar to the atomic distances in liquids and solids and therefore interference effects are observable.

- With zero charge the neutron can penetrate deep into the sample and thus probes bulk properties.

- The energy of thermal neutrons is in the range of many of the excitations in condensed matter. Thus the neutron is appropriate to study these excitations in condensed matter.

- With its spin magnetic moment the neutron can also be scattered by magnetic excitations and can probe the magnetic structure and dynamics of the sample.

The energies of neutrons coming directly from the core of a reactor are too high to be useful in condensed matter physics. They are moderated by heavy water (thermal neutrons), liquid H_2 or CH_4 (cold neutrons) or a hot massive block, for example made of graphite and heated to $T = 2400\,\mathrm{K}$ at ILL, Grenoble (hot neutrons). The typical useful energy of thermal neutrons is $5 - 100\,\mathrm{meV}$, for cold ones $0.1 - 10\,\mathrm{meV}$. Hot neutrons at $T = 2400\,\mathrm{K}$ have their maximum of intensity at $E \approx 200\,\mathrm{meV}$.

Quantity	value
mass m	$1.675 \cdot 10^{-27}\,\mathrm{kg}$
charge	0
spin	$\frac{1}{2}$
magnetic dipol moment μ_n	$-1.913 \cdot \mu_N$
standard velocity v_{st}	$2.20\,\mathrm{km/s}$
energy E_{st}	$25.3\,\mathrm{meV}$
wave length λ_{st}	$1.798\,\text{Å}$
wave vector k_{st}	$3.49\,\text{Å}^{-1}$
temperature T_{st}	$293\,\mathrm{K}$

Table 2.1: Basic properties and values of thermal neutrons ($T = 293\,\mathrm{K}$, st: standard value)

2.2 Inelastic neutron scattering

2.2.1 Triple-axis spectrometer

A triple axis spectrometer (TAS) is a very versatile and useful instrument in neutron scattering. It allows one to probe excitations in energy and momentum space in a controlled manner. The concept was developed by B. N. Brockhouse (1961) at Chalk River in Canada [8]. He was awarded a Nobel Prize in physics in 1994 together with C. Shull for "their pioneering contributions to the development of neutron scattering techniques for the study of liquid and solid matter" [9]. With its unique properties it is used for both, elastic and inelastic scattering.

Elements

In fig. 2.1 the course of the neutron beam and the main devices of the 1T thermal TAS located at the ORPHEE reactor, Laboratoire Léon Brillouin (LLB) are shown (photograph in fig. 2.2). The eponymous three axes are the monochromator axis, the sample axis and finally the analyzer axis. By an appropriate setting of the corresponding angles one can in principle reach every point in momentum space at any transfer energies. Apart from the source, usually a nuclear reactor, the monochromator crystal is the most important element of a TAS concerning the neutron intensity. It selects a specific neutron wavelength λ_i from the incident white beam by Bragg diffraction from a given set of lattice plans. Starting from Bragg's law

$$G_{hkl} = 2ksin\,\Theta_B, \tag{2.1}$$

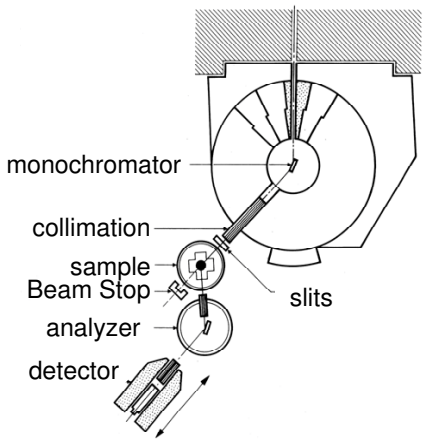

Figure 2.1: Schematic view of the 1T TAS at the ORPHEE reactor at LLB, CE Saclay, France.

Figure 2.2: Photography of the 1T TAS at the ORPHEE reactor at LLB, CE Saclay, France.

the selected wavelength of the neutron is given by

$$\lambda = 2d_{hkl} sin\,\Theta_B \tag{2.2}$$

where $G_{hkl} = \frac{2\pi}{d_{hkl}}$ with d_{hkl} the lattice spacing of the planes indicated by the Miller indices h, k, l. $k = \frac{2\pi}{\lambda}$ is the wavevector of the selected neutron and Θ_B the scattering angle. In order to get higher beam intensities the monochromator crystal usually consists of several small single crystals with a relatively broad mosaic spread, which are arranged with an adjustable curvature to focus all the neutron intensity onto the position of the sample. Modern TASs employ monochromator and analyzer crystals which are focusing both horizontally and vertically (doubly focusing). Some materials which are used as monochromator crystals are characterized in table 2.2. For inelastic neutron scattering measurements, the sample itself is normally mounted on a two-circle goniometer, which allows rotations about two orthogonal axes in the scattering plane. Additionally, horizontal movements are possible to center the sample position according to the neutron beam. For neutron experiments involving a cryostat or a magnet, a single-crystal sample is placed in an aluminium can filled with He gas providing good thermal contact to the cold finger and achieve a small temperature gradient. For using heavy superconducting magnets, it is important to mount the sample in a highly controlled way because the goniometer cannot tilt such large objects by more than a few degrees.
The analyzer crystal is used in analogy to the monochromator crystal. Usually, a TAS is operated with fixed final energy E_f and the scattering angle $2\Theta_M$ of the monochromator crystal is varied in accordance to the desired energy transfer $\Delta E = E_i - E_f$.

Material	**structure**	**a(Å)**	**c(Å)**	(hkl)
Copper	fcc	3.61509		(111)
				(220)
Pyrolytic graphite	hexagonal	2.4612	6.7079	(002)
				(004)
Germanium	diamond	5.65776		(511)
				(711)
Silicon	diamond	5.43072		(111)

Table 2.2: Listed are some materials often used for monochromator and/or analyzer crystals. Their lattice structure and constants are given. Further the Miller indices of the most commonly used diffraction planes are indicated.

Spectrometer alignment

TASs are relatively simple instruments in concept. However, an accurate alignment is crucial. Misalignment can lead to reduced neutron intensities and, even worse, to spurious results. The alignment of a TAS is a non-trivial task because there are strong correlations between the setting of the monochromator, the sample and the analyzer. For example, the values of the sample rotation Φ' and the scattering angle $2\Theta'$, optimized for maximum intensity of a particular Bragg peak, will be different from their true values Φ and 2Θ, if the analyzer is slightly misaligned.
A systematic approach to the alignment to avoid correlated errors is described in ref. [7]. Checking the experimental alignment is one of the first tasks in each measurement.

Resolution function and focusing

Due to the necessity of using imperfect crystals for Bragg diffraction and of finite beam divergences in order to obtain higher neutron flux intensities, the actual result of a neutron scattering measurement is a convolution of an instrumental resolution function $R(\mathbf{Q}-\mathbf{Q_0}, \omega-\omega_0)$ and the scattering function $S(\mathbf{Q}, \omega)$. The resolution function is peaked at $(\mathbf{Q_0}, \omega_0)$ and decreases for deviations $(\Delta\mathbf{Q}, \Delta\omega)$. The shape of the measured spectra depends on the way in which the resolution function is scanned through the structures defined by the scattering function.
In general, the resolution function is a four dimensional ellipsoid - three dimensions in momentum space and one in energy. If we ignore the resolution perpendicular to the scattering plane, we have a three dimensional object, which has, in general, the shape of a flattened cigar. The peak width measured in a constant $\mathbf{Q}$ scan through a sharp dispersion surface will depend on the orientation of the resolution function relative to the dispersion surface. In a 'focused' condition, the two longer axes of the ellipsoid are parallel to the surface, and a narrow peak will be measured. In the opposite case, the

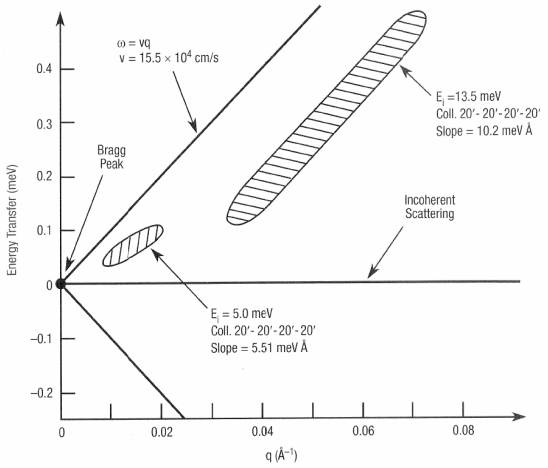

Figure 2.3: Triple-axis spectrometer resolution function calculated for incident neutron energies of 13.5 meV and 5.0 meV, compared with the dispersion curve (solid lines) for transverse acoustic phonons in niobium [10].

two long axes orthogonal to the surface, the peak may be so broad as to be undetectable. In the typical case of a non-monotonic dispersion surface, the choice is between more focused and less focused measurement conditions.
In fig. 2.3 two-dimensional projections of the resolution ellipsoid for two different incident neutron energies are shown together with the dispersion curve of a transverse acoustic phonon in Niobium [7, 10]. Scanning the instrumental resolution through the dispersion at positive energy transfer will refer to a nearly optimal focusing, as the long axis of the ellipsoid and the dispersion surface are approximately parallel to each other. At negative energy transfer the measurement is defocused and the phonon is probably indetectable. For most TASs the instrumental resolution can be accounted for by a deconvolution of the measured neutron intensities with a gaussian function, the latter representing the instrumental resolution. The deconvoluted linewidths contain the information about intrinsic properties, e.g. the lifetime of a phonon and thereby the strength of the electon-phonon coupling for a particular phonon.

Special problems

Because of the non-ideal behaviour of the elements of a TAS and the sample environment, scattering artefacts are often observed in both, elastic and inelastic neutron scattering. In many cases such artifacts appear as sharp peaks, which mimic intrinsic scattering features. The proper identification of such spurious peaks (so-called 'spurions') is crucial to extract the physically relevant information of the scattering results.

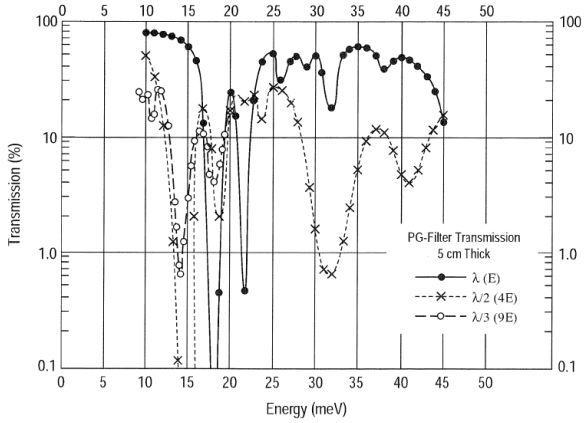

Figure 2.4: Transmission of a 5-cm-thick PG filter as function of energy for desired energy E (λ), $4E$ ($\frac{\lambda}{2}$) and $9E$ ($\frac{\lambda}{3}$) [7].

There are several well understood mechanisms, which will produce scattering artifacts. Some of them are related to higher-order neutrons (harmonics) in the incident neutron beam. An ideal monochromator would select just one unique incident neutron wave vector k_i. In reality, however, Bragg diffraction of a single-crystal is used. From eq. (2.2) it follows that for a specific angular setting Θ_B of the monochromator crystal also neutrons are Bragg diffracted by the monochromator crystal with wavelengths

$$\lambda = \frac{\lambda_{max}}{n} \qquad n\text{: natural number}$$
$$\lambda_{max} = 2d_{hkl} sin\,\Theta_B. \tag{2.3}$$

Although the flux of such higher-order neutrons with $n \geq 2$ is typically much weaker than that of the first-order wave vector, they can give rise to spurious peaks, comparable to small intrinsic features of the scattering function. There are several filter concepts to suppress these unwanted peaks.

In the thermal energy regime pyrolytic graphite (PG) is by far the most useful filter of higher-order neutrons. The transmission of a 5-cm-thick PG filter, the c axis being parallel to the wavevector of the neutrons, for a desired energy E (λ), $4E$ ($\frac{\lambda}{2}$) and $9E$ ($\frac{\lambda}{3}$) is shown in fig. 2.4. Normally k_f is fixed and the PG filter is placed between the sample and the analyzer. The most advantageous final energies are 14.7 meV and 30.5 meV, where the transmission is strongly in favor of the first-order neutrons.

Another possibility to suppress second-order contamination is the usage of an odd reflection of a non-centrosymmetric monochromator crystal, such as Ge(711). Here, the second-order Bragg scattering is forbidden by the symmetry of the crystal. The flux obtained in third order, which means $E_{n=3} = 9E_{n=1}$, is normally negligible.

A second mechanism to produce spurious results is accidental Bragg scattering by the

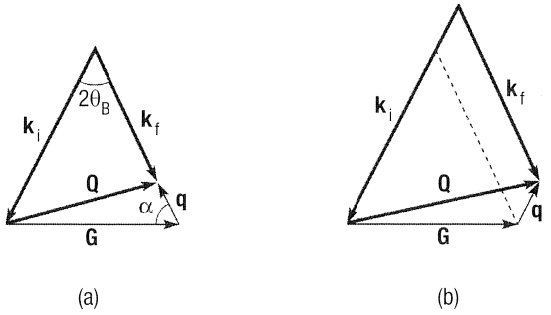

Figure 2.5: Scattering diagrams for energy loss, illustrating the conditions for accidental Bragg scattering for weak scattering from (a) the analyzer and (b) the monochromator.

sample. For a TAS, we have two crystals, the monochromator and the analyzer, set to Bragg reflect. The third crystal, the sample, might now accidentally be in a Bragg scattering position for the incident or the final wave vector. The scattering diagrams for both cases are shown in fig. 2.5. In fig. 2.5 (a) the sample scatters $\mathbf{k}_i$ elastically, corresponding to the reciprocal lattice vector $\mathbf{G}$, which lies in the same direction as the nominal $\mathbf{k}_f$. Thus, if there is incoherent or diffuse scattering from the analyzer, some neutrons will be detected. The opposite situation with Bragg scattering for $\mathbf{k}_f$ and incoherent or diffuse scattering from the monochromator is shown in fig. 2.5 (b).
Spurious peaks can also be caused by resolution function effects. When doing scans near a reciprocal lattice point $\mathbf{G}$, it can easily occur, that the tail of the resolution ellipsoid sweeps through $\mathbf{G}$ and picks up some intensity. Also, nominally strict selection rules for certain excitations may be weakened by resolution effects. Therefore excitations with the 'wrong' symmetry can happen to be detected.
Finally, there are also artifacts originating in the sample environment, such as Bragg scattering by aluminum, the material of most sample holders, sample cans and cryostat radiation shields. The sample can is normally filled with He as exchange gas. However, a certain amount of air can not be avoided. Hence, temperature dependent effects of the background can be caused by the condensation of these gases.

2.3 Elastic neutron scattering

A direct image of atomic structures can presently be achieved by high-resolution electron-microscopy (EM) atomic-force microscopy (AFM) and scanning-tunneling microscopy (STM). However, these techniques have their applications mostly in the investigation of point defects, atomic displacements and surface properties. Diffraction experiments are more appropriate to study the structural parameters and to determine the overall

structure of an unknown compound. The reason is that diffraction measurements make optimal use of the periodicity of the solid state.
X-rays, electrons, atoms or neutrons can be used as probes in diffraction measurements. There are fundamental differences between these types of radiation. The neutron is scattered by the atomic nucleus (and also by magnetic moments, if present), while X-rays and electrons are scattered by the electronic shell. Atoms are only appropriate for surface investigations as they do not penetrate into the solid state.
As already mentioned in chapter 2.1, neutrons are unique in the way, that they can penetrate deep into the solid state and carry a non-zero magnetic moment. Therefore elastic neutron scattering, or neutron diffraction, is mostly used to determine crystallographic and magnetic structures. As samples may be available in single-crystal or only in polycrystalline form, there are two principally different experimental setups in neutron diffraction: Powder diffraction and single-crystal diffraction.

2.3.1 Powder diffractometer

The advantage of a powder diffractometer over a single-crystal diffractometer is obvious in so far as only polycrystalline samples are needed, but also due to the fact that the sample needs not to be aligned. The principle of the measurement is equivalent to a Debye-Scherrer experiment with X-rays [11], but in addition also magnetic superlattice reflections can be detected (see figs. 4.17 and 4.18).
The setup of a standard neutron powder diffractometer is shown in fig. 2.6 for the two-axis instrument E9 FIREPOD (*FIne REsolution POwder Diffractometer*) at the Hahn-Meitner Institut (HMI), Berlin. The main difference to a TAS is the absence of an analyzer. Therefore, a two-axis instrument measures all scattered neutrons, which are scattered elasticaly and inelastically, coherently and incoherently. In most cases, the coherent elastic signal is much stronger than the background of diffuse and inelastic scattering and thus the lack of an analyzer is no major problem for many experiments. A bank of detectors is used in order to speed up the measurement, i.e. 64 ^{3}He single detector tubes, each covering stepwise an angular distance of nominally 2.5°, are operated at the E9 at HMI (see photograph of E9 in fig. 2.7).

2.3.2 Single-crystal diffractometer

Although Brockhouse originally invented the TAS for the study of inelastic processes, it has also proven to be an exceptionally useful instrument for measuring elastic intensities in cases where the intensity is inherently low, such as from small single crystals. The ability to use an anlyzer results in a better signal-to-noise ratio compared to the two-axis instruments with no analyzer. The analyzer selects only the elastic scattering and hence suppresses contributions from inelastic processes at finite energy transfers. Also the loss in intensity related to the additional reflection by the analyzer is not too big as analyzer crystals can be made with high reflectivities ($> 50\%$) and moreover, the analyzer can

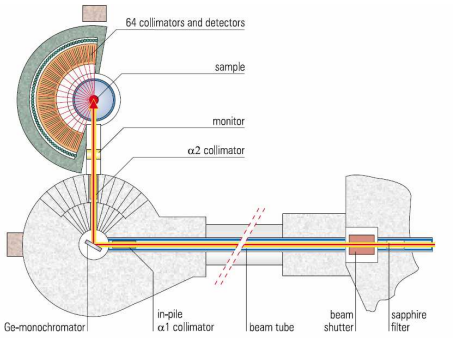

Figure 2.6: Schematic view of the E9 *Firepod* at HMI, Berlin, Germany.

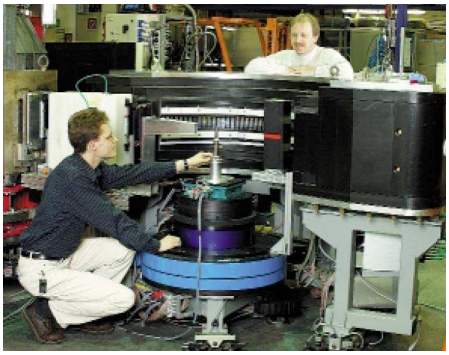

Figure 2.7: Photograph of the E9 *Firepod* at HMI, Berlin, Germany.

Instrument	**Location**	**Material**
1T, thermal TAS	LLB, CE Saclay	$La_{0.7}Sr_{0.3}MnO_3$, $La_{1.24}Sr_{1.76}Mn_2O_7$, YNi_2B_2C
PUMA, thermal TAS	FRM 2, Garching	YNi_2B_2C
IN 8, thermal TAS	ILL, Grenoble	$La_{1.24}Sr_{1.76}Mn_2O_7$
E9, powder diffraction	HMI, Berlin	$La_{0.7}Sr_{0.3}MnO_3$

Table 2.3: List of the instruments used during this work.

focus the scattered neutron beam onto the detector to increase the intensity.
Another advantage of a TAS is the ability and ease of changing the energy of both the incoming and the outgoing neutron beam. This capability has been proven very useful for the detection and elimination of multiple scattering. With a TAS the energy of incoming and outgoing neutrons can be varied, under the constraint $E_i = E_f$, while monitoring the intensity of a Bragg peak. On the one hand, if this intensity remains constant, the scattering can be considered as real, i.e. first-order, scattering. On the other hand, if it is rapidly changing with energy, it is most likely multiple scattering.

3 Lattice dynamical properties of YNi_2B_2C

Superconductivity in quaternary rare-earth transition metal borocarbides (RTBC) was discovered by Mazumdar et al. for a Y-Ni-B based system with the nominal composition YNi_4B in 1994 [12]. Although the superconducting transition was clearly observed in resistivity and susceptibility measurements, the estimated superconducting fraction of the sample was less than 2 %. Shortly after, Cava et al. and Siegrist et al. reported superconducting transition temperatures of $T_c = 16.6\,\mathrm{K}$ and $T_c = 23\,\mathrm{K}$ for $LuNi_2B_2C$ and a yttrium-palladium based borocarbide, respectively [13–15]. Whereas for the composition Y-Ni-B-C the phase being responsible for the superconductivity could be identified relatively easy as YNi_2B_2C, the situation for the palladium-based system is still complicated. Only in 2000, Dezaneti et al. showed that it is the phase with the composition YPd_2B_2C that has the observed superconducting transition temperature of $T_c = 23\,\mathrm{K}$ [16].
Despite their layered structure (see fig. 3.1) and relatively high transition temperatures, the RTBC show 3D-metallic behaviour in the normal state and are considered to be conventional s-wave superconductors.
Apart from their high superconducting transition temperatures, the RTBC have attracted much scientific interest because of the coexistence of superconductivity and long-range magnetic order in compounds with R = Dy, Ho, Er, Tm [14, 17–22]. *RTBC* are special in that the ordering temperatures T_c and T_N of superconductivity and antiferromagnetism are comparable, where $T_N < T_c$ for R = Tm, Er, Ho and $T_N > T_c$ for R = Dy.
In conventional superconductors, superconductivity is mediated by phonons. This motivated studies of the lattice dynamical properties of the RTBC family. The growth of large high-quality single-crystals of the $RENi_2B_2C$ family (RE = Y, Lu, Ho, Er, Dy,...) shortly after their discovery facilitated intensive elastic and inelastic neutron scattering studies [23–30] including measurements of the phonon density of states (PDOS) by our own group [31]. However, the phonon dispersion relations were not studied in detail.
Extensive calculations for the lattice dynamical properties of non-magnetic superconducting YNi_2B_2C were made in the theory group of our institute [32]. A description of the density-functional theory (DFT) used for these calculations is given in chapter 3.2.1. The experimental verification of the theoretical predictions is a central part of this work. In the first part of this chapter, a brief summary of phonon measurements by inelastic neutron scattering, is given. Section 3.2 contains a description of the DFT calculations and their main results, followed by the analysis of the neutron scattering results for the normal state of YNi_2B_2C . In the last section, the influence of superconductivity on the phonon spectral weight function is discussed.

The experiments were carried out on the TAS *1T* at LLB, Saclay, and on the TAS

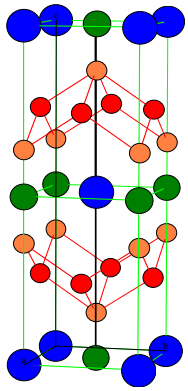

Figure 3.1: Unit cell of the tetragonal body-centered structure of YNi_2B_2C (I4/mmm). Yttrium (blue) - Carbon (green) planes are separated by Nickel (red) - Bor (orange) sheets.

DAS PUMA at the research reactor in Munich, FRM-II. The sample was a high-quality single-crystal with a mass of $m = 2.26\,\mathrm{g}$ grown in Dresden. At the LLB, the sample was mounted in a standard Helium cryostat with a lowest accessible temperature of 2 K for the measurement of the low-lying phonons in the (100) direction. Measurements for the phonons in the (xx1) and (001) directions were done in a closed cycle refridgerator ($T_{min} = 10\,\mathrm{K}$). At the FRM-II, the single-crystal was mounted in a closed-cycle refrigerator with a minimal temperature of 3 K. The sample had a $T_c = 15.2\,\mathrm{K}$, slightly lower than the maximum value $T_c = 15.6\,\mathrm{K}$ reported in the literature [14].

3.1 Phonon scattering

Before the invention of the TAS by B. Brockhouse [8], the dispersions of lattice vibrations and spin waves were largely unknown. Some rough estimates of the PDOS could be obtained, for example, from a careful analysis of the specific heat, but the behaviour of a single phonon was not measureable. Presently, neutron TAS are the most important instruments for measuring the phonon and magnon dispersion at any point in reciprocal space $\mathbf{Q}$ and energy E.[1] In the last few years, TASs have been built for inelastic X-ray

[1] In many publications phonon dispersions are shown in frequency ν versus momentum transfer $\mathbf{q}$. To convert frequency to energy units, the conversion factor is

$$1\,\mathrm{THz} = 4.136\,\mathrm{meV}. \tag{3.1}$$

scattering as well. The resolution in X-ray experiments, especially at high energies, is sometimes better than in neutron scattering. In particular, these instruments achieve a very high resolution in momentum space. In this project, only inelastic neutron scattering was used. The measurements were aiming at:

- The phonon dispersion for various directions in $\mathbf{q}$ space. In particular, it was important to search for so-called phonon anomalies predicted by DFT. The term phonon anomaly designates a pronounced reduction of the phonon frequency in a rather narrow range of momentum transfers which cannot be explained by short-range interatomic forces. They are indicative of a strong electron-phonon coupling.
- The $\mathbf{q}$-dependent phonon linewidth, which reflects the strength of the electron-phonon coupling.
- The absolute phonon intensities in different Brillouin zones, which allows one to deduce the phonon polarization patterns.

The order of the listed properties also indicates the difficulty of the experimental determination. Whereas for the dispersion 'only' the peak position is needed, the accuracy of the experimental phonon linewidth values depends strongly on an accurate determination of the experimental background. This is even more true for the determination of the integrated phonon intensities.

3.1.1 Phonon dispersion

In the simplest case, the frequency of a phonon is determined from the centre of a neutron intensity distribution as obtained in a const-$\mathbf{Q}$ scan. A dispersion curve is obtained from measurements at several points in $\mathbf{Q}$ space along a particular direction. However, the experimental determination of the phonon dispersion is complicated by various problems. To begin with, the intensity can be too low due to an insufficient size of the sample or a small structure factor for a specific phonon. Further, the resolution in energy may be insufficient to separate two different phonon branches which are close in energy. The near-degeneracy of two phonon branches is a frequent phenomenon in complicated structures like YNi_2B_2C and the manganites with many and strongly dispersive phonon branches.
Phonon branches with strong dispersion might cross other phonon branches. If the two phonons are of different symmetry, then they do not interact (see many examples in fig. 3.3). But if they are of the same symmetry, a crossing of branches is forbidden by group theory. This case is called an *anti-crossing*. An example are the two lowest lying branches in the (100) direction plotted in black in fig. 3.3, which are both of the same symmetry, called Δ_4. At $\mathbf{q} = (0.4, 0, 0)$, the upward dispersion of the acoustic branch and the downward dispersion of the optic one lead to an *anti-crossing*. Because of their symmetry, they interact with each other with a coupling parameter $\Delta(\mathbf{q})$. In the region in $\mathbf{q}$ space with finite coupling, the character of the acoustic phonon gradually passes over to the upper branch with increasing $\mathbf{q}$, meanwhile the character of the optic branch

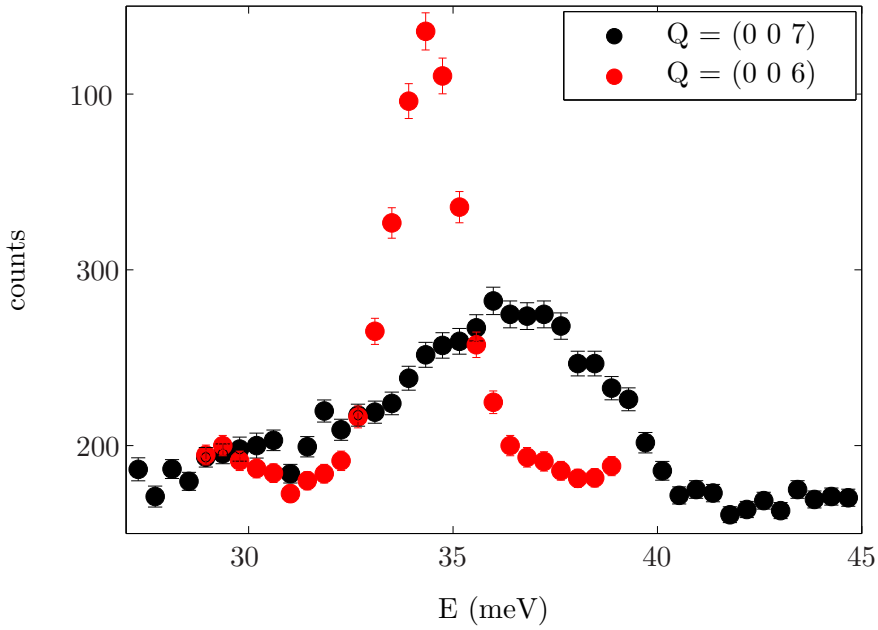

Figure 3.2: Constant momentum scans at $T = 3\,\mathrm{K}$ in YNi_2B_2C . The phonon measured at $\mathbf{Q} = (6,\ 0,\ 0)$ is found to be resolution limited with a total width of 1.9 meV, whereas the other one is extremely broadened with an intrinsic linewidth of approximately 5 meV.

does the opposite. In the 'mixing' zone, the two phonons show characteristics of both original elongation patterns. If one follows a specific branch in a Brillouin zone, where the second branch has a zero structure factor, the anticrossing can easily be missed, because the only feature indicative of the *anti-crossing* seen in such an experiment is a certain broadening of the phonon peak in the 'mixing' zone.

3.1.2 Phonon linewidth

The linewidth of a phonon is proportional to the inverse of its lifetime. In an ideal crystal, the lifetime of the phonon would be infinite and the linewidth be zero. In reality, the linewidth is finite due to:

- anharmonicity effects (phonon-phonon interaction)
- electron-phonon interaction
- crystal imperfections

In addition, the finite instrumental resolution significantly contributes to the observed linewidth.

The separation of the different contributions to the observed phonon linewidth is rather difficult. Especially at low temperatures, the dominant contribution is often given by the instrumental resolution. As already discussed in section 2.2.1, the actual result of a neutron scattering measurement is a convolution of the instrumental resolution function $R(\mathbf{Q}-\mathbf{Q_0}, \omega-\omega_0)$ and the scattering function $S(\mathbf{Q},\omega)$. The resolution function can often be approximated with a gaussian lineshape. The actual value of the resolution, e.g. the linewidth of the resolution function, can either be calculated, or experimentally determined. The former is done by 'summing' over the effects of the imperfect nature of the monochromator and analyzer crystals as well as the neutron beam divergencies [33]. The observed linewidth does not only depend on the energy resolution, but on the monentum resolution as well. As a consequence, the slope of the phonon dispersion in a certain neighbourhood in $\mathbf{q}$ matters as well (see also focusing effects in section 2.2.1). The experimental determination of the resolution width is shown in fig. 3.2 for the investigation of the phonon anomaly at $\mathbf{q} = (0,\ 0,\ 1)$, $E = 36\,\mathrm{meV}$ (see fig. 3.5 and 3.9 (a)). The zone center phonon (red dots) has a very small intrinsic linewidth, whereas the zone boundary phonon at $\mathbf{Q} = (0,\ 0,\ 7)$ (black dots) is extremely broadened. In this approach, one has to be aware, that the resolution is energy and $\mathbf{q}$ dependent. Therefore the frequency of the 'reference' phonon should be in the vicinity of the frequency of the investigated phonon, and also the slope of the phonon dispersion at the measured $\mathbf{q}$ points should be similar.
Unfortunately, a direct deconvolution of the experimental result to obtain the intrinsic phonon linewidth is not possible. Therefore, one convolutes the resolution function with an assumed lineshape of the intrinsic line, normally gaussian or lorentzian, and fits the parameters of the intrinsic line to the measured neutron data. If the contribution to the observed linewidth from the instrumental resolution is much bigger than the intrinsic phonon width, then the latter is hard to measure. To give a numerical value, strong-coupling effects in the intrinsic phonon linewidth, which are less than 10% of the energy resolution, are practically not measureable.
It can be said that anharmonic effects lead generally to an increase of the phonon linewidth and a softening of the phonon frequency with increasing temperature. On the other hand, strong electron-phonon coupling often leads to the opposite temperature dependence, in particular if it is associated with a nesting feature in the electronic system. The nesting is more pronounced at low temperatures, whereas it is reduced at elevated temperatures because of the thermal smearing of the Fermi surface.

3.1.3 Phonon intensity

The energy-integrated intensity for phonon creation measured in a constant $\mathbf{Q}$ scan is given by [7]

$$I_E \propto F(k_f)\,[n(\omega)+1]\,\frac{\left|\mathbf{Q}\cdot\overrightarrow{\xi_j}\right|^2}{\hbar\omega}e^{-2W(\mathbf{Q})}, \tag{3.2}$$

where $\overrightarrow{\xi_j}$ is the eigenvector of the jth phonon, $exp(-2W(\mathbf{Q}))$ the Debye-Waller factor, and $n(\omega)$ the Bose factor. $F(k_f)$ is a constant for fixed final energies, as used in all

inelastic measurements in this work. From eq. 3.2 one can see that the integrated intensity for phonon creation at a given energy transfer is proportional to the square of the scalar product of the phonon eigenvector ξ and the total momentum transfer $\mathbf{Q}$. Therefore phonons are mostly measured with the maximal $\mathbf{Q}$ accessible in a particular experiment. Further, using a large $\mathbf{Q}$ minimizes possible contributions from spin waves whose intensities are maximum at low $\mathbf{Q}$ because of the decrease of the magnetic form factor with increasing $\mathbf{Q}$.
The Bose factor $n(\omega)$ refers to the Bose-Einstein statistics, which apply to phonons. The thermal occupation of phonons, and magnons as well, at energies E_j increases with temperature and therefore the integrated intensity of a phonon at energy $E_j = \hbar\omega_j$ increases with temperature by a factor of

$$[n(\omega_j) + 1] = \frac{1}{e^{\frac{\hbar\omega_j}{k_B T}} - 1} + 1. \tag{3.3}$$

The Debye-Waller factor, in general, describes the redistribution of the total intensity into elastic, one-phonon and multi-phonon scattering due to the atomic displacements from the equilibrium positions and is given by

$$e^{-2W(\mathbf{Q})}, \qquad 2W(Q) = \left\langle \{Q \cdot \hat{u}\}^2 \right\rangle, \tag{3.4}$$

where Q is the absolute value of the total momentum transfer $\mathbf{Q}$ and $\langle \hat{u}^2 \rangle$ the atomic mean square displacement. By the increase of the mean square displacements of the atoms with temperature, the phonon intensity is decreased, because the degree of correlation between the atomic movements decreases.

3.2 Phonon dispersion and electron-phonon coupling in the normal state

Although T_c reaches rather high values, it is generally assumed that the superconductivity in the RTBC is phonon-mediated. This view is supported by the observation of strong phonon anomalies in RTBC compounds (R = Y [24], Lu [25], Tb and Ho [22]). More precisely, a pronounced anomaly was observed in a low-energy optical phonon branch in the (100) direction at wave vectors about $\mathbf{q}$ = (0.5, 0, 0) (we note that the phonon branch in question makes an anti-crossing with the transverse acoustic branch at about $\mathbf{q}$ = (0.4, 0, 0) and therefore becomes formally the acoustic branch for larger wave vectors). The observation of a strong softening and broadening of these anomalous phonons, in connection with a pronounced Fermi-surface nesting at the same wave vector, gives evidence for a strong coupling of these phonons to the electronic system.
Neutron scattering results for the structural parameters indicate a strong influence of the c/a ratio on T_c [34], which is connected to the electronic density of states at the Fermi energy [35]. In fact, the variation of c/a results in a deviation of the NiB_4 tetrahedra

from its ideal tetrahedral symmetry. Thus, a particularly strong electron-phonon coupling is expected for the A_{1g} phonon at $E = 103\,\mathrm{meV}$ [36–38], which strongly modulates the binding angle of the NiB_4 tetrahedra [32].

3.2.1 First principles calculations

In the following, a short description of the density-functional theory (DFT) used for the calculation of the RTBC properties will be given. For a more detailed description and review see refs. [39–41] and references therein.
The *Hohenberg and Kohn theorem* states that all the physical ground-state properties of a system of interacting electrons are uniquely determined by its charge density distribution [42]. This theorem provides the foundation of what is currently known as DFT. It can be shown that a universal functional, $F[n(\mathbf{r})]$, of the electron charge density exists such that the functional

$$E[n] = F[n] + \int n(\mathbf{r})V(\mathbf{r})d\mathbf{r} \tag{3.5}$$

is minimized by the electron charge density of the ground state corresponding to the external potential V(r), under the constraint that the integral of n($\mathbf{r}$) equals the total number of electrons. Furthermore, the value of the minimum coincides with the ground-state energy. For the search of the ground-state properties of a system of interacting electrons, it replaces the traditional description based on wave functions (which depend on 3N independent variables, N being the number of electrons) with a much more tractable description in terms of the charge density, which depends on only three variables. One problem hampering a straightforward application of this result, is that the form of the F functional is unknown. This problem is handled by the *Kohn and Sham equations*, mapping the system onto an auxiliary system of non-interacting electrons [43]. In their paper, Kohn and Sham also proposed the assumption that each small volume of the system contributes the same exchange-correlation energy as an equal volume of a homogeneous electron gas at the same density. This is known as the *local density approximation (LDA)*, used by Reichardt and coworkers for their calculations of the properties of YNi_2B_2C [32].
Within the adiabatic approximation[1], lattice dynamical properties are accessible by considering a linear response of the electron system to a perturbation induced by atomic displacements. One of the greatest advantages of this expansion of DFT to become the density functional perturbation theory (DFPT) [44] is that within DFPT the responses to perturbations of different wavelengths are decoupled. This feature allows one to calculate phonon frequencies at arbitrary wave vectors $\mathbf{q}$ avoiding the use of supercells.
DFPT is directly applicable to metals, provided the (electronic) temperature is zero, so that a clear-cut separation between occupied and empty states is possible. In this

[1] Also known as *Born-Oppenheim approximation*: The movements of the atomic lattice is slow compared to the dynamics of the electronic system. Therefore, the electron-problem is treated for static positions of the nuclei.

case, however, the number of **k** points needed to adequately sample the Fermi surface would be very large. Practical implementations of DFPT to metallic systems have been discussed by Quong and Klein [45] and by de Gironcoli [46], which are based on a smearing technique for dealing with Fermi-surface effects. In the smearing approach, each Kohn-Sham energy level is broadened by a smearing function,

$$\delta_{sigma}(\epsilon) = \frac{1}{\sigma}\tilde{\delta}(\epsilon/\sigma) \tag{3.6}$$

where $\tilde{\delta}(x)$ is any function that integrates to 1, so that $\tilde{\delta}(\epsilon)$ tends to the Dirac δ function in the limit of vanishing smearing width σ. The local density of states resulting from the broadened energy levels will be the original one, convoluted with the smearing function.

The implemantation used by Reichardt and Heid is based on a mixed-basis pseudopotential method. A mixed basis set consists of localized atomic−like states for the core electrons plus plane waves for the valence electrons. A pseudopotential is a fictitious electron-ion interaction potential, acting on valence electrons only, that mimics the interaction with the inner electrons which are supposed to be frozen in the core as well as the effective repulsion exerted by the latter on the former due to their mutual orthogonality.
Using DFPT one can compute the interatomic force constants from first principles and from these frequencies and displacement patterns are obtained, without need of experimental inputs.
In most applications, phonon dispersions are computed at the theoretical equilibrium geometry (lattice parameters and internal coordinates). However, the LDA also has some well-known shortcomings. A large overestimate (up to 20%) of the crystal cohesive and molecular binding energies is possibly the worst failure of this approximation, together with its inability to properly describe strongly correlated systems, such as transition-metal oxides. A result of the former is that the calculated volume of the unit cell is normally about 2% smaller than found in experiment [47].
The main interest of phonon calculations in metals stems from their transport properties, especially superconductivity. DFPT provides information not only on phonon dispersions but also on the electron-phonon coupling strength, i.e. the phonon linewidths, in the whole Brillouin zone, thus giving an accurate estimate of the coupling strength. Furthermore, the availability of accurate phonon dispersions and phonon linewidths over the entire Brillouin zone allows the calculation of the electron-phonon (Eliashberg) spectral function $a^2F(\omega)$ and of the mass enhancement parameter λ that enters the Allen-Dynes equation for the superconducting transition temperature T_c (see next section).

3.2.2 Lattice properties of YNi_2B_2C from first-principles

The superconductor YNi_2B_2C is a suitable candidate for the calculation of its lattice properties including the electron-phonon coupling strength based on DFPT because of three reasons:

- YNi_2B_2C has a relatively high superconducting transition temperature $T_c = 15.5\,\mathrm{K}$ indicating a strong electron-phonon coupling.
- YNi_2B_2C is non-magnetic (DFT is presently not able to give an accurate description of magnetic compounds).
- The $4f$ orbitals in YNi_2B_2C are not occupied. $4f$ electrons cannot be properly described by DFT, because they are localized but no real core electrons. So, they are neither atomic−like nor free electrons.

The results of the calculation of Reichardt et al. [32] for the lattice dynamical properties for YNi_2B_2C are shown in fig. 3.3. Lines represent the phonon dispersion, bars the electronic contribution to the phonon linewidth, $\gamma_{\mathbf{q}\lambda}$. Colors indicate branches of the same symmetry class. Branches with longitudinal character are shown in red, c-axis polarized phonons are shown in black except for the (001) direction, where c-axis polarized branches are of longitudinal character (shown in red). The linewidth $\gamma_{\mathbf{q}\lambda}$ is displayed in meV in the upper panel and in percentage of the phonon frequency $\gamma_{\mathbf{q}\lambda}/\omega_{\mathbf{q}\lambda}$ in the lower panel. The second representation is more suitable to show the importance of specific phonons for superconductivity, because the displayed ratio $\gamma_{\mathbf{q}\lambda}/\omega_{\mathbf{q}\lambda}$ directly enters into the Eliashberg function,

$$\alpha^2 F(\omega) = \frac{1}{2\pi N(0)} \sum \frac{\gamma_{\mathbf{q}\lambda}}{\omega_{\mathbf{q}\lambda}} \delta(\omega - \omega_{\mathbf{q}\lambda}). \tag{3.7}$$

$N(0)$ is the electronic density of states (per atom and spin) at the Fermi energy.
The only additional material specific quantity entering the gap equations is the effective electron-electron interaction constant μ^*, which is treated as a free parameter. A reasonable approximation to T_c can be obtained from the Allen-Dynes formula [49],

$$T_c = \frac{\omega_{eff}}{1.2}\, exp\left(\frac{-1.04(1+\lambda)}{\lambda - \mu^*(1+0.62\lambda)}\right), \tag{3.8}$$

where the electron-phonon coupling enters only via two moments of $\alpha^2 F(\omega)$, the average coupling constant (also average mass enhancement parameter)

$$\lambda = 2\int_0^\infty d\omega \frac{\alpha^2 F(\omega)}{\omega} \tag{3.9}$$

and an average effective frequency defined as

$$\omega_{eff} = exp\left(\frac{2}{\lambda}\int_0^\infty d\omega \frac{\alpha^2 F(\omega)}{\omega} ln(\omega)\right). \tag{3.10}$$

From these equations it is evident that both a large λ and a large ω_{eff} are favorable for a high superconducting transition temperature. For YNi_2B_2C, Reichardt and Heid calculated $T_c = 12.6\,\mathrm{K}$ [32], which is not too far below the experimental value of $15.5\,\mathrm{K}$. The calculated average coupling constant $\lambda = 0.89$ identifies YNi_2B_2C as a medium to

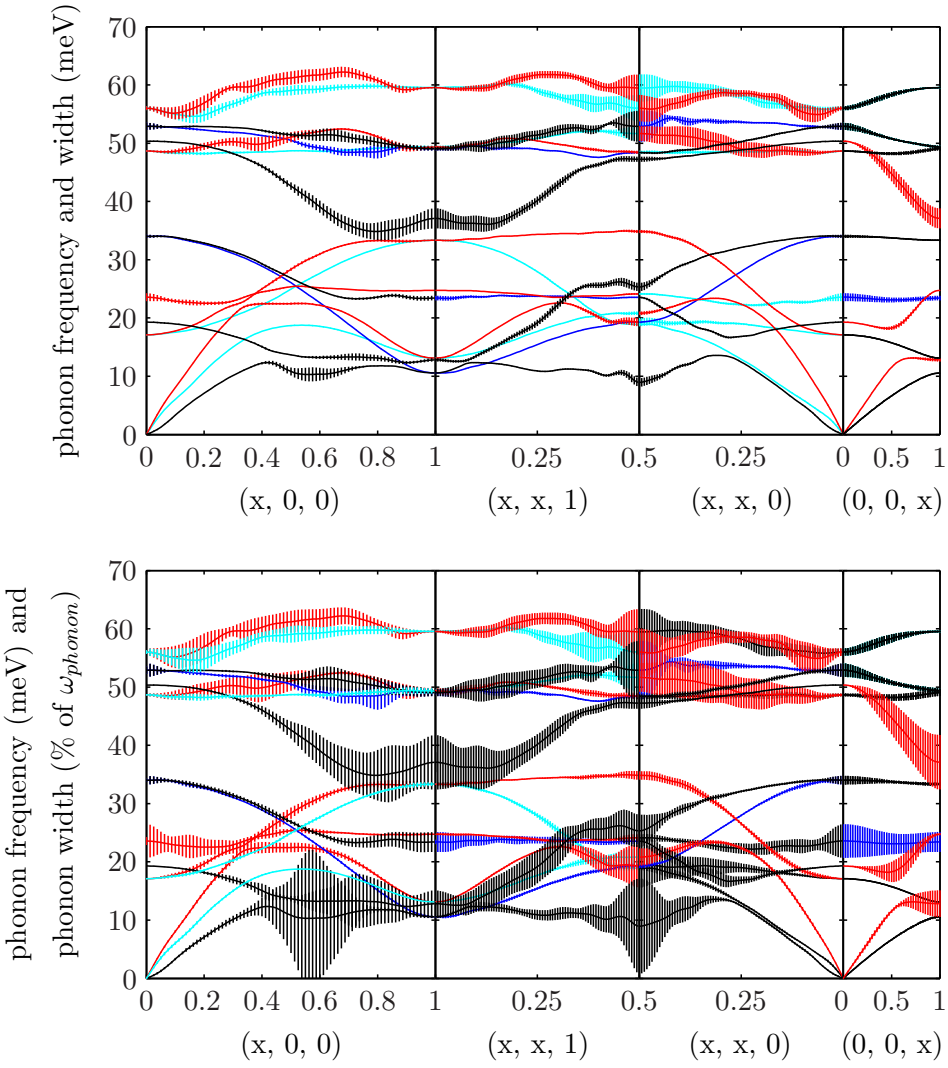

Figure 3.3: Calculated phonon dispersions and phonon linewidths for YNi_2B_2C using DFT in the LDA [48]. Lines represents the phonon frequencies, vertical bars show the value of the calculated intrinsic phonon linewidth in meV (upper panel) and in % of the phonon frequency ω_{phonon} (lower panel). Different colors denote phonons of different symmetry classes. The horizontal axes denote different crystallographic directions in reciprocal lattice units (r.l.u.).

strong coupling superconductor.
One has to mention, that Reichardt and Heid used the experimental structure for their calculations, which is about 2% larger than the optimized structure, which is found by minimizing the functional $E[n]$ in eq. 3.5. Reichardt et al. preferred to use to the experimental structure for two reasons:

- Phonon frequencies obtained with the experimental structure were in better agreement with the phonon data available from Raman scattering [36–38] and the generalized PDOS [31].
- The calculated $T_{c,calc} = 12.6\,\mathrm{K}$ using the experimental structure is much closer to the experimental value of $T_c = 15.5\,\mathrm{K}$ than the prediction using the optimized structure ($T_{c,opt} = 5.8\,\mathrm{K}$) [48].

Fig. 3.3 shows strong phonon anomalies accompanied by large electron-phonon coupling. In particular, the c-axis polarized transverse acoustic (TA) branches in the (100) and the (110) directions and the transverse optic (TO) branch dispersing between $51\,\mathrm{meV} \geq \mathrm{E} \geq 36\,\mathrm{meV}$ in the (100) direction (all shown in black) have huge anomalies in their dispersions coupled with extreme electron-phonon coupling. These phonons and several other strong-coupling phonons produce two sharp peaks in the energy integrated λ at $\mathbf{q} = (0.6, 0, 0)$ and at $\mathbf{q} = (0.5, 0.5, 0)$, the so-called M-point, both values being larger than 2.5, compared to an average value of $\lambda_{av} = 0.89$. One major goal of the present work was the investigation of these phonon anomalies in means of the frequency, the intrinsic linewidth (i.e. the phonon lifetime) and the atomic displacement patterns.
A non-trivial result of the DFT calculations is the appearance of strong elongations of the light B and C atoms in the anomalous acoustic modes in the (100) and the (110) directions. DFT calculations have shown that the electronic states near the Fermi level are mainly from the B and C atoms. Therefore, the DFT predicts that two thirds of the total coupling strength λ_{tot} are due to the light atoms B and C. At the same time, about 70% of λ results from the nine lowest branches. These two predictions seem to be somewhat contradictory because the light atoms are expected to have large amplitudes only in high energy branches. However, they are not really contradictory because the electron-phonon coupling not only renormalizes the phonon frequencies, but also influences the phonon eigenvectors, giving rise to large oscillations of B and C atoms in low energy branches, in particular around $\mathbf{q} = (0.55, 0, 0)$ and $(0.5, 0.5, 0)$.
In fig. 3.4 the absolute values of the atomic displacements $|\overrightarrow{u}|_{phonon}$ for the four atomic species, Y, Ni, B and C, are shown. The displacement values are plotted along the (100) and the (110) direction for (1) the strong coupling TA branches and (2) the first TO branch of the same symmetry. (a) and (c) are calculated using DFT, whereas (b) and (d) are results of a Born-von-Karmann (BvK) model (see sect. 4.2). Points are the calculated values, lines are guides to the eye.
Obviously, the BvK model does not predict the large B and C amplitudes at $\mathbf{q} = (0.6, 0, 0)$ and $(0.5, 0.5, 0)$, which are responsible for the strong electron-phonon coupling in the DFT. Also a peak in the light atoms' amplitudes in the optic branch in the (100) direction around $\mathbf{q} = (0.75, 0, 0)$ is not reproduced by the BvK model. The resulting structure factors will be compared to the experimental findings.

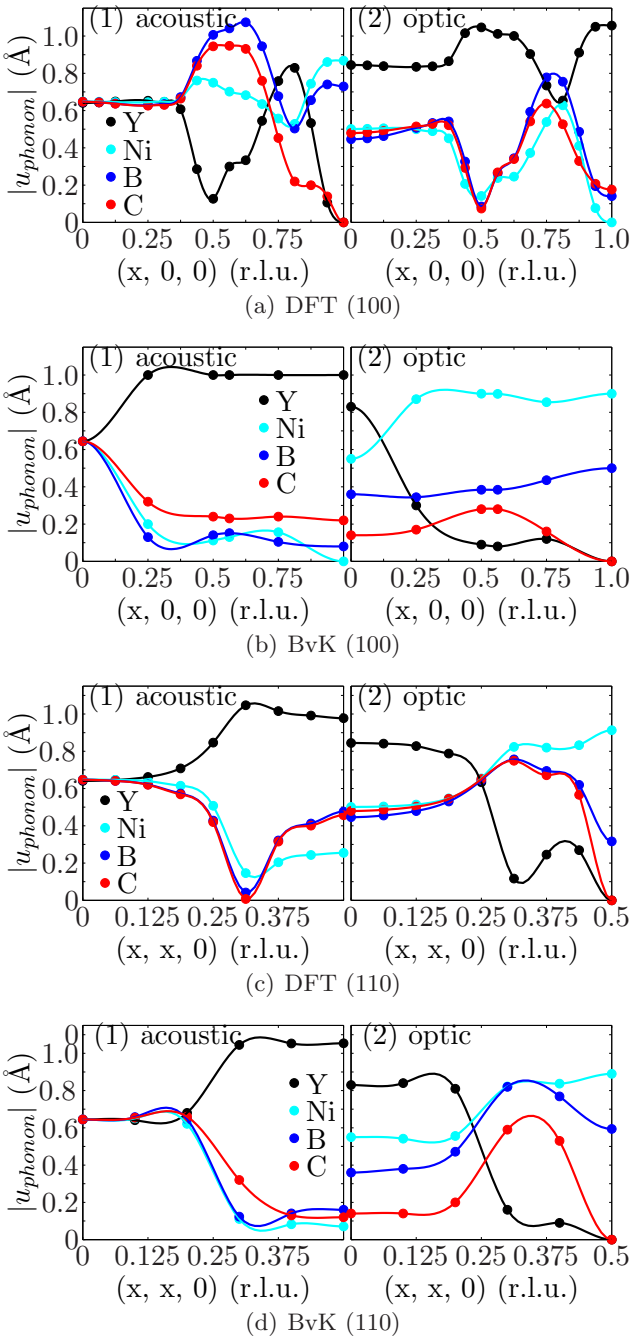

(a) DFT (100)

(b) BvK (100)

(c) DFT (110)

(d) BvK (110)

Figure 3.4: Calculated atomic displacements for the (1) acoustic and the (2) first transverse optic phonon using DFT (a,c) and a Born-von-Karman (BvK) model (b,d) along the (100) (a,b) and (110) directions (c,d) in YNi_2B_2C. Note that the phonon anomalies occur at $\mathbf{q}$ = (0.5, 0, 0) and (0.5, 0.5, 0). Dispersions for these branches are shown in fig. 3.3 (black).

3.2.3 Lattice properties: theory and experiment

In this section, we will compare our experimental results with the predictions of the above described first-principles calculations. The theoretical predictions include phonon frequencies and their elongation patterns. Further, the wavevector-dependent strength of the electron-phonon coupling for each single phonon branch, $\lambda_{\mathbf{q},\omega}$, is calculated. The challenge of measuring the above mentioned properties is described in section 3.1.
First, the results for the phonon dispersion in the range of $0\,\mathrm{meV} < \mathrm{E} < 70\,\mathrm{meV}$ will be discussed. Thereafter, we will focus on some strongly anomalous branches, which are predicted to have extremely large intrinsic linewidths due to strong electron-phonon coupling.

Phonon dispersion in several high-symmetry directions

The proper assignment of experimentally observed to theoretically calculated phonon frequencies is based on a detailed comparison of the observed phonon intensities with the calculated stucture factors for the each **Q** point. A summary of the experimentally observed phonon frequencies is given in fig. 3.5. Branches shown in red or black refer to phonons of predominantly longitudinal or transverse polarization. In general, we observed approximately 3% higher phonon frequencies than predicted. In order to simplify the assignment of the experimental data to the calculated branches for the reader, we scaled the theoretical dispersion in fig. 3.5 with a factor of 1.03. As mentioned above, Reichardt et al. did not use the optimized crystal structure, but rather employed the experimental stucture of YNi_2B_2C, the unit cell volume V of which is about 2% larger than that of the optimized one [48]. Since in most compounds phonon frequenciees scale approximately as V^2, one expects the calculated frequencies to be about 4% lower than observed. In reality, the error is somewhat less than that.

As can be seen in fig. 3.5, the agreement between experiment and theory is extremely good. Only for the strongly anomalous branch around $\mathbf{q}$ = (0.4 - 0.7, 0, 0) a significant deviation from the calculated dispersion is observed. Even here, the anomaly is predicted qualitatively, only the strength of the electron-phonon coupling seems to be underestimated as will be discussed in more detail below. We note that we observed frequencies at room temperature which are in much better agreement with theory for this particular branch. The phonon frequencies at $\mathbf{q}$ = (0.5 - 0.65, 0, 0) were even higher than predicted, whereas in the other parts of the Brillouin zone we found nearly quantitative agreement.
We emphasize that not only the phonon frequencies, but also the phonon intensities were predicted quite well by the theory, which greatly helped to find favorable positions in momentum space.
Apart from the focus of our measurements on the three anomalous branches, we also made measurements of the linewidth at other wave vector values and for other phonon branches. They showed mostly good agreement with the *DFT* predictions. However, we found also some discrepancies. For instance, the linewidth of a zone center phonon at

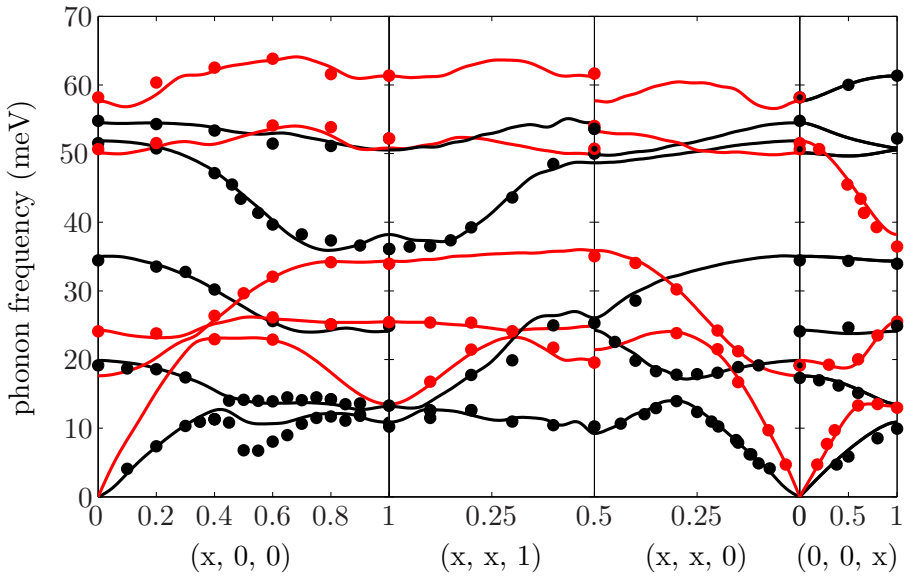

Figure 3.5: Comparison of the calculated (lines) and observed (dots) phonon dispersion in YNi_2B_2C at $T = 20\,\mathrm{K}$. Branches shown in red or black refer to phonons of predominantly longitudinal or transverse polarization. The horizontal axes denote different crystallographic directions in reciprocal lattice units (r.l.u.). Note that the theoretical results were scaled up by a factor of 1.03 (see text).

approximately 24 meV was found to be much smaller than predicted.

In the following, we will separately discuss the wave vector dependent behavior of three strongly anomaluous phonon branches:

- the transverse acoustic branch in the (100) direction,
- the transverse optic phonon branch, dispersing between 51 meV and 36 meV in the (100) and (xx1) directions and
- the transverse acoustic branch in the (110) direction.

All of them are c-axis polarized, which means that they are of transverse character (black in fig. 3.5) in the (100), (xx1) and (110) directions and of longitudinal character (red in fig. 3.5) in the (001) direction. All three phonon anomalies are accompanied by strong electron-phonon coupling. The dispersions, linewidths and polarization patterns will be discussed in detail and be compared to predictions of DFT and a BvK model.

Transverse acoustic branch in the (100) direction

The effects of strong electron-phonon coupling in YNi_2B_2C, i.e. softening of the phonon frequency and an enlarged linewidth for low temperatures, were first observed by Kawano et al. for the transverse acoustic phonon at $\mathbf{q}$ = (0.5-0.55, 0, 0) [24, 26] (see sect. 3.3.2). However, they concentrated on the superconducting regime and made no attempt to study the normal state lattice dynamical properties in detail.

In fig. 3.6 phonon scans of the TA phonon at $\mathbf{Q}$ = (0.3 - 0.7, 0, 8) are shown. All scans were taken at $T = 20$ K. The zeros of the scans are indicated by dashed colored lines. The well known phonon anomaly at $\mathbf{q}$ = (0.5, 0, 0) is clearly seen as extreme softening from $\mathbf{Q}$ = (0.4, 0, 8) to (0.5, 0, 8) of the TA phonon. We note that at $\mathbf{q}$ = (0.4, 0, 0) the dispersions of the TA and first TO branch indicate an anti-crossing behavior, i.e. an exchange of eigenvectors between these two branches. However, the calculated phonon patterns (fig. 3.4 (a)) do not reflect such an exchange of eigenvectors, although the calculated dispersions show a similar behavior as observed in experiment. However, a sudden change of the eigenvector of the TA phonon for $\mathbf{q} \geq$ (0.4, 0, 0) is obvious in the DFT calculation. The Y elongations, expected to be strong in an acoustic branch, are strongly reduced and large amplitudes of B and C dominate the pattern. There is, however, some evidence that an exchange of eigenvectors between the TA and TO branches takes place around $\mathbf{q}$ = (0.75, 0, 0) (see sect. 3.3.6). We note that this experimental observation is also supported by the calculated phonon pattern shown in fig. 3.4 (a).

The strong renormalization of the frequency from 11.3 meV to 7.0 meV from $\mathbf{q}$ = (0.4, 0, 0) to (0.5, 0, 0) is accompanied by an extreme increase of the phonon linewidth from $\Gamma = 1.4$ meV to more than 4 meV shown in fig. 3.7 (a) (black dots). The red line represents the DFT prediction. The strongly anomalous dispersion of the TA phonon hampers an accurate evaluation of the phonon linewidth because for energy scans in

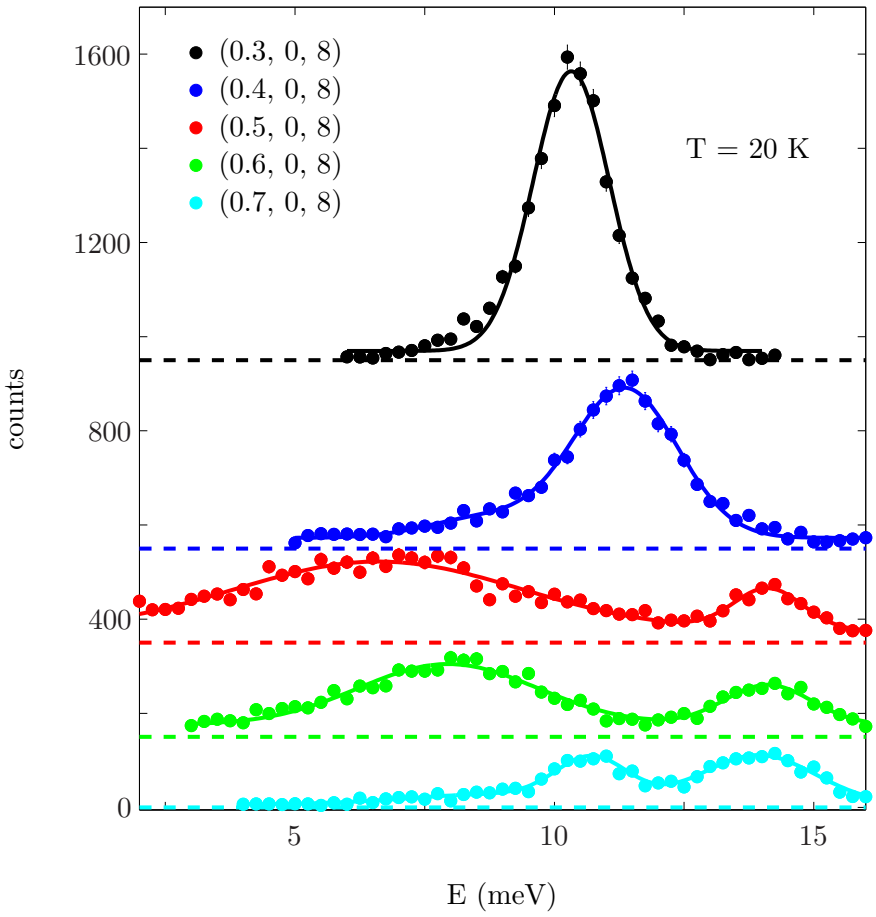

Figure 3.6: Energy scans taken at $\mathbf{Q}$ = (0.3 - 0.7, 0, 8) at T = 20 K. The low energy peaks correspond to the TA phonons. For the higher wave vectors the first TO phonon is visible as well. Solid lines are guides to the eye. Dashed lines denote the offsets included for the sake of clarity.

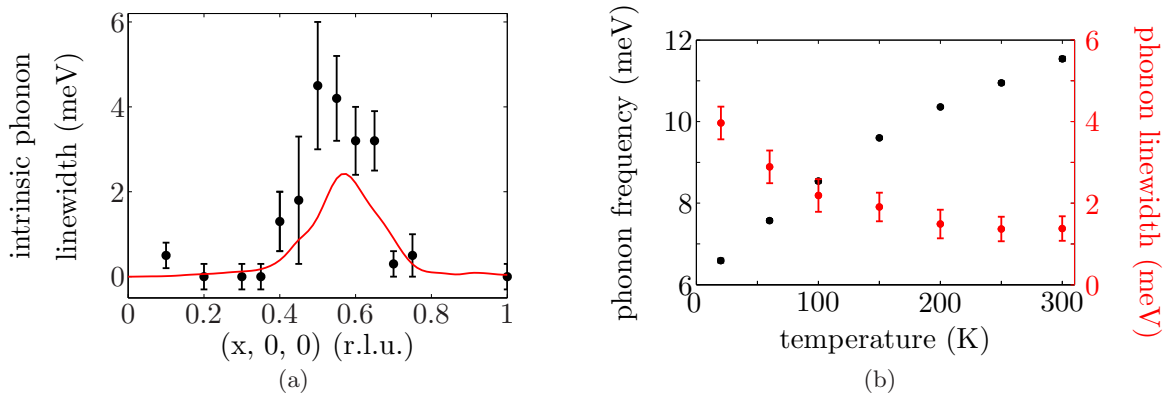

Figure 3.7: (a) Comparison of observed and calculated wave vector dependent intrinsic phonon linewidths for the TA branch in the (100) direction at $T = 20\,\mathrm{K}$ and (b) the temperature dependent phonon frequencies (black) and linewidths (red) measured at $\mathbf{Q} = (0.5, 0, 8)$.

the range of $\mathbf{q} = (0.45 - 0.55, 0, 0)$ the finite $\mathbf{q}$ resolution ($\Delta q = 0.05\,\mathrm{r.l.u.}$) strongly contributes to the observed linewidth resulting in large errorbars for these wavevectors. Nonetheless, it is clear that the intrinsic linewidths are very large around $\mathbf{q} = (0.5, 0, 0)$. Fig. 3.7 (a) shows that the behavior of the phonon linewidth is qualitatively well described by DFT, but quantitatively the phonon linewidth, i.e. the strength of the electron-phonon coupling, is underestimated by approximatly a factor of 2, consistent with the too small predicted softening of the phonon frequency around $\mathbf{q} = (0.5, 0, 0)$. Further, the maximum of the linewidth, which is expected at $\mathbf{q} = (0.6, 0, 0)$, is observed rather near $(0.5, 0, 0)$.

As discussed in sect. 3.1.2, the temperature dependence of the phonon frequency and the phonon linewidth is altered in the presence of strong electron-phonon coupling. The temperature evolution of the phonon frequency and linewidth at $\mathbf{q} = (0.5, 0, 0)$ from 20 K to 300 K is shown in fig. 3.7 (b). There is clearly an anomalous softening and broadening towards lower temperatures. Such a strong temperature dependence is typical of a strong electron-phonon coupling due to Fermi surface nesting.

For $\mathbf{q} \approx (0.5, 0, 0)$ a pronounced Fermi-surface nesting was predicted by band-structure calculations [50, 51]. The strenght of electron-phonon coupling features seen by inelastic neutron scattering is depending on two factors: an eventual Fermi surface nesting and the responsible matrix elements of electron-phonon scattering. First, a strong Fermi surface nesting enhances the phase space for the matrix element dramatically. Thus, such a nesting feature will lead to strong electron-phonon coupling effects even if the corresponding matrix element is not exceptionally large. On the other hand, large values of the matrix elements may give rise to strong electron-phonon coupling without Fermi surface nesting. The presence of the nesting, however, is crucial to the observed behavior,

Q	TA			T0		
	EXP	DFT	BvK	EXP	DFT	BvK
(0.0, 0, 8)	-	154	153	49	24	16
(0.1, 0, 8)	153	153	153	48	24	16
(0.2, 0, 8)	162	150	156	-	25	15
(0.3, 0, 8)	192	149	162	50	25	11
(0.4, 0, 8)	155	161	172	-	12	0.1
(0.5, 0, 8)	111	146	97	35	26	62
(0.6, 0, 8)	74	99	53	44	54	76
(0.7, 0, 8)	37	28	26	57	80	62
(0.8, 0, 8)	15	0.03	11	52	52	35
(0.9, 0, 8)	27	2	4	27	27	13

Table 3.1: Comparison of observed and calculated (DFT and BvK) phonon intensities for the TA and the TO phonon branch measured at $\mathbf{Q}$ = (0 - 0.9, 0, 8) for $T = 20\,\mathrm{K}$. Observed intensities are corrected for $\mathbf{Q}^2$ and $1/\omega$ in the neutron scattering cross section.

because the smearing of the nesting towards higher temperatures reduces the phase space for the electron−phonon scattering process, resulting in a hardened frequency and a smaller linewidth for higher temperatures.

Measured and calculated intensities along $\mathbf{Q}$ = (0 - 0.9, 0, 8) are listed in tab. 3.1 for the TA acoustic and first TO phonon branch. Calculations are either based on DFT or an empirical BvK model. Observed intensities are corrected for the factors $\mathbf{Q}^2$ and $1/\omega$ in the neutron scattering cross section. The calculated structure factors are normalized to the experimental value at $\mathbf{Q}$ = (0.1, 0, 8). We note that the structure factors of acoustic branches are model independent in the long wavelength limit.

In fig. 3.4 it was shown that the eigenvectors in the region of the phonon anomaly in the (100) direction differ considerably in the two calculations. However, the phonon intensities calculated for both sets of eigenvectors for measurements at $\overrightarrow{\tau}$ = (0, 0, 8) do not differ strongly from each other, which makes it difficult to discriminate between the two models. Both models predict the observed gain in intensity of the TA phonon in the first half of the Brillouin zone, followed by a sharp drop in intensity, which is slightly and more strongly overestimated by the BvK model and the DFT calculation, respectively. From $\mathbf{Q}$ = (0.8, 0, 8) to (0.9, 0, 8) the DFT indicates the experimentally found re-increase of the TA structure factor, although the predicted increase is an order of magnitude to small. In contrast, the BvK model predicts a decreasing intensity all the way to the zone boundary. Also for the TO branch both calculations qualitatively reproduce the evolution of the phonon intensities. However, the quantitative deviations

to the measurement are smaller in the whole Brillouin zone for the DFT structure factors. In conclusion, a more detailed investigation of the phonon intensities in different Brillouin zones would be necessary to resolve the question of the correct phonon eigenvectors.

Transverse optic branch dispersing between 51 meV and 36 meV

The TO phonon branch exhibiting a phonon anomaly at the zone boundary was studied in three different directions, namely the (100), the (xx1) and the (001) directions, in two runs: first on the TAS DAS PUMA in Munich and later on our own instrument at the LLB, Saclay. The dispersions for these phonon branches, shown in fig. 3.5, are in good agreement with the DFT predictions, apart from the general underestimation of 3%. Only the weak local minimum around $\mathbf{q}$ = (0.8, 0, 0) predicted by theory was not observed in experiment.
The results for the temperature dependence of the frequency of the TO phonon at $\mathbf{Q}$ = (0, 0, 7) from both experiments are in good agreement with each other (fig. 3.9 (b)). In contrast, we observed no change of the linewidth in the LLB data, but a broadening towards lower temperatures in the Munich data (fig. 3.9 (c)). However, there are two facts, which raise doubts on the quality of the PUMA data.

- The lineshape of the LLB data are much more lorentzian-like, as expected for strong coupling phonons (fig. 3.8).
- On *PUMA* we had extreme problems determining the temperature dependent linewidth, caused by, probably, two spurious peaks, one of them obvious (fig. 3.8), the other somewhat hidden in the low-energy side of the phonon and exhibiting a very strong temperature dependence.

Therefore, we have more confidence into the *1T* data, which do not see a significant broadening of the TO phonon with decreasing temperature. Nevertheless, the temperature dependence of the phonon frequency and the observed large intrinsic linewidth, which is in good agreement with the DFT calculations, indicate that strong electron-phonon coupling is present.
In fig. 3.9 (a) the intrinsic linewidths of the anomalous high-energy TO branch along (100) and (xx1) are shown. The red line represents the DFT prediction, which is in good agreement with experiment. Our experimental data indicate that the maximum of the intrinsic linewidth occurs around $\mathbf{q}$ = (0.1, 0.1, 1) whereas the calculation predicts a monotonic decrease. However, this can be considered as a minor point. We emphasize that the general behavior of the linewidths between (0, 0, 1) and (0.5, 0.5, 1) is the same in both theory and experiment.

Transverse acoustic branch in the (110) direction

A previously unkown phonon anomaly was predicted for the TA phonons at the zone boundary in the (110) direction, the so-called M-point. In the temperature dependence

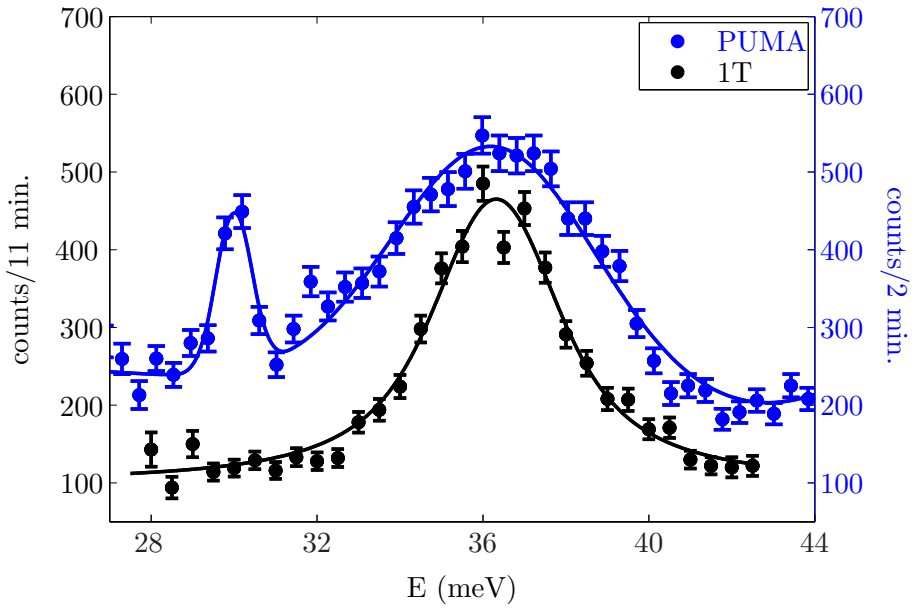

Figure 3.8: Low temperature energy scans at $\mathbf{Q}$ = (0, 0, 7) taken on the TASs PUMA at the FRM-II (blue) and 1T at the LLB (black). The sharp peak in the low energy tail of the phonon is spurious.

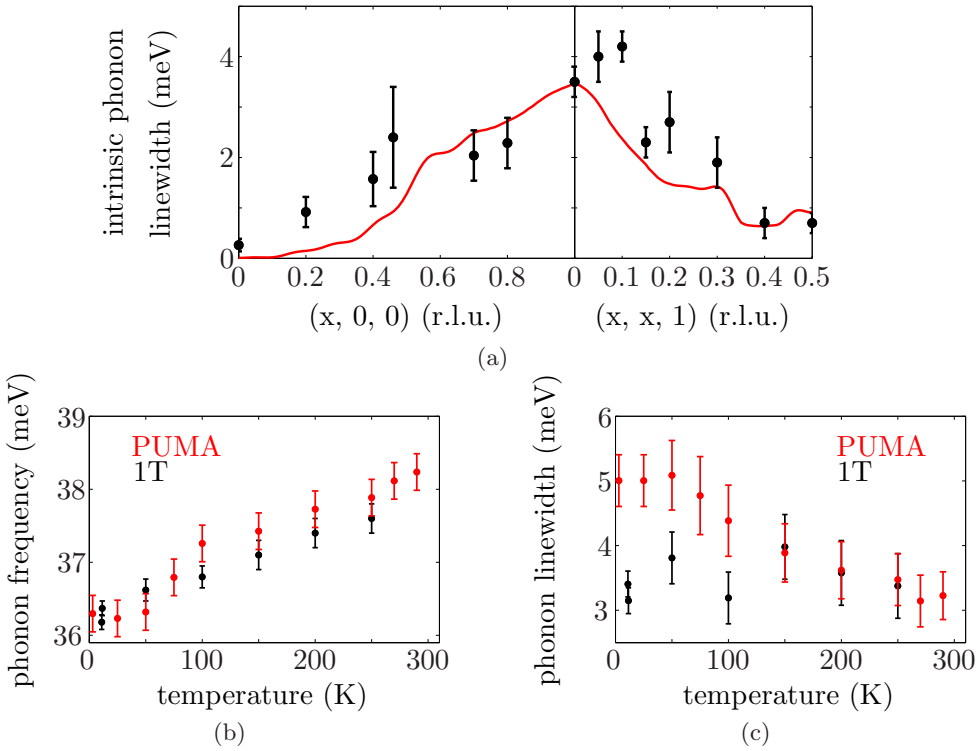

Figure 3.9: (a) Comparison of observed and calculated wave vector dependent intrinsic phonon linewidths for the TO branch in the (100) and the (xx1) directions at low temperatures, (b) the temperature dependent phonon frequencies and (c) linewidths measured at $\mathbf{Q}$ = (0, 0, 7) on the TASs PUMA (red) and 1T (black).

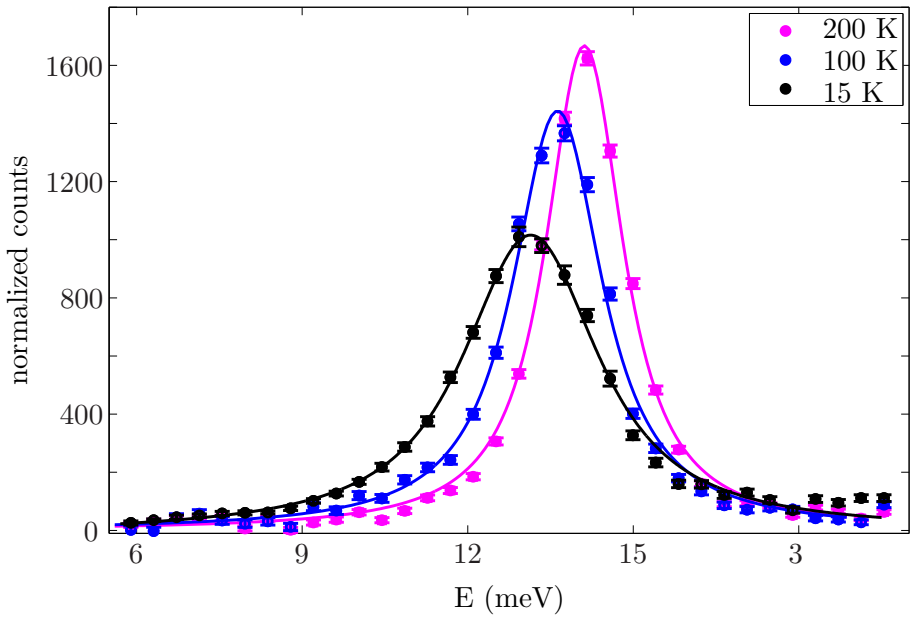

Figure 3.10: Energy scans taken at the M-point phonon at various temperatures. The counting rates were normalized to a monitor of $6 \cdot 10^6$ and corrected for the Bose factor and $1/\omega$ in the scattering cross-section.

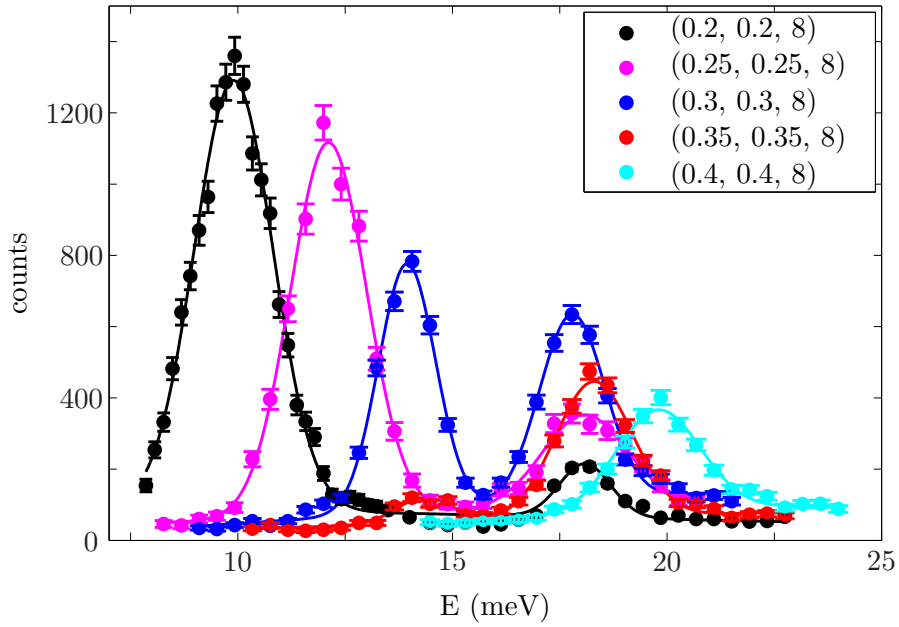

Figure 3.11: Energy scans taken at $\mathbf{Q}$ = (x, x, 8), $x = 0.2 - 0.4$ at $T = 3\,\mathrm{K}$. Lines are guides to the eye.

of the frequency and linewidth of the TA phonon at $\mathbf{Q}$ = (0.5, 0.5, 7) ($\mathbf{q}$ = (0.5, 0.5, 0) with $\overrightarrow{\tau}$ = (-1, 0, 7)) a strong coupling behavior, similar to that at $\mathbf{Q}$ = (0.5, 0, 8), was observed as shown in fig. 3.10. Lines are fits to the data with a Lorentzian convoluted with a Gaussian for the experimental resolution of about 1 meV. The frequency softens from 11.1 meV at $T = 200\,\mathrm{K}$ to 10.2 meV at $T_c = 15\,\mathrm{K}$. The extracted intrinsic linewidth (FWHM) increases from $\Gamma = 1\,\mathrm{meV}$ to $\Gamma = 2.4\,\mathrm{meV}$ in the same temperature range. A summary of the temperature dependencies of the phonon frequencies and phonon linewidths observed at $\mathbf{Q}$ = (0.5, 0.5, 7) are shown in fig. 3.12 (b).

The measurement of the phonon anomaly at the M-point is complicated by unfavorable structure factors. In fact, the TA phonon at $\mathbf{q}$ = (0.5, 0.5, 0) has its by far largest structure factor in the Brillouin zone of $\overrightarrow{\tau}$ = (-1, 0, 7) for the absolute wave vector $\mathbf{Q}$ = (0.5, 0.5, 7). In other Brillouin zones the initially large structure factor of the TA phonon is transferred to the nominally first TO phonon branch. The anti-crossing takes place around $\mathbf{q}$ = (0.3, 0.3, 0) and is illustrated for the (0, 0, 8) Brillouin zone in fig. 3.11. The branch with acoustic character continues its upward dispersion up to the zone boundary and nominally becomes the first TO branch for $\mathbf{q} > (0.3, 0.3, 0)$. On the other hand, the eigenvector of the TO branch is moved to the lower branch for $\mathbf{q} > (0.3, 0.3, 0)$[2]. A detailed analysis of this anti-crossing is given in table 3.2. It shows

[2]Throughout this work, the nominal description of branches is used, e.g. the strong coupling phonon at the zone boundary in (110) direction is referred to as an acoustic phonon, despite its unusual atomic

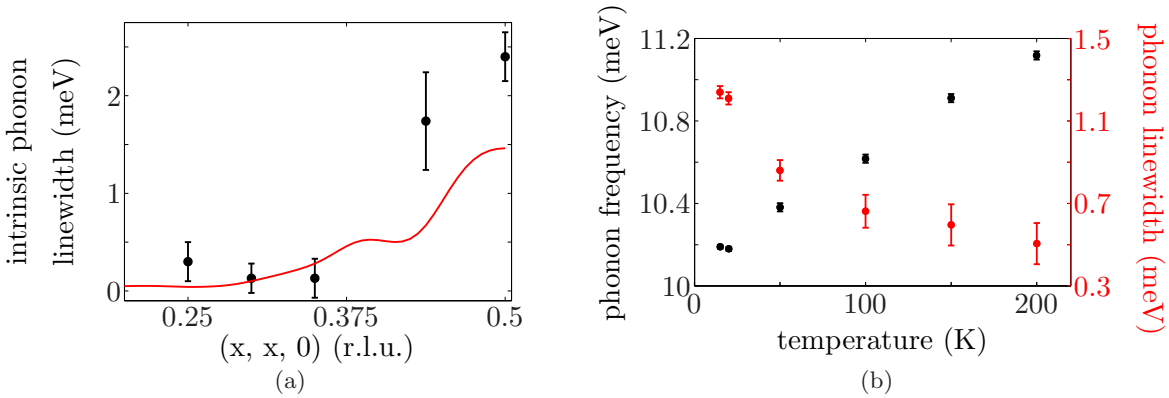

Figure 3.12: (a) Comparison of observed and calculated wave vector dependent intrinsic phonon linewidths for the TA branch in the (110) direction at $T = 20\,\mathrm{K}$ and (b) the temperature dependent phonon frequencies (black) and linewidths (red) measured at $\mathbf{Q} = (0.5, 0.5, 7)$.

the calculated structure factors and the experimentally measured integrated intensities for the scans shown in fig. 3.11. The structure factors are normalized to the integrated intensity of the TA phonon at $\mathbf{q} = (0.2, 0.2, 8)$. Measured intensities are corrected for the factor $1/\omega_{phonon}$ in the one-phonon cross-section (eq. 3.2).
The agreement between calculated and observed intensities is very satisfactory although not as good as for the phonon frequencies. We note that intensities are invariably less well predicted than frequencies by all kind of theories. Therefore, the agreement shown in tab. 3.2 can be taken as confirmation of the accuracy of the theory.

By tilting our sample holder a few degrees out of the scattering plane, we gained access to points away from the M-point with good structure factors. The results are displayed in fig. 3.12 (a) in comparison to the DFT calculation (red line). The onset of strong electron-phonon coupling as function of wave vector seems to be predicted with good accuracy. However, the agreement for larger wave vectors is only qualitative, i.e. the strength of the electron-phonon coupling at the zone boundary is clearly underestimated as was the case for the TA phonon at $\mathbf{q} = (0.5, 0, 8)$.
In contrast to the phonon anomaly at $\mathbf{q} = (0.5, 0, 0)$, nothing is known about a nesting feature for $\mathbf{q} = (0.5, 0.5, 0)$. An energy integrated $\mathbf{q}$ resolved calculation by R. Heid showed also an extremely enhanced phase space at this wave vector. However, no single strong nesting feature seems to be responsible, but many small pockets in the Fermi surface, connected by this particular wave vector, are contributing to the sharp peak in the wave vector dependent phase space. Whether the corresponding electron-phonon scattering matrix elements are large, too, cannot be answered by our present knowledge.

As for the TA phonon branch in the (100) direction, the polarization patterns for the M-

displacement pattern.

Q	TA		T0	
	EXP	DFT	EXP	DFT
(0.2, 0.2, 8)	3000	3000	600	820
(0.25, 0.25, 8)	3000	2320	1700	1430
(0.3, 0.3, 8)	1800	680	2300	3000
(0.35, 0.35, 8)	200	140	1700	3270
(0.4, 0.4, 8)	<20	0	1700	3270

Table 3.2: Comparison of integrated intensities and calculated structure factors for the transverse acoustic (TA) and the first transverse optic (TO) branch at $\mathbf{Q}$ = (0.2, 0.2, 8) - (0.4, 0.4, 8) (scans shown in fig. 3.11). The DFT structure factors are normalized to the observed intensity of the TA phonon at $\mathbf{q}$ = (0.2, 0.2, 8). Integrated intensities are corrected for the factor $1/\omega$. All measurements were done at low temperatures.

Q	TA		
	EXP	DFT	BvK
(0.2, 0.2, 4)	8.17	8.17	8.17
(0.5, 0.5, 7)	11.74	12.21	3.66
(0.5, 0.5, 8)	<0.25	0.002	2.06
(0.5, 0.5, 5)	1.64	1.45	1.27
(0.5, 0.5, 6)	0.28	0.03	2.33

Table 3.3: Comparison of calculated and observed phonon intensities with the aim to check the predicted elongation pattern of the M-point phonon at $E = 10\,\mathrm{meV}$. The calculations were based on DFT and a Born-von-Karmann model (BvK).

point are qualitatively different in predictions by the DFT and a BvK model (fig. 3.4). Tab. 3.3 summarizes the observed integrated intensities of the TA phonon at the M-point and compares them to the calculated structure factors. The experimental values are corrected for $\mathbf{Q}^2$ and $1/\omega$. The structure factors were normalized to the corrected integrated intensity of the TA phonon at $\mathbf{Q} = (0.2, 0.2, 4)$.
The predicted DFT values are well within the error bars of the measurement, whereas the BvK model differs considerably for three out of four $\mathbf{Q}$ points. Thus, we conclude that for the TA phonon at the M-point the eigenvector predicted by DFT with large oscillations of the light B and C atoms is adequate.

3.3 Phonons as a probe for the anisotropy of the superconducting energy gap

3.3.1 Influence of the superconducting energy gap on phonon linewidths - early results

The first measurements of the influence of superconductivity on phonons were done in 1973 by J. D. Axe and G. Shirane on Nb_3Sn ($T_c = 18.3\,K$) [52]. They observed a reduction of the linewidth of relatively strong coupling acoustic phonons with energies $\hbar\omega_{phonon}$ smaller than the superconducting energy gap $2\Delta(0)$ on cooling through the superconducting transition temperature. Shortly after, Shapiro et al. made a very careful measurement of phonon linewidth effects across the superconducting transition temperature in Niobium ($T_c = 9.2\,K$) [10]. In particular, they made a series of scans for transverse acoustic phonons, which show a sudden change in the phonon linewidth on crossing T_c similar to Nb_3Sn. Fig. 3.13 shows data for the observed phonon linewidth 2Γ versus temperature in Niobium for three phonons with different frequencies. The inset shows the phonon frequency in energy versus temperature for which the observed linewidths are displayed. Phonons with different energies were measured at different wave vectors along (110). The inset makes clear that the energy of phonon (A) corresponds to the gap energy at a somewhat higher temperature $T(2\Delta)$ than for phonon (B). Neglecting this difference, the same behavior of a sudden sharpening was observed. For low temperatures, the phonon lineshapes become resolution limited (horizontal line denotes the instrumental resolution). On the other hand, phonon (C) with $\hbar\omega_{phonon} > 2\Delta(0)$ becomes broader for $T < T_c$. This can be qualitatively understood by considering the enhancememt of the electronic density of states above the energy gap, which boosts the electron-phonon coupling strength. The right-hand scale for $2\Gamma^{e-p}$ of fig. 3.13 denotes the authors' extraction of the intrinsic phonon linewidth due to electron-phonon coupling.
For each phonon energy denoted by (A) or (B), Shapiro et al. extracted a value $2\Delta(T)$, where $2\Delta = \hbar\omega_{phonon}$ and T is determined by $2\Gamma(T) = (2\Gamma(0) + 2\Gamma(T_c))/2$. Our calculations using the theory of Allen et al. [53] discussed in sect. 3.3.3 have shown that this procedure is only valid for phonon energies much smaller than $2\Delta(0)$, whereas for phonons with $\hbar\omega_{phonon} \approx 2\Delta(0)$ the determination of $2\Delta(T)$ requires calculations based on the theory discussed later.

3.3.2 Superconductivity induced effects on the phonon lineshape in the borocarbides

The strongest changes in the phonon lineshape on entering the superconducting state ever observed were reported for compounds of the borocarbide family. Kawano et al. reported anomalous phonon scattering below T_c for YNi_2B_2C [24]. The main experimental observation is shown in fig. 3.14 (a). The very broad phonon peak observed

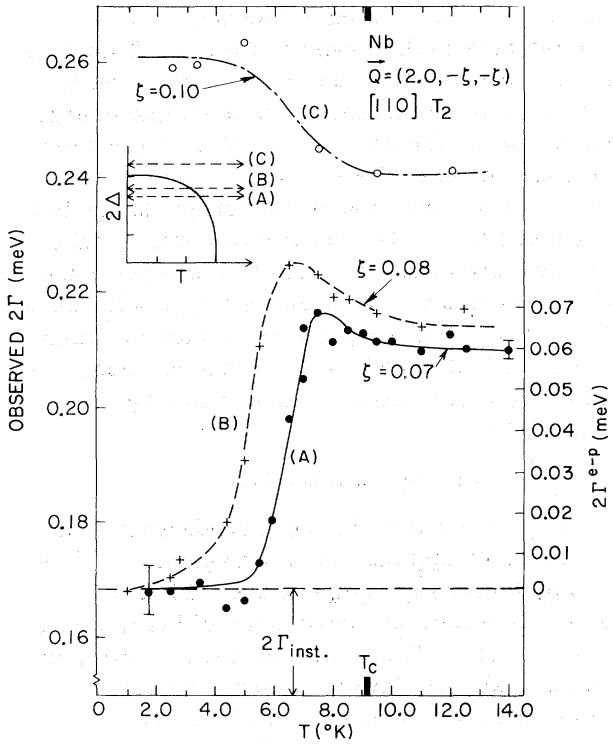

Figure 3.13: Temperature dependence of the experimental linewidth, 2Γ, of several transverse $(\xi\xi 0)$ phonons in Nb. Curves A and B have $\hbar\omega_{phonon} < 2\Delta(0)$ and curve C $\hbar\omega_{phonon} > 2\Delta(0)$. The dashed line denotes the experimental resolution. Right-hand scale indicates the intrinsic phonon linewidth, related to electron-phonon coupling. Figure is taken from ref. [10].

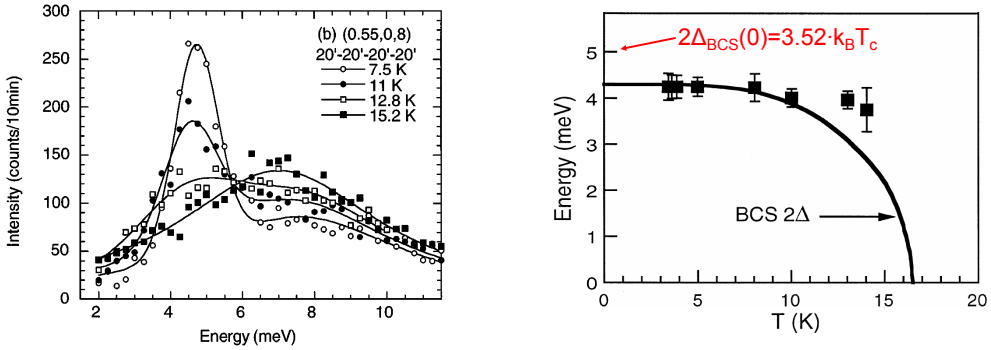

(a) YNi_2B_2C [24] (b) $LuNi_2B_2C$ [28]

Figure 3.14: (a) Constant **Q** scans of the transverse acoustic phonon in YNi_2B_2C at **Q** = (0.55, 0, 8) for $T \leq T_c$ [24]. (b) Energy of the sharp peak observed below T_c in $LuNi_2B_2C$ (results similar to (a)). Solid line denotes the temperature dependence of $2\Delta(T)$ according to weak coupling BCS theory as given in ref. [28]. Red arrow denotes the correct BCS weak coupling value of $2\Delta(0) = 5\,\text{meV}$.

at $T_c = 15.2\,\text{K}$ seems to loose spectral weight on entering the superconducting state, while a 'new' peak is emerging in the low energy tail. Measurements with an applied magnetic field proved the connection between this altered lineshape and the superconducting state. Kawano et al. [24,26] speculated in favor of a new excitation emerging in the superconducting state.
Motivated by the discovery of this anomalous phonon behavior, Stassis et al. [25] made measurements on the Lu borocarbide, $LuNi_2B_2C$ ($T_c = 16.5\,\text{K}$). Similar to YNi_2B_2C, they found a sharp peak in the superconducting state. However, a different interpretation was given in terms of a phonon mode coupling model, where, for $T < T_c$, the acoustic mode is represented by the sharp peak and the optic mode by the broad hump at higher energies. In a second publication [28], the authors made reference to a theory published by P.B. Allen et al. [53] (discussed in detail in sect.3.3.3). According to Allen et al. the sharp peak in the superconducting state is directly connected to the opening of the energy gap and cannot be regarded as a new excitation. Stassis et al. concluded that the frequency of the sharp peak corresponds to $2\Delta(T)$ and compared it to the BCS weak coupling superconducting energy gap $2\delta(T)$ (fig. 3.14 (b)). Obviously, the peak frequency is not following the BCS like behavior for $2\Delta(T)$. Still, Stassis et al. claimed that their observations revealed $2\Delta(T)$. We note the following shortcomings of their analysis: Firstly, the standard BCS value for a superconductor like $LuNi_2B_2C$ with $T_c = 16.5\,\text{K}$ is $2\Delta(0) = 5.0\,\text{meV}$ (red arrow in fig. 3.14 (b)) and not 4.3 meV. Secondly, as will be discussed below, the peak frequency does not coincide with 2Δ in Allen's theory, but is

below the gap value. It is only close to T_c that the peak frequency is approaching $2\Delta(T)$. Here, however, its spectral weight is reduced making it difficult to observe. Very close to T_c, there is only a sharp intensity cut-off right at 2Δ. However, the expected features close to T_c were not observed neither by Kawano et al. nor by Stassis et al. because of insufficient statistics. As will be discussed later, our measurements with much better statistics did confirm the temperature dependent changes predicted by the theory of Allen et al..

3.3.3 Allen's theory for the Neutron-scattering profile of Q $\neq$ 0 phonons in BCS superconductors

Motivated by the observation of unusual lineshapes in the superconducting state of $LuNi_2B_2C$ and YNi_2B_2C, P. B. Allen et al. resumed their theoretical treatment of the effects of superconductivity on the phonon lineshape in BCS superconductors [54–56]. The work was published in 1997 [53] and referred in particular to experimental results described in Refs. [24] and [25]. The calculated scattering law was tested for the case of Niobium [10] and then applied to the borocarbides[3]. This theory has only three independent parameters, two of which are fixed by the experimentally measured normal state properties just above T_c.

- ω_N - The normal state phonon frequency.
- γ_N - The half intrinsic phonon linewidth at half maximum in the normal state, due to electron-phonon coupling.
- $2\Delta(T)$ - The temperature dependent value of the superconducting energy gap.

The explicit formula of the scattering law and the included variables are the following:

$$S(Q,\omega) = \frac{4\omega r_Q \omega_N^2 \gamma_S/\gamma_N}{\left[\omega^2 - \omega_N^2 - 2\omega_N^2 r_Q RE(\delta\Pi)/\gamma_N\right]^2 + \left[2\omega r_Q \omega_N \gamma_S/\gamma_N\right]^2} \tag{3.11}$$

Π is the phonon self-energy and γ_s/γ_N the ratio of superconducting to normal values of the imaginary part of the phonon self-energy. The impact of the ratio $r_Q = \gamma_N/\omega_N$ for the Eliashberg equation is already discussed in chapter 3.2.2 (eq. 3.7). In the theory of Allen et al. it determines together with the ratio $\omega_N/2\Delta(T=0)$ the strength of the superconductivity induced effect on the phonon lineshape. The largest effects are expected for large r_Q and $\omega_N/2\Delta(T=0) \approx 1$.
There are three qualitatively different scenarios for the lineshape in the superconducting state depending on the ratio of the phonon frequency ω_N over the zero temperature gap value $2\Delta(T=0)$.

[3] We tested an implementation of the theory for ourselves and could quantitatively reproduce data for the temperature dependent linewidth of the transverse phonon at $\mathbf{q}$ = (0.07, 0.07, 0) (phonon (A)), shown in fig 3.13.

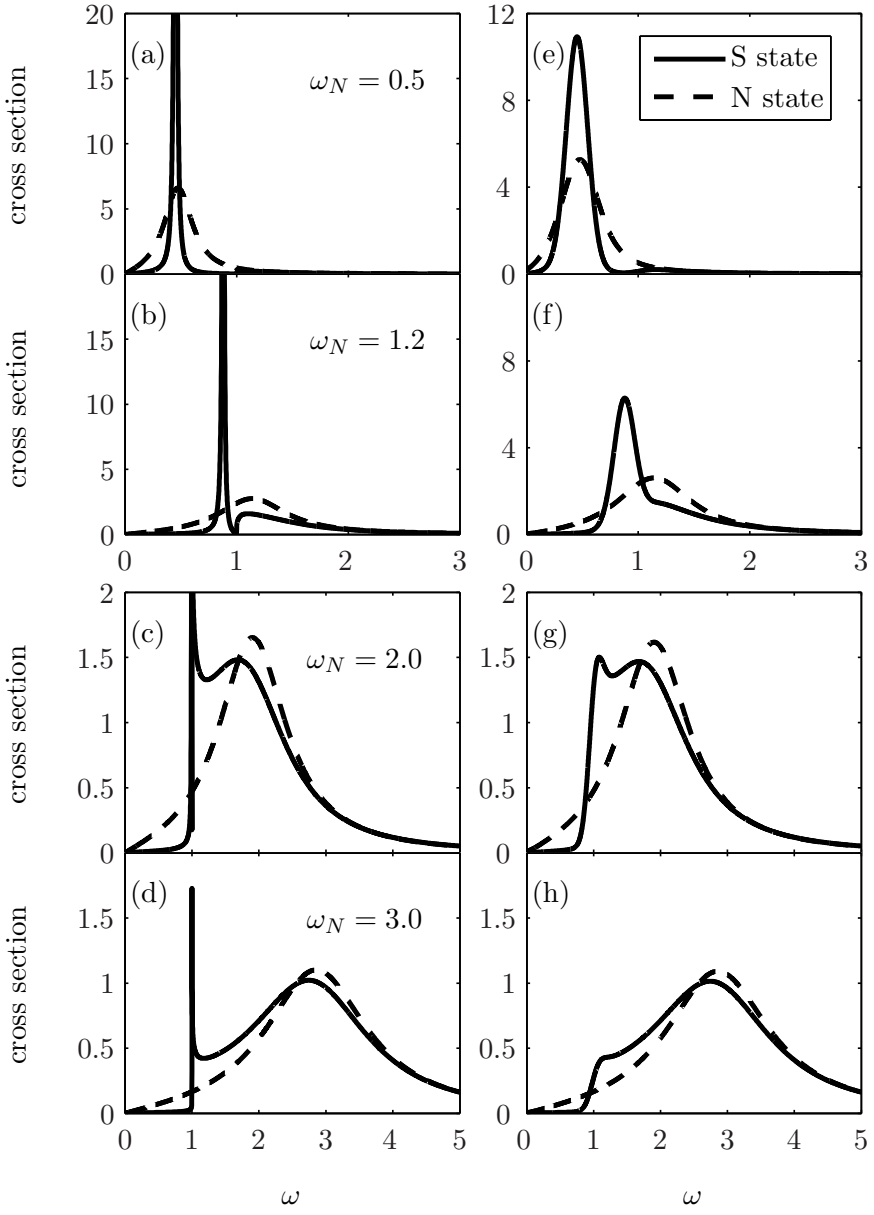

Figure 3.15: Calculated line shapes at ω_N = (a) 0.5, (b) 1.2, (c) 2.0 and (d) 3.0 (units of 2Δ) at $T/T_c = 0.15$ (solid lines) and $T \geq T_c$ (dashed lines). For all calculations $r_Q = 0.3$ was used. Panels (e) (h) are convoluted with an instrumental broadening $\Gamma = 0.13$ (units of 2Δ). The calculations were done using the theory of Allen.

1. $\frac{\omega_N}{2\Delta(T=0)} < 1$
   For this configuration, the lifetime of the phonon in the superconducting state is increased because electronic decay channels are frozen out by the superconducting gap. Thus the phonon linewidth becomes resolution limited. This behaviour is seen in Refs. [52] fig.1 and [10] fig.2 in the superconductors Nb_3Sn and Nb, respectively.

2. $1 < \frac{\omega_N}{2\Delta(T=0)} < 1 + r^*$
   The phonons studied by Kawano et al. and Stassis et al. fall into this parameter range. Due to a logarithmic singularity of $Re(\delta\Pi_s)$ and a small imaginary part of Π at low temperatures, there is a resonance at a certain energy. If $\omega_N/2\Delta$ is within $1 \pm r_Q$, the resonance captures most of the spectral weight at low temperatures and dominates the phonon spectra. Allen called this resonance below 2Δ a *mixed vibrational/superelectronic collective excitation*.

3. $\frac{\omega_N}{2\Delta(T=0)} > 1 + r^*$
   Here, the low frequency tail of the phonon peak, which lies below the gap, is pushed up in frequency to form a narrow spike at the gap energy on entering the superconducting state. The spike itself is washed out by the finite experimental resolution Γ. The theory of Allen et al. predicts not only the suppression of the spectral weight below 2Δ just mentioned, but also a downward shift of the intensity maximum and an intensity build-up on the low energy side of the peak.

The value of $r^* = \omega_N^*/2\Delta$ for which the behavior changes from case 2 to 3 strongly depends on the ratio $r_Q = \gamma_N/\omega_N$. For example, the M-point phonon has a normal state frequency $\omega_N = 1.79 \cdot 2\Delta$ and can be clearly assigned to case 3 ($r_Q = 0.122$), while the TA phonon at $\mathbf{Q} = (0.5, 0, 8)$ with a normal state frequency of $\omega_N = 1.72 \cdot 2\Delta$ is a case 2 phonon ($r_Q = 0.47$). For $r_Q = 0.3$ as used in the calculation for fig. 3.15, r^* lies between 2 and 2.5 approximately.
Fig. 3.15 shows the calculated phonon spectra for ω_N = (a) 0.5, (b) 1.2, (c) 2.0 and (d) 3.0 (units of 2Δ) at $T/T_c = 0.15$ (solid lines) and $T \geq T_c$ (dashed lines). Panels (e)−(h) are convoluted with an experimental resolution of $\Gamma = 0.13$ (units of 2Δ). We used an implementation of the Allen theory programmed by R. Heid[4]. The parameter sets (ω_N, r_Q) are chosen in a way that the evolution from case 1 (a) to case 2 (b) and to case 3 (d) can be seen very easily. With increasing ω_N, the frequency of the resonance approaches 2Δ; simultaniously the captured spectral weight is reduced. Finally, the sharp feature is located at 2Δ but is washed out by the experimental resolution (fig. 3.15 (d) and (h)).
Thus, the energy value of the superconducting energy gap is most easily identifiable in the convoluted curves for case 3, because the position of the gap directly coincides with the dominant feature in the superconducting state - the resolution limited intensity cut-off at 2Δ. On the other hand, case 1 contains no information about the absolute value of the gap and for case 2 the energy position of the sharp resonance peak relative to 2Δ is below the gap value and has to be inferred from a calculation based on realistic parameters for a precise determination of the gap value.

[4]Research Center Karlsruhe, Intitute for solide state physics

3.3.4 Opening of the superconducting energy gap in phonon spectroscopy

In YNi_2B_2C, the phonon best suited for extracting the superconducting gap from a careful study of the low temperature lineshape is the endpoint of the transverse acoustic branch in the (110) direction. On cooling from $T = 200\,\mathrm{K}$ to a temperature just above T_c, this phonon softens by about 10% and broadens substantially, indicative of a strong electron-phonon coupling (figs. 3.10 and 3.12 (b)). However, the lineshape remains Lorentzian to a very good approximation.

On further cooling through the superconducting transition temperature, the lineshape starts to deviate strongly from a Lorentzian. In particular, there is a steplike increase at a certain energy E_s, which gradually increases as the temperature is lowered (fig. 3.16 (a)). The experimental data at $T = 3\,\mathrm{K}$ clearly resemble the calculated curve in panel (h) of fig. 3.15. Hence, the intensity step is indicative of $2\Delta(T = 3\,\mathrm{K})$. The temperature evolution of this intensity drop is easily identifiable in the raw data and thus, the gap energy can be extracted with high precision as a function of temperature from an accurate determination of the low frequency part of the phonon spectral function at various temperatures.

In order to extract $2\Delta(T)$ with the utmost precision, we calculated phonon spectra with parameters extracted from a fit of the scattering law (eq. 3.11), convoluted with the experimental resolution of $\Gamma = 1\,\mathrm{meV}$, to the $T = 15\,\mathrm{K}$ data. The calculated curve normalized in a way as to match the neutron counts is plotted as a black line in fig. 3.16 (a). Panel (b) shows the unscaled curves for $T = 15\,\mathrm{K}$, $12\,\mathrm{K}$ and $3\,\mathrm{K}$. For $T < T_c$ the temperature enters the theory via the temperature dependence of $2\Delta(T)$, which was chosen as to represent the observed intensity drop at the gap energy. The calculated curves reproduce the observed spectra qualitatively very well. However, it is obvious that the theory quantitatively underestimates the effect. Therefore, the calculated curve in fig. 3.17 (blue line) was scaled by a factor of 1.35 in order to reproduce the height of the intensity cut-off and thus to facilitate to extract the value of 2Δ (red dashed line in fig. 3.17) for the given temperature.

For $T > 10\,\mathrm{K}$, the step-like increase of the intensity at $E = 2\Delta(T)$ becomes rather weak and broad. Therefore, the method to extract $2\Delta(T)$ demonstrated in fig. 3.17 becomes inaccurate. Here, a better method is to plot the intensities for fixed energy transfer versus temperature as was done in fig. 3.18[5]. For small energy values, these plots exhibit sharp superconductivity induced features. Hence, this kind of plotting enables an accurate determination of $2\Delta(T)$ at temperatures close to T_c. The arrows shown in fig. 3.18 indicate the temperature at which 2Δ is equal to the energy transfer.

The temperature dependent gap value deduced in this way is plotted in fig. 3.21. The experimental curve (red solid line) qualitatively deviates somewhat from the BCS weak-coupling behavior (black dashed line), which is not surprising for a superconductor with T_c as high as $15.5\,\mathrm{K}$. Likewise, the value of the zero temperature gap is indicative of strong coupling because the ratio $2\Delta/k_BT_c = 4.3$ exceeds considerably the weak coupling limit of 3.55.

[5] The measurement was done in units of THz. $1\,\mathrm{THz} = 4.136\,\mathrm{meV}$

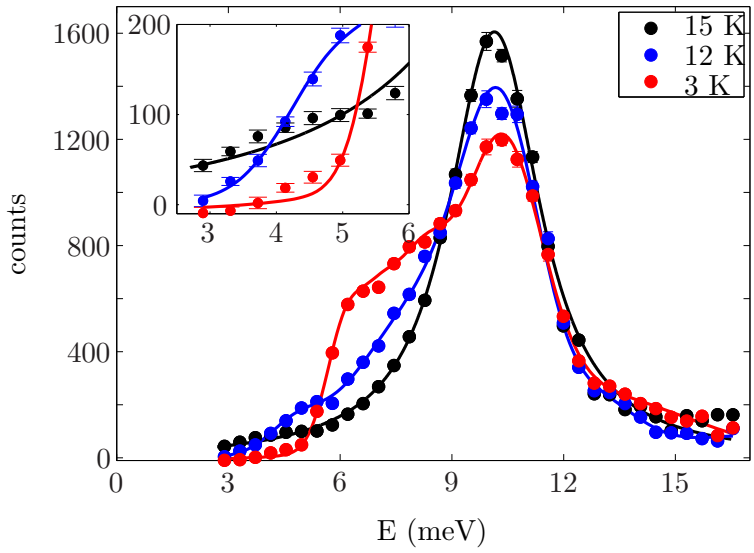

(a) Experiment

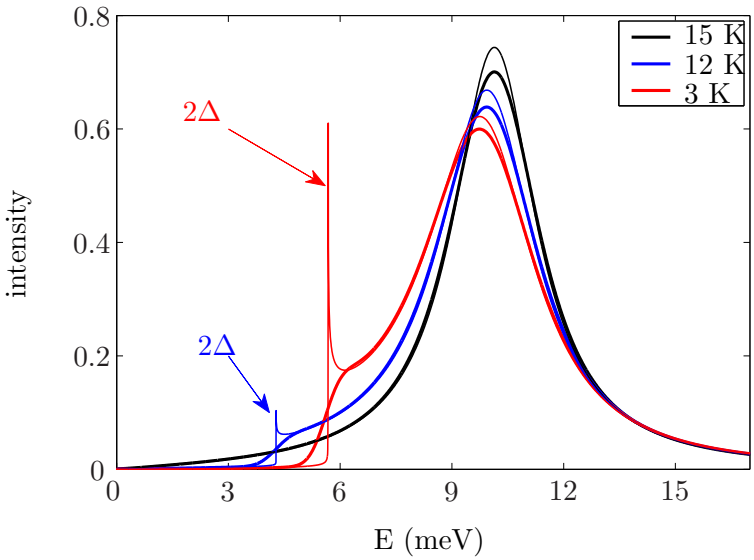

(b) Theory

Figure 3.16: (a) Phonon scans at $\mathbf{Q} = (0.5,\ 0.5,\ 7)$ for $T \leq T_c$. Lines are guides to the eye for $T < T_c$ and a theoretical fit with a lorentzian for $T = T_c$ (15 K). An estimate of the experimental background was subtracted. (b) Calculated phonon spectral function (for details see text). The curve at $T =$ 15 K is fitted to the experimental data (see (a)) as explained in sec. 3.3.3. The theoretical results (thin lines) are convoluted with the experimental resolution (thick lines).

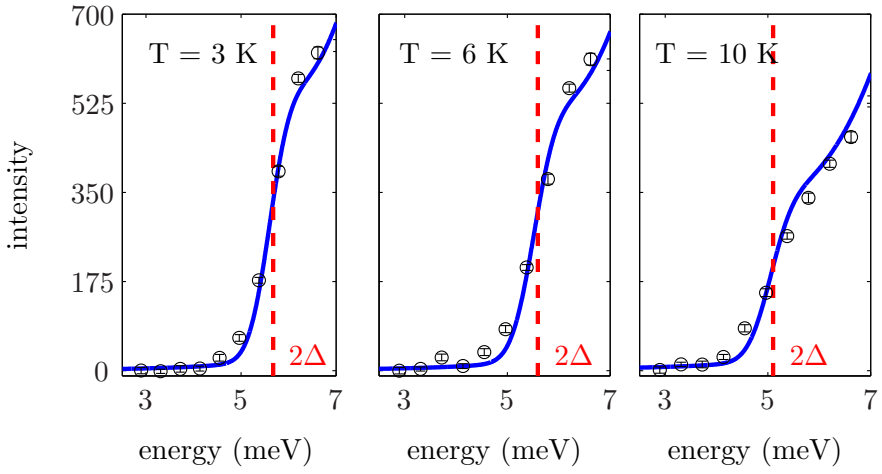

Figure 3.17: Energy scans at $\mathbf{Q} = (0.5, 0.5, 7)$ for three different temperatures. Blue lines are calculated phonon spectra. Compared to the 15 K data, the calculations are scaled by a factor of 1.35, in order to show the qualitative agreement with theory and the precision of the gap (red dashed line) determination.

3.3.5 Re-investigation of the phonon anomaly at q = (0.5, 0, 0)

The method of extracting the superconducting gap from phonon lineshapes explained above looks straightforward. Therefore, one might ask why it has not yet been used so far. There are indeed two stringent conditions which have to be met to make the signature of the superconducting gap clearly visible: (i) the linewidth in the normal state has to be relatively large, i.e. about 10 % of the phonon frequency or even more and (ii), the phonon energy should be not much larger than twice the gap energy, otherwise the tail of the phonon line extending into the gap region will be too weak.
One might also think to study phonons with an energy comparable to the gap energy. Here, the superconductivity-induced changes of the phonon lineshape are fairly strong, but extraction of the gap energy can only be made with the help of detailed calculations (see fig. 3.15 (b), (f)). An example for such a case is the TA phonon in the (100) direction at wavevector $\mathbf{q} = (0.5, 0, 0)$. As discussed in sect. 3.3.2, profound changes of the lineshape of this phonon were first observed by Kawano et al. [24]. Puzzled by the appearance of an intense and relatively narrow line below T_c Kawano et al. thought to have found a new sharp excitation.
The temperature dependence of this phonon was re-investigated by Kreyssig[6] and Stockert[7] by measurements on the TAS 1T at LLB, Saclay. However, they never evaluated their data and finally asked me to do it along the same lines as used for the M-point

[6]Institute of solid state physics, Technical University Dresden
[7]Max-Planck Institute for chemical physics of solids, Dresden

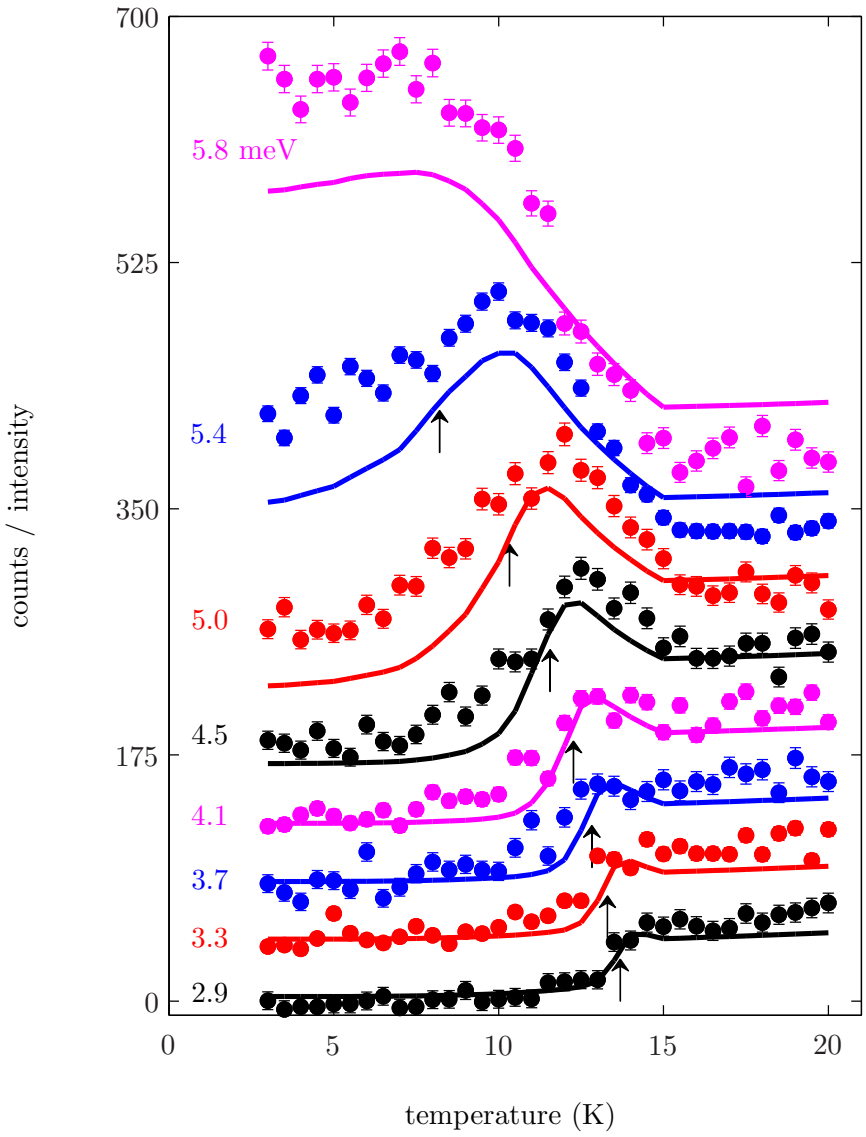

Figure 3.18: Temperature scans at $\mathbf{Q} = (0.5, 0.5, 7)$ at various energy transfers in the range of 2.9 meV $<$ E $<$ 5.8 meV (see values on the left side of the data). Lines are calculated within the framework of the theory proposed by Allen et al. [53]. Arrows indicate the temperature at which $2\Delta(T)$ is equal to the energy transfer.

phonon. I will show that the peculiar lineshapes appearing below T_c can be quite naturally understood using again the theory of Allen et al. [53].

The phonon at q = (0.5, 0, 0) has a significantly lower energy than the M-point phonon discussed above (7 meV as compared to 10 meV) and moreover, has a much larger linewidth. As a consequence, the superconductivity-induced re-distribution of spectral weight is even stronger, but the superconducting gap cannot be inferred from the data as easily, except for temperatures close to T_c where the gap is still small. For lower temperatures, most of the spectral weight condenses into a fairly sharp peak whose energy is somewhat below the gap. As mentioned above, this resonance can be regarded as a mixed vibrational/superelectronic collective excitation. Its position with respect to 2Δ has to be determined from calculations for the parameter values of this particular phonon. Again, the theory does not reproduce the observed lineshapes quantitatively, but sufficiently well to allow for a precise determination of the gap value (fig. 3.19). For temperatures near T_c, temperature scans were used to determine $2\Delta(T)$ similar to the case of the M-point phonon (fig. 3.20).

Plotting 2Δ versus temperature extracted from the two phonon lines discussed above, the two data sets differ considerably (fig. 3.21). In other words, the data show evidence of two gaps with different absolute values at zero temperature, $2\Delta(0)_{(0.5,0,0)} = 4.08 \pm 0.1\,\mathrm{meV}$ and $2\Delta(0)_{(0.5,0.5,0)} = 5.7 \pm 0.1\,\mathrm{meV}$ probed by the different phonons. This fact can be inferred rather directly from the raw data when comparing the temperature evolution of the intensities at different energy transfers as is demonstrated in fig. 3.22 for three energy values. The temperature evolution of the intensities at $\mathbf{Q}$ = (0.5, 0, 8) (open symbols) and at (0.5, 0.5, 7) (filled symbols) is quite similar but only if one compares energies according to $\frac{E_{(0.5,0.5,7)}}{E_{(0.5,0,8)}} = 1.5$. Thus, a rough estimation of the gap difference, $\approx 50\%$, can be extracted directly from the raw data without any calculations.

The nearly perfect agreement of the different temperature scans after scaling the energies by a factor of 1.5 is even more remarkable considering that the data were taken on different TASs, namely *1T* at LLB for $\mathbf{Q}$ = (0.5, 0, 8), and *PUMA* at the research reactor in Munich for $\mathbf{Q}$ = (0.5, 0.5, 7).

Different energy gaps might arise from two-band superconductivity as in the case of MgB_2 [57] and proposed for YNi_2B_2C as well [58], or from gap anisotropy or from both. For both scenarios the question arises how phonons can probe different energy gaps rather than an average one. We presume that this is due to the fact that for the phonons under investigation, most of the coupling to the quasi-particles stems from a rather narrow region of the Fermi surface, and hence it is the gap opening up at this particular section of the Fermi surface which is reflected in the phonon lineshape.

As it is now evident that the superconducting energy gap in YNi_2B_2C exhibits a clearly non-isotropic behaviour, it is rather surprising that the experimental data are quite well described by Allen's theory which assumes an isotropic gap. As we will see in the next section, the experimental gap values determined from phonon scans vary continuously from 4 meV to even above 6 meV (inset of fig. 3.21). Nonetheless, the superconductivity induced features are quite sharp, mostly resolution limited.

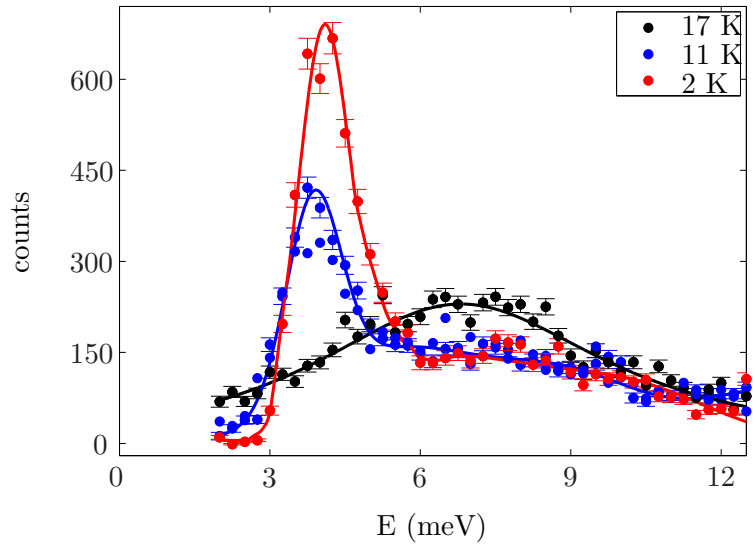

(a) Experiment

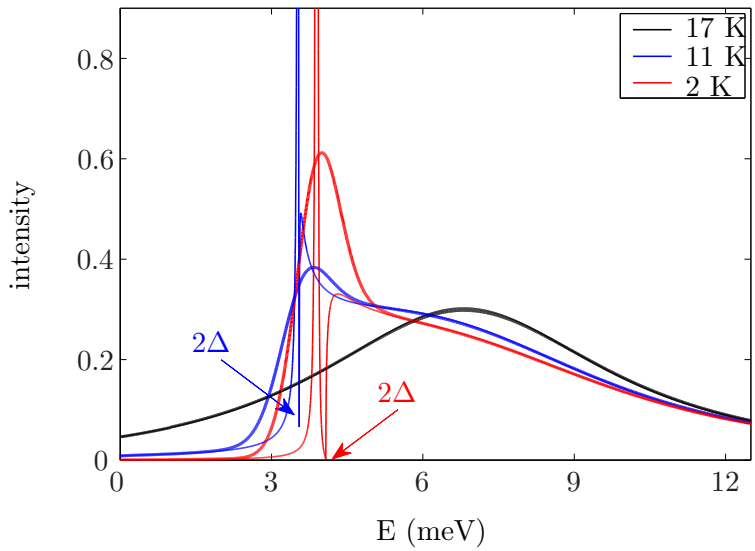

(b) Theory

Figure 3.19: (a) Phonon scans at $\mathbf{Q} = (0.5, 0, 8)$ for temperatures just above and below T_c. Lines are guides to the eyes for $T < T_c$ and a fit with a lorentzian for $T = 17\,\mathrm{K}$. An estimate of the experimental background was subtracted. (b) Calculated phonon spectral function (for details see text). The lineshape of the curve at $T = 17\,\mathrm{K}$ is fitted to the experimental data (see (a)) as explained in sec. 3.3.3. The theoretical results (thin lines) are convoluted with the experimental resolution (thick lines).

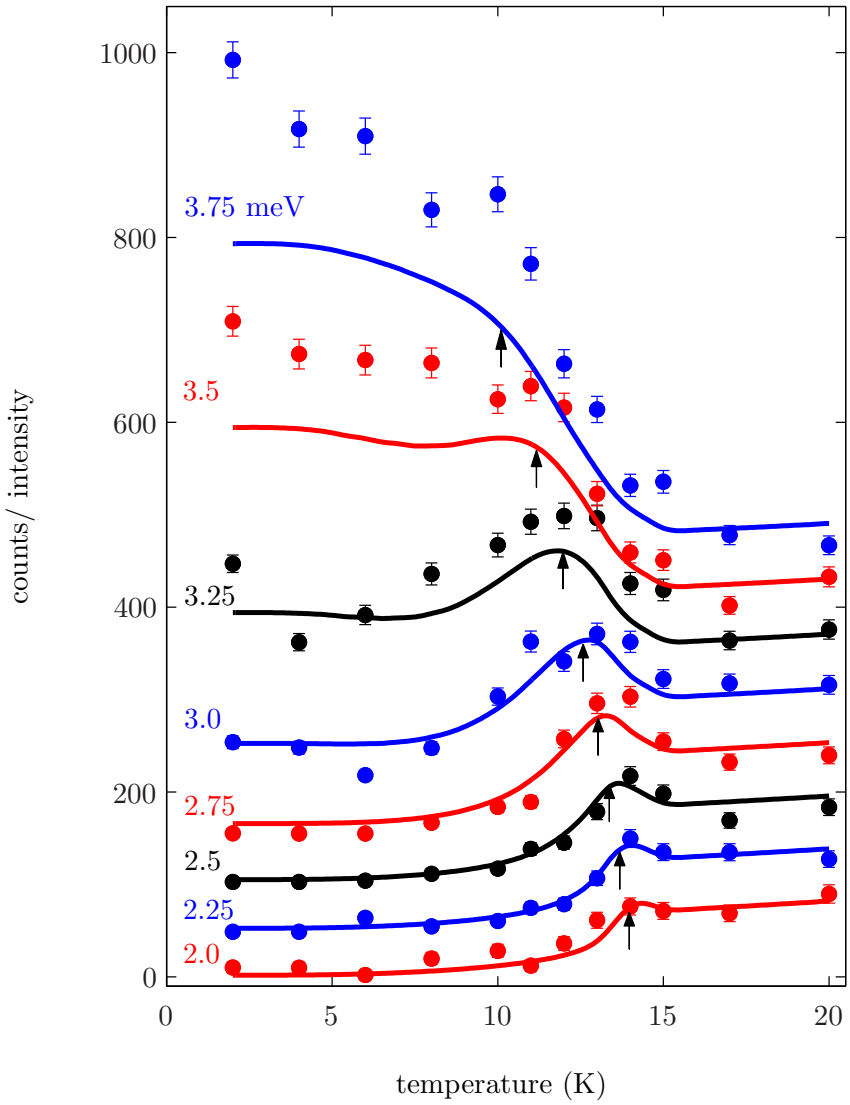

Figure 3.20: Temperature scans for energies 2.0 meV $<$ E $<$ 3.75 meV (see numbers on the left side of curves) for $\mathbf{Q}$ = (0.5, 0, 8). Lines are calculated within the framework of Allen's theory [53]. Arrows indicate the temperature at which the energy transfer is equal to $2\Delta(T)$.

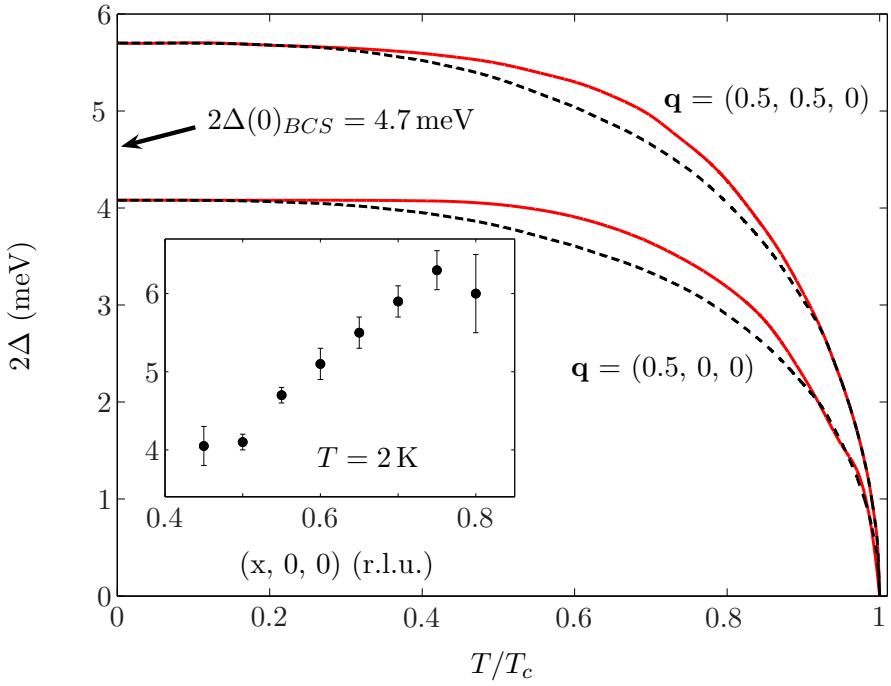

Figure 3.21: Temperature dependence of the superconducting energy gap 2Δ as extracted from experiment for two different phonons (red lines). Black lines describe BCS weak coupling behavior, scaled to the measured low-temperature values. The insert describes the evolution of the gap extracted from phonons in the (100) direction at $T = 2\,\mathrm{K}$ (see sec. 3.3.6).

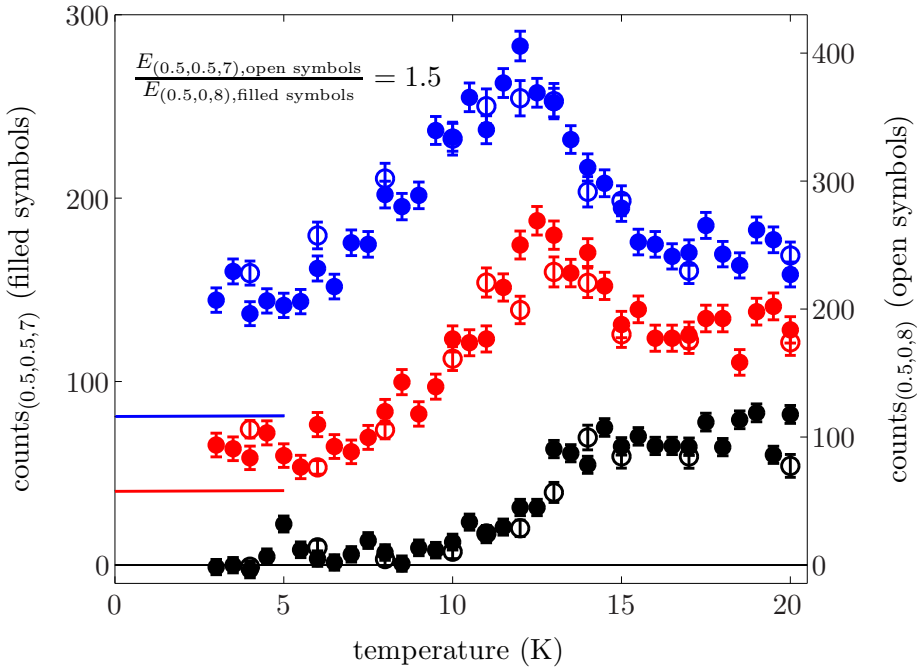

Figure 3.22: Comparison of temperature scans at $\mathbf{Q}$ = (0.5, 0.5, 7) (filled symbols) and (0.5, 0, 8) (open symbols). Same colors denote scans with $\frac{E_{(0.5,0.5,7)}}{E_{(0.5,0,8)}} = 1.5$. The absolute values of the energies at $\mathbf{Q}$ = (0.5, 0.5, 7) and (0.5, 0, 8) are 3.3 meV (black), 4.5 meV (red), 5.0 meV (blue) and 2.25 meV (black), 3.0 meV (red), 3.25 meV (blue), respectively. Color coded horizontal lines denote the zero of the corresponding data sets.

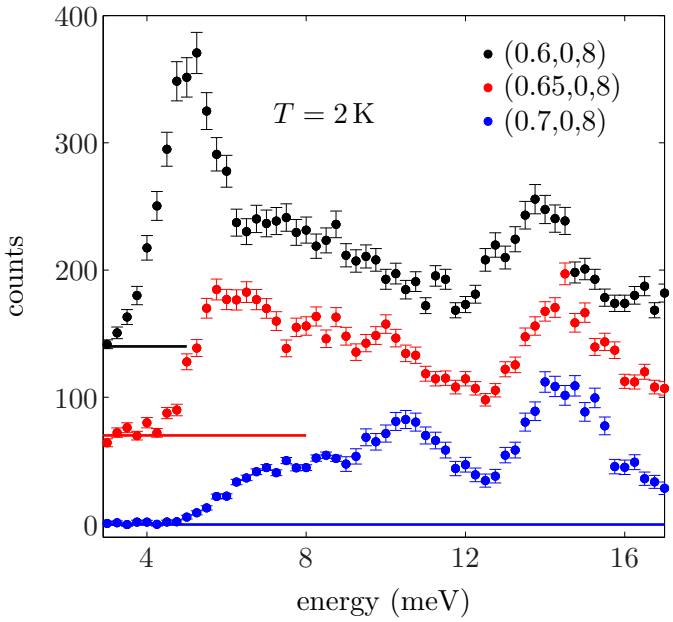

Figure 3.23: Energy scans at $T = 2\,\mathrm{K}$ for $\mathbf{Q}$ = (0.6 - 0.7, 0, 8). An offset (color-coded horizontal lines) was included for the sake of clarity.

3.3.6 Evolution of the superconducting gap extracted from phonons along the (100) direction

In addition to the superconductivity induced changes of the phonon lineshape at the M-point and at $\mathbf{q}$ = (0.5, 0, 0), similar changes were observed at neighbouring wave vectors. Although the superconductivity induced signatures become weaker when going away from $\mathbf{q}$ = (0.5, 0, 0) we made an investigation of these features along the (100) direction in order to determine the evolution of the superconducting energy gap extracted from phonons over a large part of the Brillouin zone. The requirements concerning the phonon frequency, linewidth and the gap value discussed above limit the range in reciprocal space where superconductivity induced changes can be observed. For smaller wave vectors than $\mathbf{q}$ = (0.5, 0, 0), the frequencies rapidly increase and the phonons loose coupling strength. Therefore, we only evaluated one additional $\mathbf{q}$ point in this direction, i.e. $\mathbf{q}$ = (0.45, 0, 0). Towards the zone boundary, the frequnecies also increase but much slower. Further, the coupling strength decreases much less and is rather transferred to the first optic branch. Thus we were able to observe superconductivity induced effects up to $\mathbf{q}$ = (0.8, 0, 0).

Fig. 3.23 shows energy scans at $T = 2\,\mathrm{K}$ for $\mathbf{Q}$ = (0.6 - 0.7, 0, 8). The phonon lineshape at $\mathbf{Q}$ = (0.6, 0, 8) is similar to that at $\mathbf{Q}$ = (0.5, 0, 8), although the relative intensity of the sharp peak at the low energy side of the phonon is somewhat reduced. This can be understood as the result of a decreasing strength of the superconductivity induced

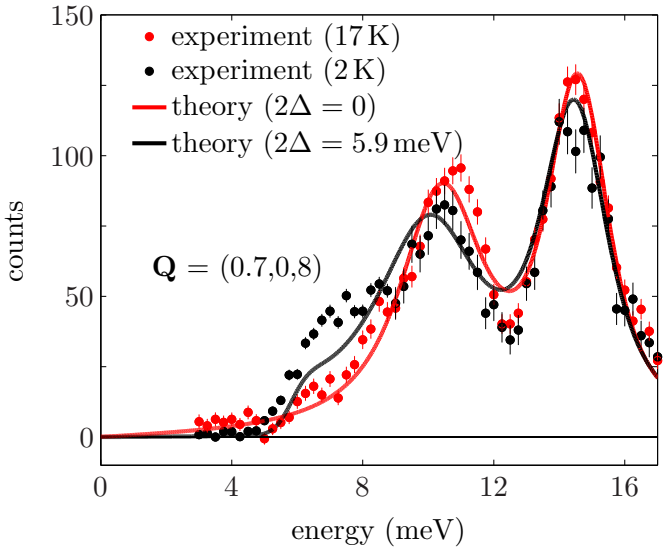

(a) $\mathbf{Q}$ = (0.7, 0, 8)

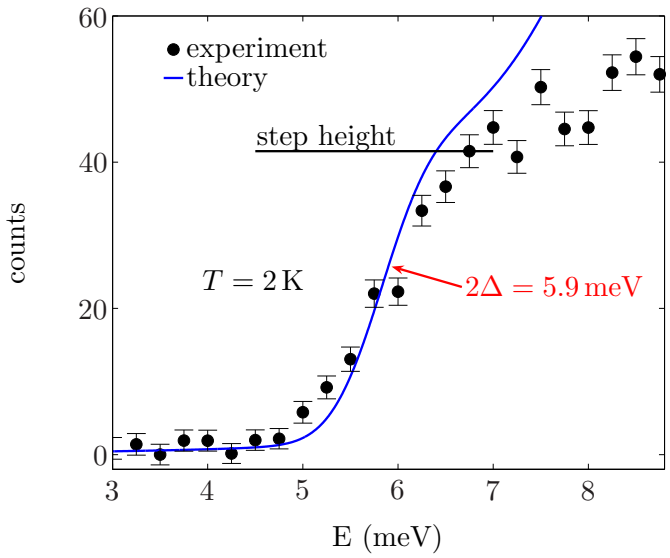

(b) Determination of 2Δ

Figure 3.24: (a) Energy scans observed at $\mathbf{Q}$ = (0.7, 0, 8) for $T < T_c$ (black dots) and $T > T_c$ (red dots). Lines are calculated within Allen's theory [53] for the normal (red) and the superconducting state (black), wherein both phonons were treated as being not coupled to each other (see text). The experimental background was subtracted. (b) Enlargement of the low energy region of the low temperature scan in (a). The blue line was calculated assuming a gap of $2\Delta = 5.9\,\text{meV}$ (black line in (a)). The theoretical result was scaled by a factor of 1.8 in order to reproduce the observed step height (horizontal line) and thus enabling us to extract 2Δ.

effect due to an increased phonon frequency of 8 meV compared to 7 meV at $\mathbf{q}$ = (0.5, 0, 0). Concomitantly, the coupling strength, i.e. the intrinsic linewidth of the phonon, is reduced (see fig. 3.7 (a)). On going to larger $\mathbf{q}$ values in the (100) direction, the phonon branch is further dispersing upwards and therefore the effect weakens even more. At $\mathbf{Q}$ = (0.7, 0, 8) we observed a phonon lineshape in the superconducting state similar to that of the low temperature one for the M-point phonon shown in fig. 3.16 (a). This qualitative change of the low temperature lineshape for wave vectors in close neighbourhood to each other supports the view that the superconductivity induced changes of the phonon lineshapes at both, $\mathbf{q}$ = (0.5, 0, 0) and (0.5, 0.5, 0), originate from the same underlying physical mechanism. We note that the turning point between the two lineshapes occurs at $\mathbf{q}$ = (0.65, 0, 0). Thus $\mathbf{q}$ = (0.65, 0, 0) corresponds to case 3 of Allen's theory shown in fig. 3.15 (c) and (g).
The energy scans observed at $\mathbf{Q}$ = (0.7, 0, 8) for T = 17 K and 2 K are shown in fig. 3.24 (a). Lines are once more the results of Allen's theory for the normal and the superconducting state, respectively. However, the experimental data clearly show that both the acoustic and the optic phonon peaks are affected by superconductivity. Therefore, we fitted two Lorentzians to the normal state data and then calculated the effect of a superconducting gap for each phonon separately. This approach to treat the two phonons of the same symmetry as being uncoupled is clearly an approximation, but reproduces the observed lineshape rather well. Not surprisingly, the theory underestimates the experimentally observed re-distribution of spectral weight in a similar manner as for the previously analysed phonons.
Fig. 3.24 (b) shows an enlargement of the low energy region of the T = 2 K energy scan in panel (a). The blue line represents an upscaled version of the theoretical curve shown in (a) in order to reproduce the observed step height, which is indicated by the horizontal line. The scaling factor was adjusted as to place the bulge on the upper side of the step-like feature in the calculation to the same height as experimentally observed. An equivalent plot for the M-point phonon was already shown in fig. 3.17. What is different here is the fact that the observed width in energy of the intensity-step is larger than the calculated one, whereas there is good agreement in this respect at the M-point. This indicates that the phonon at $\mathbf{q}$ = (0.7, 0, 0) probes a relatively large region of the Fermi surface with a considerable variation of the gap energy. The gap value was determined in a way that the calculated curve crosses the observed intensities at half of the step height. Thus 2Δ = 5.9 meV is somehow an average gap value (see also discussion below). For the other wave vectors a similar procedure was used.
In fig. 3.25 the difference data of the observed intensities at T = 2 K and T = 17 K, I_{2K-17K}, are plotted for $\mathbf{Q}$ = (0.7 - 0.8, 0, 8) (black dots). Red lines denote the calculated intensities for the superconducting minus that for the normal state. The extracted gap values are displayed for each wave vector and the values for r_Q, which determine the strength of the sueprconductivity induced effects (see sect. 3.3.3), are given for the TA and TO phonons. They were determined by fitting of the normal state intensities. The difference data of the M-point phonon are plotted as well for the sake of comparison (inset of fig. 3.25).
For $\mathbf{q}$ = (0.7 - 0.8, 0, 8) the data clearly show that both the TA and TO phonons

are affected by superconductivity. The principal features observed in experiment are all reproduced by theory (red line). Nonetheless, inspection of the figures reveal several shortcomings of the theory. This is, of course, not really surprising since similar shortcomings were already found for the simpler cases where only one phonon had to be considered. It is rather surprising that the theory still gives a rather satisfactory description of the observed effects although it was not designed to deal with such a complicated situation. In this context, we would like to discuss an already mentioned discrepancy between theory and experiment in more detail: the intensity increase at $E = 2\Delta$, which is found to be more gradual than calculated. This might be well due to the fact, that on moving away from $\mathbf{q} = (0.5, 0, 0)$ the phonon does no longer get its coupling from a narrow section of the Fermi surface due to the Fermi surface nesting. Thus, the phonon integrates over different parts of the Fermi surface having different energy gap values.

As the superconductivity induced effects on the phonon lineshapes for $\mathbf{q} > (0.7, 0, 0)$ become very weak we plotted only the difference data for these wave vectors (fig. 3.25). The observed maxima in I_{2K-17K} for $\mathbf{Q} = (0.75, 0, 8)$ and $(0.8, 0, 8)$ are a factor of 3 and 6 smaller than for $\mathbf{Q} = (0.7, 0, 8)$, respectively, but the general features remain the same. For the latter, $\mathbf{Q} = (0.8, 0, 8)$, we found that the upper peak, corresponding to the TO phonon, is affected much stronger by superconductivity than the TA phonon peak. Having a closer look on how strong the two TA and TO phonon peak intensities are affected by superconductivity, we see a continuous evolution between $\mathbf{Q} = (0.6, 0, 8)$ and $(0.8, 0, 8)$. First, only the TA phonon is altered (equivalent to the case at $\mathbf{q} = (0.5, 0, 0)$), while at the latter wave vector it is predominantly the TO phonon. In between, both phonon peaks show similar reductions of the peak intensities in the superconducting state. This behavior can be qualitatively understood in terms of an exchange of eigenvectors, especially for the displacements of the B and C atoms as was discussed for the DFT results in sect. 3.2.2: According to DFT, the strength of the electron-phonon coupling for the low energy phonons in YNi_2B_2C is coupled to large amplitudes of the light B and C atoms in the polarization patterns. In Allen's theory the strength of the superconductivity induced effects, e.g. the value of r_Q, is roportional to the intrinsic phonon linewidth caused by strong electron-phonon coupling. Thus, the here observed transfer of the relative strength of the superconductivity induced effect from the TA to the TO phonon can be related to a corresponding change in the phonon eigenvectors. And indeed, the maxima of the absolute values of the atomic displacements of B and C in the TA and TO phonon branch in the (100) direction (fig. 3.4 (a)) coincide well with the observed wave vector dependent strength of the superconductivity induced effects shown in figs. 3.24 and 3.25. That means, around $\mathbf{q} = (0.5, 0, 0)$, where only the TA phonon was affected, there are large amplitudes for B and C in the acoustic branch but very small ones in the optic branch. The B and C elongations then reach a maximum in the TO branch at $\mathbf{q} = (0.75$ - $0.8, 0, 0)$ whereas the C and B amplitudes are reduced by a factor of 5 and 2, respectively, in the TA branch at $\mathbf{q} = (0.75, 0, 0)$.
When looking in detail on the $\mathbf{Q} = (0.8, 0, 8)$ data, one can see a finestructure around 6 meV which might be the signature of two distinct gaps. An attempt to evaluate the data with two different gap values for the TA and the TO phonon, respectively, leads to gap values of $2\Delta = 5.5$ meV and nearly 7 meV, what would be extremely large compared

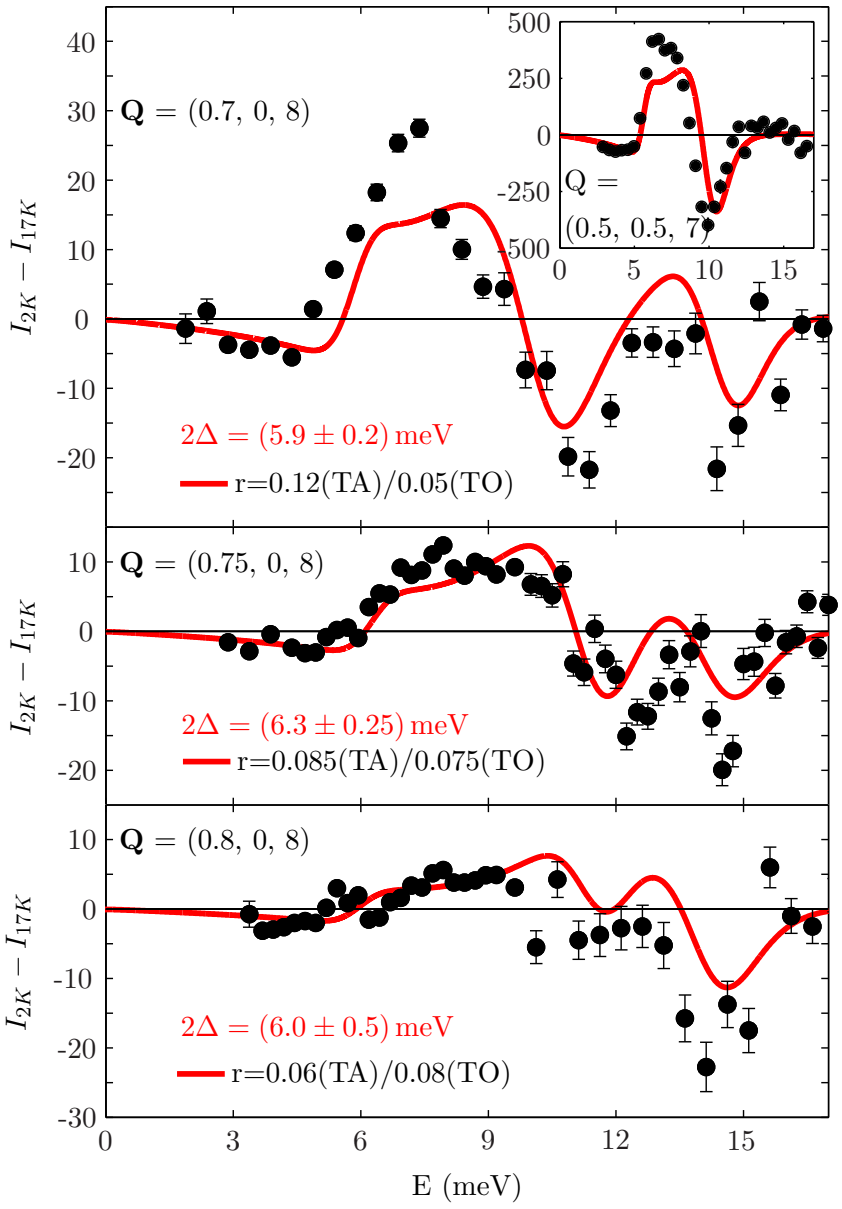

Figure 3.25: Plots of difference data for **Q** = (0.7 - 0.8, 0, 8). The r_Q values used in the calculation are given in each panel. The insets shows a similar plot for the M-point phonon for comparison.

to the canonical BCS value of $2\Delta_{BCS} = 4.7\,\text{meV}$. We note that the calculated red line referes to a single gap value of 6 meV.
The results for 2Δ are summarized in the insert of fig. 3.21. The gap varies smoothly from 4.1 meV at $\mathbf{q} = (0.5, 0, 0)$ up to 6.3 meV at $\mathbf{q} = (0.75, 0, 0)$. Further on, it seems to decrease again, but the error bar is quite large for this result, as discussed above. We note that we found no evidence for a further decrease of the gap value at $\mathbf{q} = (0.45, 0, 0)$. Here, the gap is the same as for $\mathbf{q} = (0.5, 0, 0)$ within the error bars. We emphasize, that according to the results presented in this section, the energy gap value determined for the M-point phonon, $2\Delta_{M-point} = 5.7\,\text{meV}$, is not an extremum, but lies within the range of the observed gap values for the (100) phonons.

3.3.7 Concluding remarks

Allen et al. [53] reported an upper boundary for the phonon frequency with respect to 2Δ, for which superconductivity induced changes of the phonon lineshape should be observeable, as $\hbar\omega_N \leq (1 + 2r)2\Delta$. According to this prediction, an altered lineshape should only be observed for phonons with a frequency $\hbar\omega_{phonon} \leq 8.3\,\text{meV}$, when using the parameters extracted from the experimental data at $\mathbf{Q} = (0.75, 0, 8)$. However, the frequencies of the TA and TO phonons at this wave vector are $\omega_N = 11.8\,\text{meV}$ and $\omega_N = 14.7\,\text{meV}$, respectively. Thus, superconductivity induced changes of the phonon lineshape are observable in a much larger frequency range than assumed in ref. [53]
Therefore, we think that these superconcuctivity induced features could be observed also in other phonon-mediated superconductors with less extreme electron-phonon coupling strength. However, one has to know what to look for, especially if the features are as small as for $\mathbf{Q} = (0.75, 0, 8)$. It also means that one has to use unusual long counting times for low energy phonons, in our case $\approx 4-5$ min. per point, in order to identify the influence of superconductivity on the phonon lineshape.

3.4 Discussion

3.4.1 Symmetry of the superconducting energy gap in YNi_2B_2C

An important issue in the discussion of superconductivity in borocarbides is the symmetry and the size of the superconducting energy gap. Gap anisotropy has been inferred from a variety of experimental techniques. Most of the work on the symmetry of the superconducting energy gap was done by magnetic field dependent specific heat measurements [59, 60] (also field-angle dependent [61]), thermal conductivity [62], de Haas-van Alphen measurements (dHvA) [63] and, more recently, low-temperature scanning-tunneling microscopy (STM) and spectroscopy (STS) [64]. All investigators conclude that they see signatures of small-gap regions on the Fermi surface (FS) or even nodal points or lines. These nodes are typically inferred from the observation of quasiparticle

excitations at energies much lower than the gap maximum Δ_0. In the following a short list of the experimental observations will be given.

- Magnetic field dependent measurements revealed a $\sqrt{H}$-dependence of the low-temperature electronic specific heat coefficient $\gamma(H)$ in $LuNi_2B_2C$ [59] and YNi_2B_2C [60] unexpected for isotropic s-wave supercondcutors. For an isotropic gap, the quasiparticle excitations would be confined to the vortices and thus the electronic specific heat would increase linearly with the number of vortices in the sample, e.g. the applied magnetic field.

- de Haas-van Alphen oscillations coming from a small electron pocket in the boro-carbide superconductor YNi_2B_2C ($H_{c2} = 10\,\mathrm{T}$ [58]) have been observed in the vortex state down to a surprisingly low field of 2 T. The observed amplitude at low fields is much larger than given by theoretical predictions [65, 66] based on a BCS value of the superconducting gap [67]. The authors argue that the gap on this particular part of the FS is much smaller than the gap on other parts of the FS [63].

- The field dependence of the electronic thermal conductivity of $LuNi_2B_2C$ is very similar to that of UPt_3 (roughly linear in T), a heavy-fermion superconductor with nodal lines in the gap, and very different from the exponential dependence characteristic of s-wave superconductors [62].

- Angular variations for the field-angle dependent heat capacity were analyzed as a function of magnetic field angle, field-intensity, and temperature to provide its origin. From the quantitative agreement between experiment and theory [68] the authors concluded that one is directly observing nodal quasiparticles generated along (100) by the Doppler effect [61].

- Shulga et al. measured the temperature dependencies of the upper critical fields in $LuNi_2B_2C$ and YNi_2B_2C and compared them to model predictions [58]. The authors concluded that the experimental observations can be well described in an effective two-band model.

- STM and STS measurements at $T = 0.46\,\mathrm{K}$ showed evidence of a fourfold-symmetric star-shaped vortex core. This was interpreted as signature of small parts of the FS with a minimal gap along (100) and a larger one along (110).

- Bashlakov et al. reported point-contact spectroscopy measurements on YNi_2B_2C [69]. The extracted values of 2Δ for a non-oriented sample range from 2.6 meV to 6.6 meV. However, the lowest and largest values are separated by $\Delta E = 0.6\,\mathrm{meV}$ from a broad energy region, where most of the observed energy gaps are located. Gap values extracted from measurements along the (100), (001) and (110) directions were reported as 3 meV, 4.6 meV and 5.0 meV, respectively.

Here, we want to point out that an assignment of a single gap value to a certain direction, i.e. a direction dependent energy gap, is not meaningful for superconductors with

a complicated FS topology like YNi_2B_2C.
In the general case of an anisotropic energy gap the gap values will vary on the FS in a way, which in general cannot be described by any simple function like the ones invented ad-hoc in the literature. Moreover, the FS of YNi_2B_2C, like that of many other compounds, is composed of several pockets, each having their own gap function. If in such a case the gaps on different parts of the FS (belonging to different bands) are widely different, but relatively isotropic on each part, one speaks of two-band (or multi-band) superconductivity. A nice example of such a case is MgB_2. In general, however, the gaps may already vary on each part of the FS considerably leading to a continuous distribution of gaps. Theory can in principle predict the full variation of gaps over all parts of the FS but in reality, the computational effort would be enormous. Therefore, there is little hope that such a calculation will be performed for YNi_2B_2C in the near future [70]. We note that in measurements of macroscopic quantities like upper critical field or thermal conductivity, they will reflect integrals over the whole FS. Their behavior might well be explained by a gap function having a simple functional form, but this function should not be confused with the full variation of the gap on all the parts of the FS
The gap probed by phonons will reflect the local gap of a particular part of the FS if this phonon gets the dominant contribution to its coupling strength to the quasiparticles from just that part. Which part of the FS gives the coupling cannot be inferred from the phonon measurements, but needs to be answered by DFT. Inspection of the FS might already give the answer, but on the other hand, a specific phonon with wave vector $\mathbf{q}$ will, in general, connect more than a single pair of points of the FS. This is even more true for such a complicated FS as in YNi_2B_2C, in which the FS stems from three bands. We note that the parts of the FS, connected by $\mathbf{q}$, may even have very different gap values. Thus, several gap values can correspond to a single phonon wave vector. Luckily enough, we found several phonons in YNi_2B_2C, which apparently probe regions of the FS with a quite small variation of the gap.
At $\mathbf{q}$ = (0.5, 0, 0) it seems relatively clear that pronounced Fermi surfuce nesting is responsible for probing just this part of the FS. In contrast, it is much less clear which parts of the FS are probed by the M-point phonon. We note that there are many small pockets on the FS, which are connected by $\mathbf{q}$ = (0.5, 0.5, 0) [70]. Thus, it is rather surprising that we observe a so well defined signature of the superconducting gap in our phonon measurements for this phonon. In the case when many sets of points on the FS are connected by the same wavevector and all sets are equally responsible for the electron-phonon coupling effects, one would expect a broad gap signature, centered around an average value. This behavior seems to be true for $\mathbf{q}$ = (0.7 - 0.8, 0, 0) (see sect. 3.3.6).
From what was said above, our method of determining 2Δ is restricted to distinguished parts of the FS and therefore, we cannot claim to measure the maximum gap anisotropy. Our data are in agreement with the above cited papers as to the fact that the gap is anisotropic. There is also good agreement between gap values deduced from point contact spectroscopy [69] and our results. However, we cannot rule out on the basis of our measurements that there are regions of the FS having a very small gap as advocated by some of the papers cited above. There might well be no phonon suitable for probing this part of the FS.

3.4.2 Superconducting pairing mechanism

The most important question in superconductivity is the pairing mechanism responsible for Cooper pair formation. In conventional superconductors, the pairing is phonon mediated, whereas the determination of the coupling mechanism in exotic superconductors, like high T_c's and heavy fermions, is still the goal of many theoretical and experimental investigations.
In most of the above cited papers, the authors advocate an anisotropy of the gap, $\Delta_{max}/\Delta_{min} \approx 10$ or even larger, so far unseen for classical phonon-mediated superconductors. This has led to question the nature of the pairing mechanism itself, in analogy with high-T_c and heavy Fermion superconductors.
The prediction of a high $T_c = 12.6\,\mathrm{K}$ by DFT assuming a phonon mechanism in conjunction with the experimental verification of the predicted electron-phonon coupling strength by our measurements provide conclusive evidence that despite all the above described anomalies in various physical measurements, the pairing mechanism is still conventional.

3.5 Further investigations

Due to time limitations several projects had to be scheduled after the completion of this thesis.

- A proposal for 7 days of beam-time on the cold *TAS* 4F-2, LLB, was recently accepted. In the proposed study, we want to investigate the phonon lineshape under a magnetic field smaller than the upper critical field of $H_{c2} \approx 10\,\mathrm{T}$ [58]. Since YNi_2B_2C is a type-II superconductor, such a state is characterized by the presence of magnetic vortices, in the core of which superconductivity is completely suppressed. Outside the vortex core, however, the superconducting gap gradually recovers and finally reaches its full original value, provided the density of vortices is not too high, i.e. the magnetic field is not too close to H_{c2} . The aim of the proposed experiment is to find out whether or not the phonon lineshape will reflect the inhomogeneous nature of the superconducting state. In other words, we would like to find out whether phonons act as a local probe or are rather averaging the superconducting properties over a length scale much larger than the vortex dimensions. The phonon best suited for such a study is the M-point phonon with energy $E = 10\,\mathrm{meV}$ discussed above.

- The eigenvector predicted by DFT for the TA phonon at $\mathbf{q} = (0.5, 0, 0)$ will be checked by measuring the integrated intensities in different Brillouin zones.

- Another open issue is the electron-phonon coupling strength of the B-A_{1g} phonon at $E = 103\,\mathrm{meV}$. This mode strongly renormalises the bonding angle of the Ni-B

tetrahedra and was proposed to play a key-role in the superconducting pairing mechanism [35]. DFT predicts an extreme coupling strength of this phonon with a linewidth of $2\Gamma_{epc} = 24\,\mathrm{meV}$, but only at the zone center. The calculated linewidth decreases rapidly going out into the Brillouin zone and the contribution of this particular mode to the electron-phonon coupling constant λ therefore is calculated to be only 4%. The Raman results for this phonon [36–38] are no unambiguous confirmation of the predicted huge intrinsic phonon linewidth ($2\Gamma = 24\,\mathrm{meV}$), because the observed large linewidth of the B-A_{1g} occur in both superconducting YNi_2B_2C and in the non-superconducting reference compound $Y(Ni_{0.7}Co_{0.3})_2B_2C$. So far, experimental investigations using inelastic neutron scattering were unsuccessful due to unfavorable experimental constraints.

- First results for $\mathbf{Q} = (0.9,\ 0,\ 8)$ at $T = 2\,\mathrm{K}$ and $17\,\mathrm{K}$ indicate an appearance of superconductivity induced effect towards the zone boundary, although no altered phonon lineshape at $\mathbf{Q} = (0.85,\ 0,\ 8)$ was observed. Therefore, further measurements will be made for phonons close to the zone boundary.

4 Colossal magnetoresistance - competition between magnetism and polaron formation in manganites

4.1 Introduction

Transition-metal oxides (TMO) have been the subject of study over a long time already, because they exhibit a wide range of interesting physical phenomena, which are still poorly understood. Most importantly, strong electron-electron and electron-lattice correlations have to be taken into account. TMO attracted particular attention after the discovery of high-temperature superconductivity (HTSC) in 1986 [71].
Somewhat later, the observation of extremely large magnetoresistance (named *colossal magnetoresistance (CMR)*) in manganites by Helmholt et al. [72] and Jin et al. [73] sparked special interest in the long known family of manganese perovskites. There was hope for applications of the rare-earth manganites, for example as magnetoresistive sensors [74].
But the manganites are also interesting for basic condensed-matter physics for a different reason. These materials offer a unique opportunity to study the interplay of spin, charge and orbital degrees of freedom. In particular, the metal-insulator transition in manganites is caused by a competition between localization of electronic states and electronic band formation. The onset of long-range ferromagnetic order and a concomitant drop of the electrical resistivity was first explained by the double-exchange picture (see sect.4.1.3) [75–78], in which the ferromagnetic alignment of all $3d$ spins of the Mn ions strongly increases the degree to which the e_g electrons are delocalized. On the other hand, it is not only the breakdown of the ferromagnetism above the Curie temperature T_C, which causes the enhanced electrical resistivilty, but also a self-trapping mechanism via polaron formation, which strongly suppresses the intersite hopping rate of the conduction electrons [79, 80].
The investigations during this work concentrate on ferromagnetic CMR manganites, i.e. $La_{0.7}Sr_{0.3}MnO_3$ and $La_{1.24}Sr_{1.76}Mn_2O_7$. Results will be compared with the prototype CMR compound $La_{1-x}Ca_xMnO_3$, $x = 0.25, 0.35$. Elastic and inelastic neutron scattering techniques were used to gain more insight into the physical mechanisms of the ferromagnetic(FM)-to-paramagnetic(PM) metal-insulator (MI) transition and the nature of the FM groundstate.

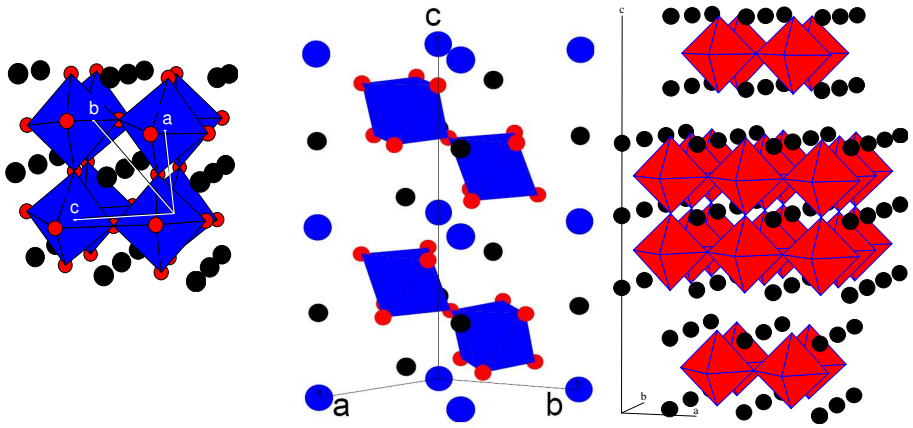

(a) $La_{1-x}Sr_xMnO_3$ (b) $La_{1-x}Sr_xMnO_3$ (c) $La_{1.24}Sr_{1.76}Mn_2O_7$

Figure 4.1: Crystal structures of $La_{1-x}Sr_xMnO_3$ ($x = 0.3$) with (a) rhombohedral and (b) hexagonal bases and (c) tetragonal $La_{2-2x}Sr_{1+2x}Mn_2O_7$. MnO_6 octahedra are shaded with Mn ions in the center and oxygen (red) at the corners. Only full octahedra are colored. Black dots represent La/Sr sites.

4.1.1 Structure and phase diagram

The cubic perovskite is the parent structure of the $(R,A)_{n+1}M_nO_{3n+1}$ compounds, where R, A and M are trivalent rare-earth, divalent alkaline-earth and transition-metal ions, respectively, and n indicates the number of layers per unit cell (cubic perovskite: $n = \infty$). The transition metal ion sits in the center of the cubic unit cell, the rare- or alkaline earth ions are located at the corners and the oxygens ions at the center of surfaces, forming an octahedron around the transition metal ion. For the here investigated compounds we have Re = La^{3+}, A = Sr^{2+} and M = $Mn^{3+/4+}$.

The cubic manganites undergo a structural phase transition at relatively high temperatures ($\approx 600 - 700\,K$), resulting in a rather complicated low-temperature structure. For instance, $La_{0.7}Sr_{0.3}MnO_3$ has a distorted rhombohedral structure, space group $R\overline{3}c$, for which a rhombohedral or a hexagonal basis can be used as shown in fig. 4.1 (a) and (b), respectively. In this structure, all oxygen positions are equivalent, i.e. all oxygen positions are obtained by symmetry operations from $\mathbf{r} = (x, x, 0.25)$. The bilayer compound has a tetragonal structure, space group $I4/mmm$, with the lattice constants $a = b = 3.86\,Å$and $c = 19.9\,Å$(fig. 4.1 (c)). Along the c axis, double layers of MnO_6 octahedra are separated by two LaO planes. There are three inequivalent positions of the oxygen atoms with respect to the MnO_2 planes of the double layer structure: in-, intra- and out-of-plane.

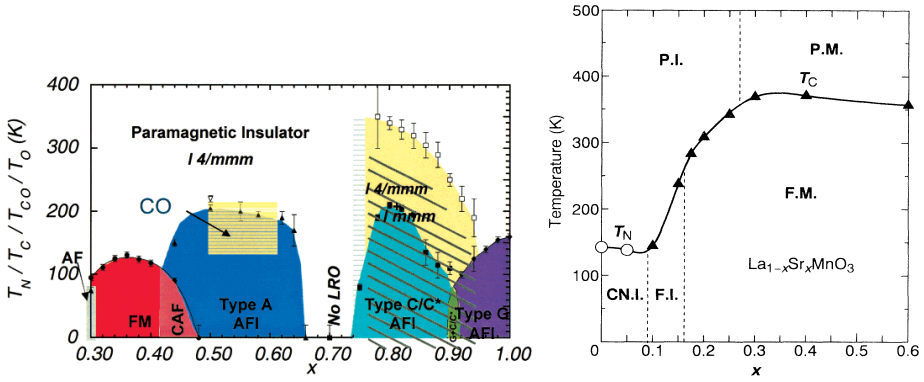

(a) $La_{2-2x}Sr_{1+2x}Mn_2O_7$ (b) $La_{1-x}Sr_xMnO_3$

Figure 4.2: Phase diagrams of (a) $La_{2-2x}Sr_{1+2x}Mn_2O_7$ [81] and (b) $La_{1-x}Sr_xMnO_3$ [82] as function of doping x.

The phase diagrams as functions of doping x for $La_{2-2x}Sr_{1+2x}Mn_2O_7$ and $La_{1-x}Sr_xMnO_3$ are shown in fig. 4.2 (a) and (b), respectively [81, 82]. Doping of the trivalent La site with the divalent Sr ion is accompanied by a change of the Mn valence from 3+ ($x = 0$) to 4+ ($x = 1$). This change of the valencies results in a rich phase diagram with many different ground states, especially for the bilayer manganite. In this work, we will focus on the doping range $x = 0.3 - 0.4$. In the bilayer manganite, a metallic-like FM groundstate is observed for $x = 0.3 - 0.4$, which undergoes a transition to a PM state with an insulator-like electrical resistivity at higher temperatures. This MI transition can be tuned by magnetic field suppressing the resistivity by over two orders of magnitude in the bilayer manganite [83]. This effect is called CMR. In the $La_{1-x}Sr_xMnO_3$ series, similar behaviors are observed for $x = 0.2 - 0.3$. However, in the here investigated compound, $x = 0.3$, both, the low and high temperature slope of $\rho(T)$ are positive with $(\delta\rho/\delta T)_{T<T_C} > (\delta\rho/\delta T)_{T>T_C}$.

4.1.2 The colossal magnetoresistance effect

The most notable of the interesting phenomena in the manganites is the outstandingly large magnetoresistance. Discovered by Helmholt et al. [72] and Jin et al. [73], this CMR (*CMR*) occurs at the phase boundary between the FM and the PM phase. More specifically, the resistivity is metallic-like at temperatures T less than the FM transition temperature, T_C, i.e. it is relatively low and increases with T, whereas at $T > T_C$ it is very large and typically decreases with T. Due to a high sensitivity of T_C to the applied magnetic field, the resistivity changes dramatically as a function of field in the vicinity of T_C.
The resistivity data of $La_{1.2}Sr_{1.8}Mn_2O_7$ as a function of temperature for $B = 0, 3, 7\,\mathrm{T}$ are shown in fig. 4.3 (a) [81]. The resistivity near $T_C = 120\,\mathrm{K}$ drops by more than

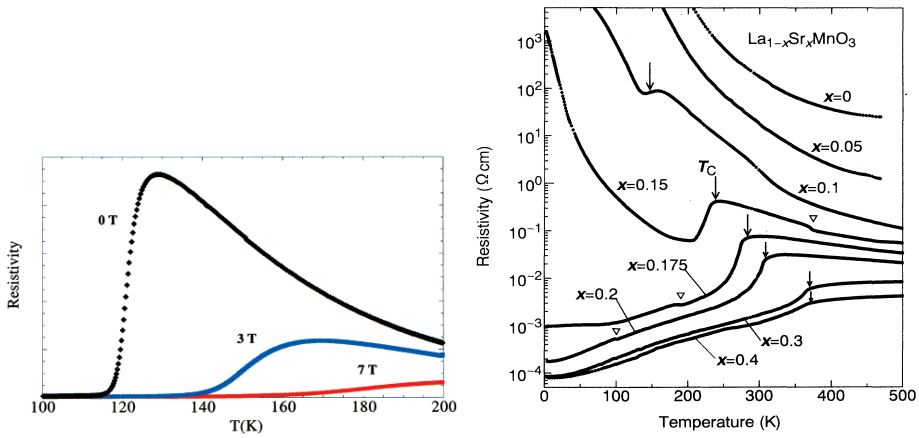

(a) $La_{1.2}Sr_{1.8}Mn_2O_7$ (b) $La_{0.7}Sr_{0.3}MnO_3$

Figure 4.3: Electrical resistivity as a function of temperature for (a) $La_{1.2}Sr_{1.8}Mn_2O_7$ in three magnetic fields [81] and (b) for $La_{1-x}Sr_xMnO_3$, $0 \leq x \leq 0.4$ [82].

compound	T_C (K)	$\rho(T_C, B=0)$ (mΩcm)	$\rho(T_C, B \neq 0)$ (mΩcm)	$\frac{\rho(T_C,B=0)}{\rho(T_C,B\neq 0)}$
$La_{1.2}Sr_{1.8}Mn_2O_7$ [81, 83, 84]	118	150	1 (B=6T)	150
$La_{0.7}Ca_{0.3}MnO_3$ [85, 86]	260	40	2 (B=5T)	20
$La_{0.75}Ca_{0.25}MnO_3$ [85]	240	106	17 (B=4T)	5
$La_{0.8}Sr_{0.2}MnO_3$ [82]	305	30	7.5 (B=15T)	4
$La_{0.7}Sr_{0.3}MnO_3$ [82]	358	7.5		<4

Table 4.1: FM transition temperatures and resistivity for zero and finite magnetic fields in some CMR compounds. Data are taken from the references as indicated.

two orders of magnitude upon cooling. Resistivity measurements for $La_{1-x}Sr_xMnO_3$ are shown in fig. 4.3 (b) [82]. The low temperature resistivity decreases upon doping by more than seven order of magnitude. The resistivity in $La_{1-x}Sr_xMnO_3$ is qualitatively similar to that in (a) for $x = 0.2 - 0.25$, but for $x \geq 0.3$ we see no insulating behavior anymore. In general, the magnetoresistance effect is relatively weak in $La_{1-x}Sr_xMnO_3$ with a reduction of the resistivity of a factor of 4 for $x = 0.2$ in an applied field of $B = 15\,\mathrm{T}$.
Tab. 4.1 lists resistivity values of some manganites, including the here investigated ones, at T_C for zero and finite magnetic fields. We note that despite the huge reduction on applying a magnetic field, even the smallest measured resistivity for $La_{1.2}Sr_{1.8}Mn_2O_7$ in the metallic-like state ($\sim 10^{-3}\Omega cm$) is still orders of magnitude higher than in good metals ($\sim 10^{-6}\Omega cm$).

4.1.3 Current ideas to explain the colossal magnetoresistance effect

The strong electron-electron and electron-lattice interactions in manganites stem from the particular electronic structure of the Mn ion. On doping the trivalent La site with divalent Sr, the valence of the Mn ion is altered from 3+ ($x = 0$) to 4+ ($x = 1$) with four or three electrons in the $3d$ shell, respectively.

The electronic structure of an isolated Mn^{3+} ion is sketched in fig. 4.4 (b) (left part). Under the influence of the crystal field, the five-fold degenerate $3d$ levels are split into three low-lying t_{2g} and two higher e_g levels. Three of the four $3d$ electrons of the Mn^{3+} ion occupy the low-lying t_{2g} levels. They are considered to be localized and form according to Hund's rule an $S = 3/2$ core spin. The fourth electron occupies an e_g orbital. The two-fold degeneracy of the e_g orbitals is lifted by the so-called Jahn-Teller (JT) effect, i.e. a distortion of the MnO_6 octahedra. The two e_g levels are separated by an energy E_{JT} and only the lower one is occupied. One such possible distortion is indicated by arrows in fig. 4.4 (a).
In undoped $LaMnO_3$ (AFM groundstate), all octahedra are distorted and consequently, all electrons are localized, because hopping to nearest neighbours would require an energy E_{JT}, which is of the order of 1 eV, i.e. much larger than k_BT. Doping the trivalent La site with divalent Sr introduces Mn^{4+} ions with only three $3d$ electrons, which occupy the t_{2g} orbitals. The Mn^{4+} ions are not JT active and, therefore, want to form undistorted MnO_6 octahedra. If an neighboring $Mn^{3+}O_6$ octahedron tries to develop a JT distortion, it must also spend some additional energy in order to elastically deform the $Mn^{4+}O_6$ octahedron. Therefore, the gain in energy for higher doping levels x by the JT distortions of the $Mn^{3+}O_6$ octahedra becomes smaller. At a certain doping level, two different ground-states have nearly the same energy: a JT distortion is not favorable anymore and the system achieves a FM groundstate, in which the $(1-x)$ e_g electrons per Mn ion form a conduction band. The electrical resistivity is dramatically reduced in the FM groundstate. On heating, the ferromagnetism is destabilized and the JT distortion again becomes more favorable: the system switches to a PM insulator for $T > T_C$. Thus, the mobility of the e_g electrons strongly depends on the fine balance between localization (JT effect) and delocalization (double-exchange, see below) and is crucial for the under-

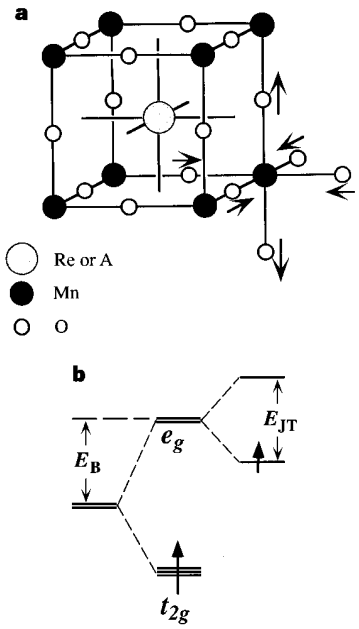

Figure 4.4: (a) Perovskite structure and (b) the effect of the crystal field on the $3d$ electronic structure of the Mn^{3+} ion. E_{JT} denotes the splitting of the e_g level due to a Jahn-Teller distortion of the oxygen octahedron around the Mn^{3+}-ion.

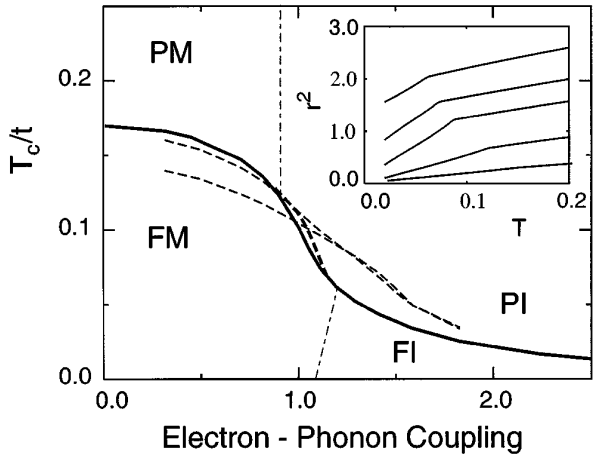

Figure 4.5: FM transition temperature (solid line) as function of the electron-phonon coupling strength λ. Regions are labeled as FM metal (FM), PM metal (PM), FM insulator (FI) and PM insulator (PI), according to the value of the magnetization and $\delta\rho/\delta T$. The inset shows calculated mean square lattice displacements versus temperature for $\lambda = 0.71(lowest), 0.9, 1.05, 1.12, 1.2$. Figure is taken from ref. [80].

standing of the MI transition in FM manganites. From the two models described below, the double exchange model investigates the impact of the electron-electron interaction via the spins, whereas the polaron picture proposes an additional important role of the electron-lattice interaction via the JT effect.

The double exchange (DE) model, proposed by Zener [75, 76] and Anderson and Hasegawa [77] and later by de Gennes [78] rests on the idea that the hopping of an electron between Mn^{3+} and Mn^{4+} is governed by a transfer integral, t, that depends explicitly on the angle Θ between classically treated core spins (assumed to be localized) on neighboring ions,

$$t = t_0 \cdot \cos\Theta/2. \tag{4.1}$$

Thus, the hopping amplitude is maximized when core spins are parallel (FM). In this treatment, the transition from a spin-disordered state at $T > T_C$ to the FM state at $T < T_C$ can be shown to increase the conductivity by a factor of two, rationalizing why the MI transition coincides with the Curie point. Likewise, for T slightly above T_C, application of a field will tend to align the spins, increasing the conductivity and leading to a large magnetoresistance.

In 1995 Millis et al. pointed out that the factor of two increase of the resistivity in the double exchange model cannot even explain the resistivity in the $La_{1-x}Sr_xMnO_3$ series [79], which exhibits a relatively small magnetoresistance. They proposed a polaronic

model involving dynamical JT fluctuations as follows [80,87]: the conventional dynamical electron-phonon coupling, which links instantaneous deviations of atoms from their ideal crystallographic positions to the instantaneous deviations of electron configuration from the average values has three important modes: a breathing distortion of the O_6 octahedron around a given Mn which couples to changes in the e_g charge density, and two volume-preserving distortions (JT modes), which couple to preferential occupancy of one e_g orbital over the other. One such distortion, indicated by arrows on fig. 4.4 (a), involves a stretching of the MnO bonds along z together with a compression in the xy plane and is favoured by occupancy of the $3z^2 - r^2$ e_g orbital. The corresponding change in the energy levels is shown in fig. 4.4 (b).
Strong electron-phonon coupling may localize charge carriers, because the presence of an electron in a given Mn e_g orbital causes a local lattice distortion, which produces a potential minimum. This minimum tends to trap the electron and dramatically increases the electrical resistivity. Such 'self-trapped' state is called a small polaron [88].
On crossing the boundary between ordered and disordered state, even a slight change in the hopping rate of the charge carriers, in view of the long time required for the distortion to lock in, can lead to a significant change in the competition between the self-trapping mechanism and the tendency towards delocalization due to DE, resulting in the observed enormous increase of the resistivity in the PM state.
In this picture, the strength of the electron-phonon coupling , λ, is directly connected to T_C, i.e. large λ means small T_C, as shown in fig. 4.5 [80]. In this figure, the FM transition temperature, T_C, is plotted versus the electron-phonon coupling strength, λ (solid line). Regions are labeled as FM metal (FM), PM metal (PM), FM insulator (FI) and PM insulator (PI), according to the value of the magnetization and $\delta\rho/\delta T$. Further calculations on polaronic models support the above presented correlation of T_C with λ [88,89].
The inset of fig. 4.5 shows the calculated atomic mean square displacement r^2 as a function of temperature for different electron-phonon coupling strengths λ [80]. Theory predicts that the temperature dependences below and above T_C are different. This prediction can be relatively easily checked by experiment. Several CMR compounds have already been measured [90–92] and our own measurement for $La_{0.7}Sr_{0.3}MnO_3$ will be presented in sect. 4.4.

4.1.4 Correlated polarons and charge order in manganites

A polaron in a manganite with $x = 0.3 - 0.4$ cannot be considered as an isolated phenomenon in an otherwise undistorted lattice. In $La_{0.7}Sr_{0.3}MnO_3$ 70% of the Mn ions are JT active and there will be strong spatial correlations between the distortions, which may lead to long range or short range order. Prominent examples of the long range order of distorted Mn^{3+} ions are the cubic parent compound $LaMnO_3$ and the 50% doped manganites. The former is a pure Mn^{3+} compound and in neutron powder diffraction data a small but significant difference in the length of the in-plane (1.924(2) Å) and out-of plane (1.9742(9) Å) short bonds, and a well separated in-plane long bond (2.177(2) Å) were observed [93]. The in-plane long bonds are aligned perpendicular to each other

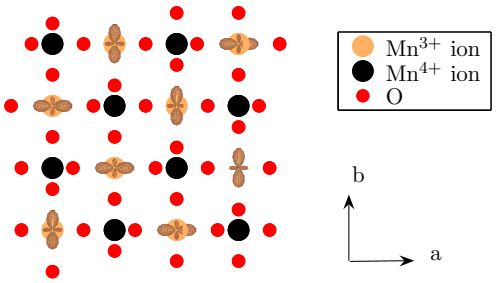

Figure 4.6: Charge-order of the CE-type as observed in $LaSr_2Mn_2O_7$ [94]. The Jahn-Teller distortion of the Mn^{3+} ions (beige dots) is indicated by the occupied e_g orbitals. The wave vector of the charge order is $\mathbf{q}_{CE} = (\frac{1}{4}, \frac{1}{4}, 0)$.

on neighbouring Mn ions reflecting the alignment of the occupied e_g orbitals.

For the 50% doped manganites with an equal share of Mn^{3+} and Mn^{4+} ions, Goodenough predicted a charge-ordered groundstate [95], in which Mn^{3+} and Mn^{4+} ions order in alternate (110) planes as shown in fig. 4.6. Wollan et al. first determined this structure in a previously published neutron scattering investigation of $La_{1-x}Ca_xMnO_3$ for a doping level of $x = 0.58$ [96]. According to their labeling of different kinds of magnetic structures, i.e. $A, B, C, D, E, ...$, this particular ordering was named C-E order. The Mn ions of different valences are arranged in a checker-board pattern, wherein the occupied e_g orbitals of the Mn^{3+} ions form a zig-zag pattern along the (110) direction. Along this direction the same pattern is repeated on each forth atom, thus the order vector is $\mathbf{q}_{CE} = (\frac{1}{4}, \frac{1}{4}, 0)$. The CE order was found to be the groundstate for $La_{0.5}Ca_{0.5}MnO_3$ [96] and later on, in other half-doped manganites including $LaSr_2Mn_2O_7$ [94,97,98]. For the doping range of the compounds studied in this work, only short range orbital order is found.

4.2 Lattice dynamical calculations using a simple shell-model

The derivation of atomic force constants from first principles, as done for YNi_2B_2C, is not yet possible for strongly correlated electron systems like the manganites. Lattice dynamical properties of strongly correlated electron systems are still the domain of phenomenological models, like the shell model [99].

The shell model is an improvement of the rigid-ion model for ionic insulators, in which short-range repulsive forces and the Coulomb interaction between the ions are taken into account. In addition, the shell model considers the atomic polarizabilities assuming that each ion consists of a spherical electronic shell which is isotropically coupled to

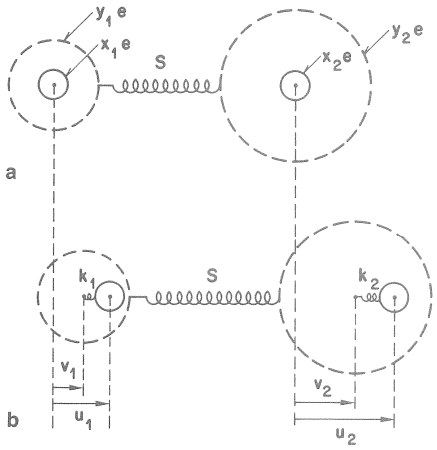

Figure 4.7: The coupling of two neighbouring ions in the simple shell model. (a) Ions in equilibrium positions and (b) ions in displaced positions with displacements of the shells $v_{1,2}$ and of the cores $u_{1,2}$. k_1, k_2 and S are the spring constants of the model. $y_{1,2}e$ and $x_{1,2}e$ are the charges of the shells and the cores of ion_1 and ion_2, respectively. Figure is taken from ref. [100].

its rigid ion-core by a spring, represented by force constants k_1 and k_2 in fig. 4.7. The inter-atomic coupling is represented by the spring S. If the intra-atomic force constants k_1 and k_2 are made infinite, the shell model is reduced to the simpler rigid−ion model again. We note that, the effective charge of an ion $z*e$ is different from its formal charge ze, usually $z*e < ze$.
The shell model was developed for the calculation of phonon dispersions in ionic insulators. The FM $La_{0.7}Sr_{0.3}MnO_3$ and $La_{1.24}Sr_{1.76}Mn_2O_7$ are certainly not insulators, but they still can be considered as ionic compounds with a certain degree of electronic delocalization. The effect of metallicity is implemented in the 'screening' parameter. It accounts for the reduced range of the Coulomb forces due to the screening effect of the conduction electrons.
Technically, the calculations are based on a huge number of phonon scans in all major crystallographic directions. The measured phonon frequencies are entered according to their symmetry classes. Then, the calculated phonon dispersions are fit to the experimentally observed values. Thus, the quality of the model, i.e. its ability to predict the 'normal' behavior of phonon branches, depends strongly on the accuracy of the underlying phonon data. We note that shell models are in the harmonic limit and, therefore, do not include higher-order effects like anharmonicity or electron-phonon coupling . In this sense, it can give new insights as an example of the 'normal' behavior, i.e. the behavior expected for coupled harmonic oscillators.

The program package GENAX, used for the shell model calculations in this work, was developed by W. Reichardt in the neutron scattering group at the Research Center

Karlsruhe and was already widely used for HTSC and other compounds.

4.3 Strong electron-phonon coupling effects in Mn-O bond stretching phonons of $La_{1.24}Sr_{1.76}Mn_2O_7$

Many-body interactions in manganites are expected to be strong and include the coupling to other electrons plus collective modes such as phonons [79], magnons [101, 102], and orbitons [103, 104]; the details of how these modes couple to the electrons, however, are still poorly understood. Although the strong JT coupling of the lattice to the electronic system is evident, a thorough investigation of the lattice dynamical properties, i.e. phonon dispersions and phonon linewidth effects due to electron-phonon coupling, is still lacking for most of the CMR manganites, except for $La_{0.7}Sr_{0.3}MnO_3$ [105, 106] and to some extent for $La_{0.7}Ca_{0.3}MnO_3$ [107].
Phonon measurements in the former compound, $La_{0.7}Sr_{0.3}MnO_3$, are extremely complicated by a distortion of the cubic perovskite structure. A doubling of the unit cell and a splitting of main cubic symmetry directions into inequivalent rhombohedral axes, i.e. the cubic $(110)_{cubic}$ direction splits into two inequivalent rhombohedral directions, $(1\bar{1}0)_{rhombo}$ and $(112)_{rhombo}$, as well as the twinning of the available samples result in up to 60 phonon branches for the main cubic axes showing up in experiment. This means that the ability to study phonons with particular symmetries by using selection rules is hampered by the structural distortion [106]. In $La_{0.7}Ca_{0.3}MnO_3$ the structure is less complicated (orthorhombic) but still rather complex.
The bilayer manganite, too, crystallizes in a relatively complicated structure. It has 12 atoms in its tetragonal unit cell ($\rightarrow$ 36 phonon branches). However, the perovskite-like structure of the MnO_6 octahedra is undistorted (fig. 4.1 (c)) and the samples are not twinned. Therefore, the inelastic neutron scattering data taken along the tetragonal directions are easier to interpret.
In this work, the dispersions and linewidths of three particular phonon branches in $La_{1.24}Sr_{1.76}Mn_2O_7$ were investigated. They are associated with JT like distortions of the MnO_6 octahedra, for which unusually strong electron-phonon coupling effects are expected. They are all of Mn-O bond stretching character and were studied along the (100) and the (110) directions. In particular, the zone boundary modes of these branches resemble JT distortions of the MnO_6 octahedra. These special modes are called:

1. the 'half-breathing' mode at $\mathbf{q}$ = (0.5, 0, 0) in the (100) direction (Δ_1 symmetry),
2. the 'planar breathing' mode at $\mathbf{q}$ = (0.5, 0.5, 0) (Σ_1 symmetry) and
3. the 'Jahn-Teller' mode at $\mathbf{q}$ = (-0.5, 0.5, 0) in the (110) direction (Σ_3 symmetry).

The branches which include the first and second modes are of longitudinal character, whereas for the JT phonon the branch has a predominantly transverse character. The

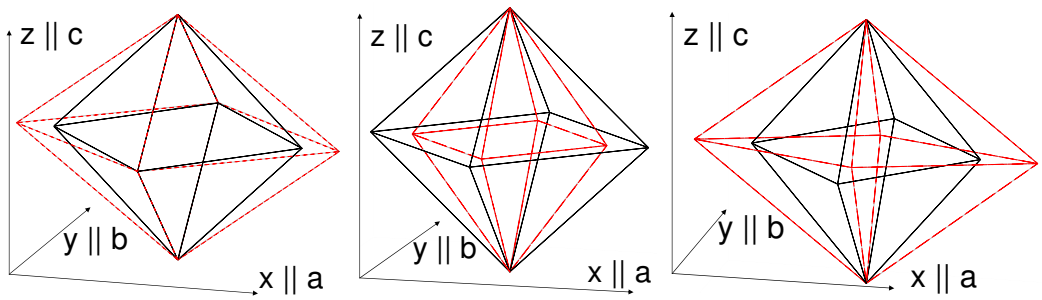

(a) Half-breathing mode at $\mathbf{q}$ = (0.5, 0.5, 0) (b) Planar breathing mode at $\mathbf{q}$ = (0.5, 0.5, 0) (c) Jahn-Teller mode at $\mathbf{q}$ = (0.5, 0.5, 0)

Figure 4.8: Calculated polarization patterns in one MnO_6 octahedron for the JT-like phonons in $La_{1.24}Sr_{1.76}Mn_2O_7$ based on a shell model (sect. 4.2). The undistorted octahedra are shown in black, the distorted ones in red. For the sake of clarity, the elongations are exaggerated. The oxygen atoms sit at the corners. The movement of the Mn ion (center of octahedron, not shown) is negligible in these phonons.

calculated elongation patterns of the three zone boundary modes are shown in fig. 4.8 for one octahedron. The central Mn ion is not marked because its movement is negligible. Oxygen atoms sit on the edges of the octahedra. The undistorted octahedra are drawn in black, the distorted ones in red. We note that the elongations are scaled up in order to better visualize the phonon patterns. The dominant atomic displacements for all shown phonons are within the (001) plane. We point out that the JT phonon at $\mathbf{q}$ = (-0.5, 0.5, 0) directly reflects the JT distortion of the MnO_6 octahedra as observed in the parent cubic compound, $LaMn^{3+}O_3$ [93].
The model used here was originally developed by W. Reichardt and M. Braden [108]. During this work, the model was refined with the help of new experimental results.
Our sample was a high-quality single-crystal of $La_{1.24}Sr_{1.76}Mn_2O_7$ with the FM transition temperature measured at 115 K. The volume of the crystal was 0.5 cm^3. The experiments were carried out on the TASs 1T at the ORPHEE reactor and IN8 at the Institut Laue-Langevin (ILL), using doubly focusing Cu220(LLB)/Cu200(ILL) monochromator and PG002(LLB)/Si111(ILL) analyzer crystals at fixed final energies of 30.5 meV or 35 meV (LLB) and 20 meV (ILL). Our measurements were performed in the constant-momentum-transfer mode, where $\mathbf{Q} = \vec{\tau} + \mathbf{q}$, and $\vec{\tau}$ is a reciprocal lattice point. We choose $\vec{\tau}$ = (4 , 0, 0) and (3, 3, 0) for measurements in the (100) and (110) directions, respectively, in order to have a negligible magnetic form factor and to maximize the phonon structure factor. The large momentum transfer ensures that the observed scattering originates from phonons rather than from magnetic scattering. If not stated otherwise, scans were made at low teperatures, $T \leq 10$ K.

4.3.1 Mn-O bond stretching phonons in the (100) direction

The first part of the phonon investigation is focused on the (100) direction. For this crystallographic direction clear phonon anomalies, generally attributed to strong electron-phonon coupling, have been observed in cubic manganites [105–107].

Phonon scans along the (100) direction in $La_{1.24}Sr_{1.76}Mn_2O_7$ are shown in fig. 4.9. An experimental background was subtracted and an offset of 500 counts for each curve was included for clarity - dashed lines denote the zero of the corresponding scans. Solid lines are gaussian fits for the Mn-O bond bending and bond-stretching modes, respectively. Because of the presence of contaminations in the ILL data, the scan at $\mathbf{Q} = (4.5, 0, 0)$ and the zone center scan were re-measured on 1T. The small peak at $E = 57\,\text{meV}$, $\mathbf{q} = (0.2, 0, 0)$ is probably due to the mixing of the eigenvectors caused by an anti-crossing of the zone center bond-bending branch with another branch with zero structure factor near the zone center. Also an interaction of this branch with the downward dispersing Mn-O bond stretching branch cannot be excluded. We neglect this minor peak in our analysis. The bond-bending mode is dominant in the whole Brillouin zone in agreement with structure factor calculations (zone center data for the bond bending phonon were scaled by a factor of 0.5 for the sake of clarity). Identifying the dominant peak as the bond-bending one, we observed an exchange of eigenvectors between the bond-bending and -stretching branch from $\mathbf{q} = (0.2, 0, 0)$ to $(0.3, 0, 0)$. While the bending mode exhibits an upward dispersion, the bond-stretching one lowers its frequency from $E = 73\,\text{meV}$ at the zone center to 53 meV at the zone boundary. This softening of $\Delta E = 20\,\text{meV}$ is similar to the softening of equivalent branches observed in $La_{0.7}Sr_{0.3}MnO_3$, $La_{0.8}Sr_{0.2}MnO_3$ and $La_{0.7}Ca_{0.3}MnO_3$ [105, 107].

The upper part of fig. 4.10 shows a comparison of calculated phonon dispersions (black lines) with the measured phonon frequencies for $\mathbf{q} = (0 - 0.5, 0, 0)$. Thick black lines denote phonons having a non-negligible calculated structure factor in the Brillouin zone investigated. Dots represent the experimentally observed frequencies for the bond-stretching (blue) and bond-bending (red) phonon peaks. Dashed lines are guides to the eye. The downward dispersion of the Δ_1 bond-stretching branch is in contradiction to the shell model, which predicts an upward dispersion towards the zone boundary. In contrast, the dispersion of the bond bending peak is well described by the shell model. The small deviation at $\mathbf{q} = (0.2, 0, 0)$ is probably due to the onset of the interaction between the two phonon branches.

The dispersion of the bond-stretching branch is not just downward but its dispersion cannot even be described by a simple cosine function. The very large negative slope between $\mathbf{q} = (0.2, 0, 0)$ and $(0.3, 0, 0)$ plus the small dip around the latter wave vector are clear signatures of strong electron-phonon coupling for this particular branch.

The lower part of fig. 4.10 shows an anylysis of the wave vector dependent evolution of the deconvoluted phonon linewidth of both the bond-bending (red) and the bond-stretching (blue) branches. Dashed lines are guides to the eye. Both branches exhibit clear maxima of their linewidths, of which the one for the bond-bending branch at $\mathbf{q}$

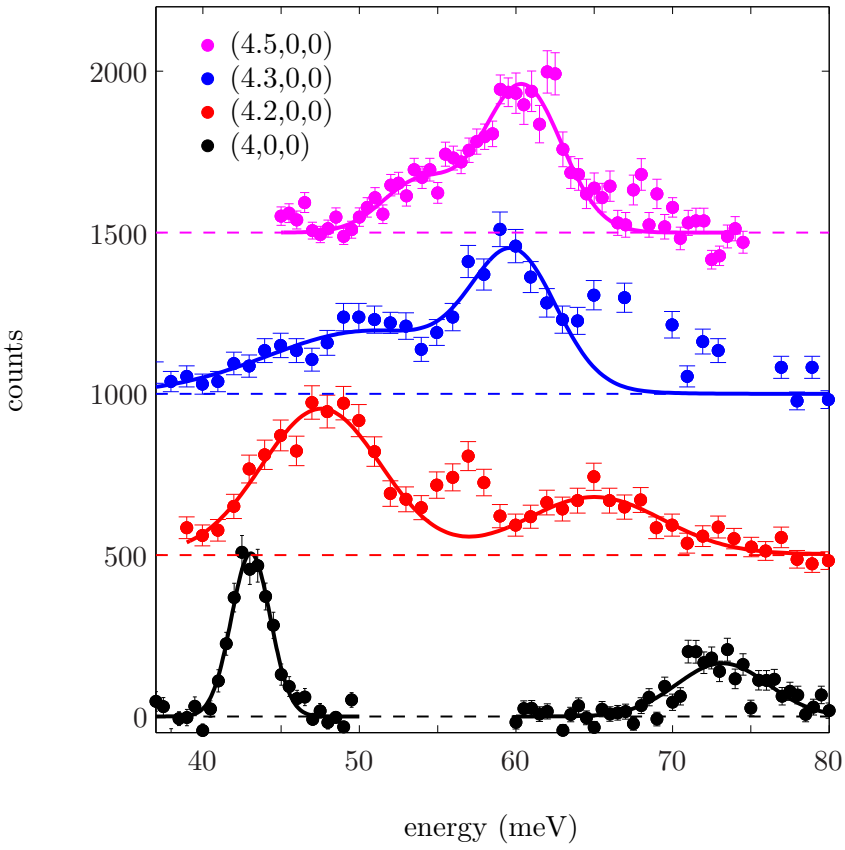

Figure 4.9: Energy scans in the (100) direction for several wave vectors. An estimate of the experimental background was subtracted. Dashed lines indicate the zero of each scan. Solid lines are gaussian fits for the main bond-bending and -stretching phonons. The high-energy part of the scan at $\mathbf{q}$ = (4.3,0,0) is contaminated by two spurious peaks. Zone center data consist of two separate scans (see text). Zone center data for the bond bending phonon were scaled by a factor of 0.5 for the sake of clarity.

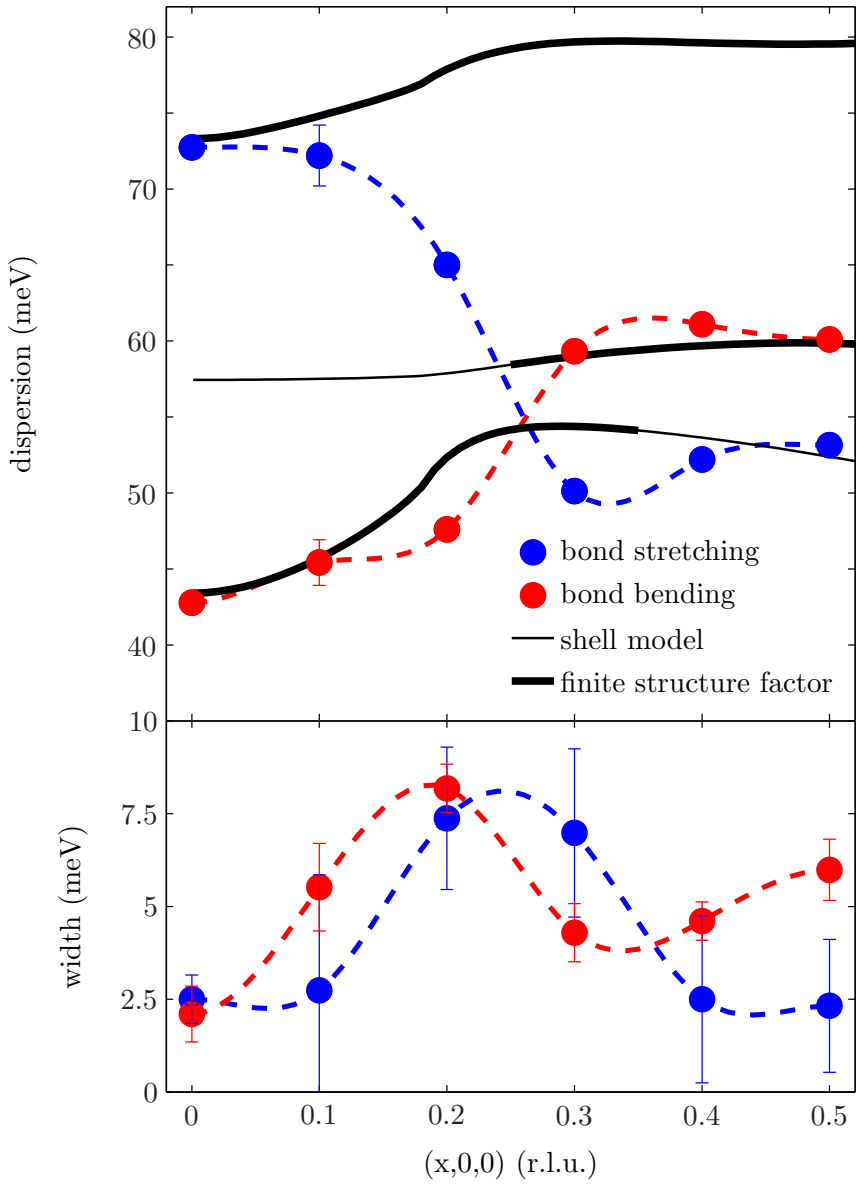

Figure 4.10: Dispersion and resolution corrected linewidths of the Mn-O bond-bending and -stretching phonons in the (100) direction. Solid lines are shell model predictions. Wave vectors with finite structure factors for the branches of interest are marked by thick solid lines. Dashed lines are guides to the eye.

= (0.2, 0, 0) is somewhat surprising because the dispersion shows no anomalies and is well described by the shell model prediction. Possibly, the interaction with the bond-stretching branch starts already at this small wave vector. The maximum broadening in the bond-stretching branch occurs halfway to the zone boundary and agrees well with the extremely steep downward dispersion of this branch.
Our data for the Mn-O bond stretching branch in the (100) direction clearly show signatures of strong electron-phonon coupling , i.e. strong softening and broadening at **q** = (0.25, 0, 0), similar to observations in other manganites [106, 107].

4.3.2 Mn-O bond stretching phonons in the (110) direction

The phonons in $La_{1.24}Sr_{1.76}Mn_2O_7$ were already studied to some extent by Reichardt and Braden [108]. However, they were unable to follow the dispersion of the JT-like Mn-O bond stretching branches in the (110) direction up to the zone boundary. Therefore, we made a new attempt to study these branches in detail.
Here, we report low temperature phonon scans along the (110) direction, measured with $\mathbf{Q} = \overrightarrow{\tau} + \mathbf{q}$, $\overrightarrow{\tau} = (3, 3, 0)$. By scanning along $\mathbf{q} = (0, 0, 0) - (\pm 0.5, 0.5, 0)$ we were able to select separately the branches of either predominantly longitudinal (+,Σ_1 symmetry) or transverse (-,Σ_3 symmetry) character.
We focused on the Mn-O bond stretching branches in the (110) direction, because both longitudinal and transverse vibrations involve lattice distortions corresponding to a polaronic state (see fig. 4.13). We note that single-site JT polarons should couple most strongly to the zone boundary transverse phonon in the same direction (see fig. 4.8 (c)).

Fig. 4.11 shows representative scans for **q** values from the zone center to the zone boundary. The peak corresponding to the bond-stretching vibration at the zone center, at **Q** = (3, 3, 0), is observed at 73 meV (fig. 4.11 (a)). The scan was not extended down to the energy of the bond bending vibration at 43 meV (fig. 4.9) because its structure factor is zero in this Brillouin zone. Bond bending phonons acquire a non-zero structure factor away from the zone center resulting in a double peak structure for scans with $\mathbf{q} \geq$ (0.2, 0.2, 0). We note that the sharp peak at $E = 52$ meV in panel (f) is spurious. The dashed line represents an estimate of the experimental background, which we assumed to be **Q**-independent in the small wave vector range of our experiment. Below 65 meV it was obtained from a fit to the zone center data. Above 65 meV, where the bond stretching phonon appears at the zone center, the background curve represents a fit to the data at **Q** = (2.75, 3.25, 0).
The transverse bond stretching branch disperses downwards, whereas the bond bending one disperses slightly upwards from 45 meV to 51 meV. While the bond bending branch exhibits no prominent linewidth changes with increasing **q**, the bond stretching one broadens strongly half way to the zone boundary (fig. 4.11 (c)) and then sharpens again (fig. 4.11 (d)).
Integrated phonon intensities give information about their eigenvectors. In the transverse direction the intensities of the phonons below 50 meV increase smoothly towards the zone boundary, wherease the phonon intensity above 50 meV does not change very much between the zone center and the zone boundary. Based on our lattice dynamical

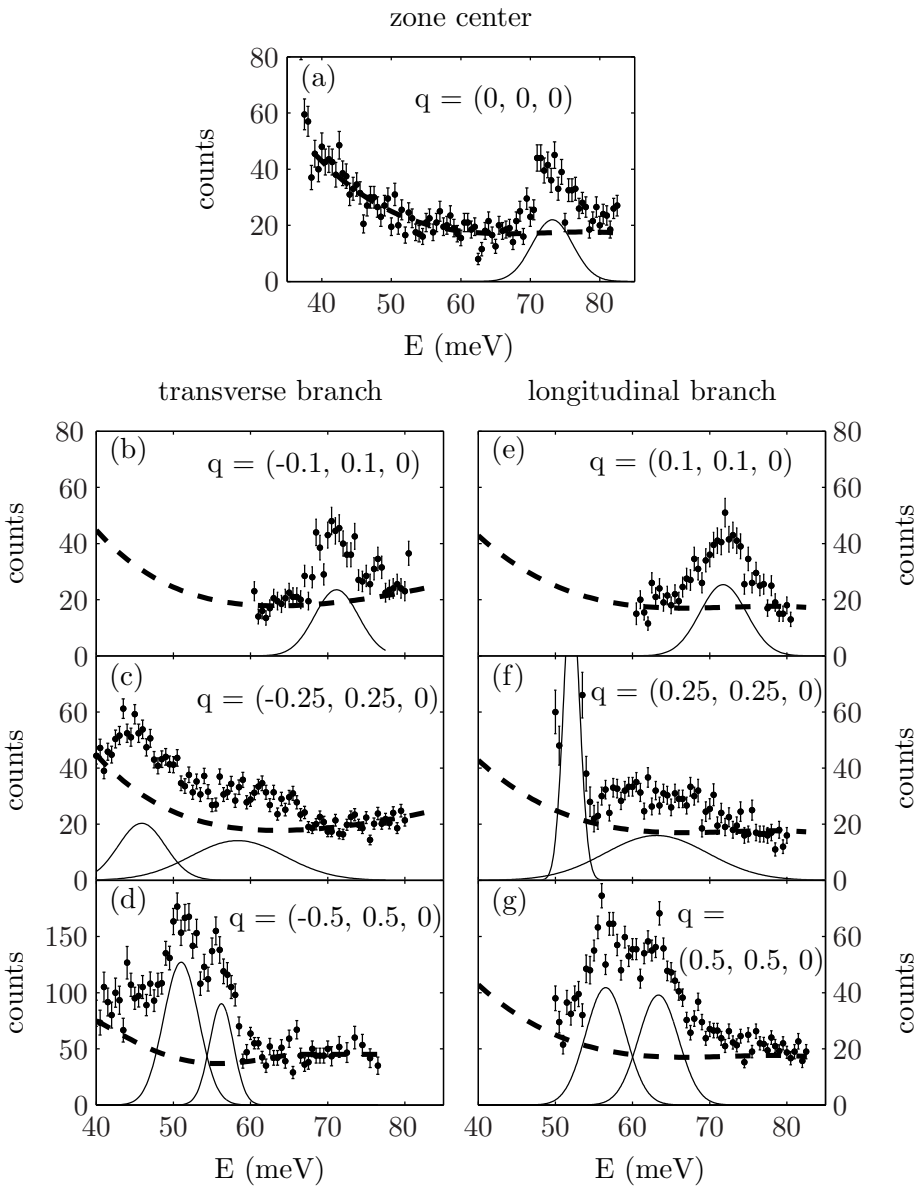

Figure 4.11: Energy scans in the Brillouin zone $\tau = (3, 3, 0)$ in $La_{1.24}Sr_{1.76}Mn_2O_7$ at $T = 10\,\mathrm{K}$. The counting rate of the transverse zone boundary phonon (d) is quantitatively different because it was measured with a different final energy $E_f = 30.5\,\mathrm{meV}$ (other scans $E_f = 35\,\mathrm{meV}$). The sharp peak at $\mathbf{q} = (0.25, 0.25, 0)$, $E = 52\,\mathrm{meV}$ is spurious.

model, this behavior is consistent with the lower branch being mostly of bond bending character, whereas the upper branch is mostly of bond stretching character. The same applies to the longitudinal branch, but only between the zone center and $\mathbf{q}$ = (0.4, 0.4, 0), because there is an abrupt change in phonon intensities further on towards the zone boundary. Such behavior indicates that the bending and stretching modes mix with other modes near the zone boundary. Here, it is meaningless to assign stretching or bending character to particular phonon peaks, instead, the stretching/bending vibrations contribute to more than one peak. Interpreting the behavior of such hybridized modes is quite complex and is outside the scope of this work; fortunately, the conclusions that we draw rely primarily on the measurements of the longitudinal pure modes for $\mathbf{q} \leq$ (0.4, 0.4, 0).

Fig. 4.12 shows the observed dispersion (a) and linewidths (b) of the transverse Mn-O bond stretching branch. The experimental dispersion is compared to shell model predictions. The strongest deviations from the shell model occur half way to the zone boundary (fig. 4.12 (a)). The experimental dispersion has a much stronger softening from $\mathbf{q}$ = (-0.15, 0.15, 0) to $\mathbf{q}$ = (-0.25, 0.25, 0) leading to a minimum in the dispersion whereas the linewidth has a pronounced maximum at the same wave vector. This enhanced renormalisation peaks at the wave vector equivalent to the CE-type order vector $\mathbf{q}_{CE}$ (see sect. 4.1.4). On the other hand, the zone boundary phonon at $\mathbf{q}$ = (0.5, 0.5, 0), whose lattice displacements correspond to the JT distortion of the undoped parent compound, has a narrow linewidth and is not strongly softened when compared to the shell model prediction. Thus, the phonons in the FM state of the CMR compounds reflect the tendency to CE order observed in half-doped manganites. In our compound ($x = 0.38$), CE order is short range and static above T_C and remains in the form of fluctuations below T_C. On the other hand, no signature is found for a strong coupling of the electrons to JT-distortions of the type found in the undoped parent compound [93].
We now discuss the longitudinal branch. Fig. 4.12 (c) shows that it also has an anomalous downward dispersion. It does not agree with the shell model even qualitatively: although the starting point at the zone center is in good agreement with the model, the calculation is more than 15 meV higher than the experiment at the zone boundary.
It is instructive here to make a comparison with the cuprates. In the 214 cuprates, like $La_{2-x}Sr_xCuO_4$, the longitudinal Cu-O bond stretching phonons in the (110) direction indeed show an upward dispersion for $x = 0$, as predicted by a corresponding shell model. We note that for zero doping La_2CuO_4 is an insulator. In contrast, the Cu-O bond-stretching branch shows a pronounced softening with increased doping around the zone boundary [109]. This softening is the strongest in the overdoped compound ($x = 0.3$), which is close to a conventional metal, so this doping-induced zone boundary softening is most probably a reflection of increased metallicity of the cuprates with increased doping rather than an exotic correlation effect. Thus we conclude that the overall downward dispersion of the longitudinal branch in our sample is a reflection of its metallicity rather than of the JT effect.
A dramatic difference between the phonons of $La_{1.24}Sr_{1.76}Mn_2O_7$ and the cuprates is observed half way to the zone boundary: here, a huge line broadening and an abrupt additional softening are observed in $La_{1.24}Sr_{1.76}Mn_2O_7$ (fig. 4.12 (d)), but not in $La_{1.7}Sr_{0.3}CuO_4$.

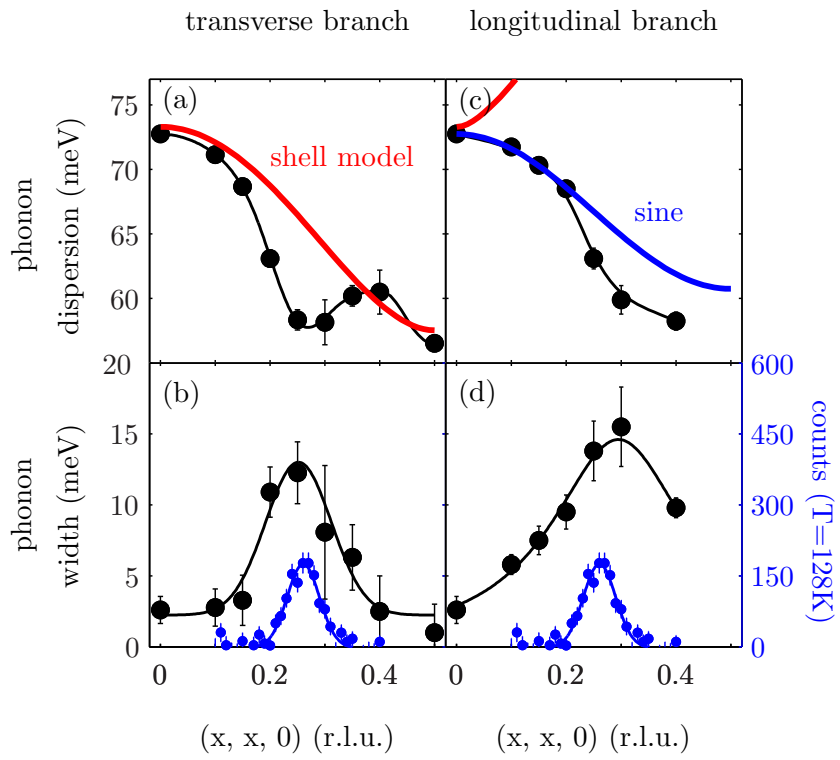

Figure 4.12: Phonon frequencies and intrinsic linewidths of Mn-O bond-stretching vibrations in $La_{1.24}Sr_{1.76}Mn_2O_7$ as obtained from inelastic neutron scattering. Experimental data (black dots) of the transverse and longitudinal branches are displayed in (a)+(b) and (c)+(d), respectively. Data shown in blue in (c) and (d) represent elastic neutron scans of the polaron peak at $T = 128\,\mathrm{K}$ and refer to the right vertical axis (blue). Red lines in (a) and (b) are shell model calculations of the phonon frequencies. The blue line in (b) is a simple sinusoidal function fitted to the first four points of the dispersion. Black lines are guides to the eye.

In $La_{2-x}Sr_xCuO_4$ with $x = 0.3$ the dispersion can be well described by a simple cosine function and there was no anomalous line broadening around $\mathbf{q} = (0.3, 0.3, 0)$ [109]. Interestingly, a very similar anomaly is observed in superconducting $La_{2-x}Sr_xCuO_4$ in the (100) direction. This anomaly has been attributed to dymanic charge stripes [110]. This similarity suggests the presence of charge fluctuations extending in the direction diagonal to the Mn-O bonds in the bilayer manganite.

Both the longitudinal and the transverse phonon anomalies may be understood in terms of coupling to the charge/orbital fluctuations of the CE type. Fig. 4.13 (a), (b) shows the eigenvectors of the longitudinal and the transverse phonons with $\mathbf{q} = (0.25, 0.25, 0)$ for the atoms in one MnO_2 plane. Fig. 4.13 (c) shows the lattice deformation associated with long-range CE order. We expect the short-range CE order to be similar. It is striking that the lattice deformation around the Mn^{3+} site in Fig. 4.13 (c) corresponds to a part of the eigenvector of the transverse phonon, whereas the deformation around the Mn^{4+} site corresponds to a part of the eigenvecotor of the longitudinal one. This matching provides a natural mechanism of strong coupling between CE-type fluctuations of both the transverse and the longitudinal phonons at the same wavevector.

All phonon measurements discussed above were performed at temperatures well below the transition temperature T_C from the FM metallic to PM insulating phase. We now discuss what happens to phonons above T_C when the static short-range CE-type order appears. It is more difficult to measure phonons in the CE-ordered phase, because static distortions result in an increase of the Debye-Waller factor, which suppresses coherent phonon intensities by almost a factor of two. This effect makes it impractical to measure bond-stretching phonons near the $\overrightarrow{\tau} = (3, 3, 0)$ reciprocal lattice vector where the structure factor is small. Thus we decided to measure temperature-dependence near $\mathbf{Q} = (5, 0, 0)$ where the structure factor is much higher, but the drawback is that the transverse and longitudinal phonons contribute equally to the total intensity. We focused the temperature-dependent measurements on $\mathbf{q} = (0.25, 0.25, 0)$ because the energies of the longitudinal and transverse modes are similar and broadening is near maximum. Fig. 4.14 (a) shows the sum of separately measured transverse and longitudinal phonons scaled together with the scattering intensity at $\mathbf{Q} = (5.25, 0.25, 0)$ ($T = 10\,\mathrm{K}$). Good agreement between the two data sets confirms that we are dealing with simple bond-stretching modes.

Fig. 4.14 (b) shows the phonon spectra at 10 K and 150 K plotted on the same intensity scale. In addition to the overall intensity decrease, a pronounced narrowing of the bond-stretching phonons is apparent at 150 K. One possible explanation for this narrowing is that the longitudinal and transverse phonons move closer together. However, the width of the combined intensity at 150 K (8 meV) is smaller than the widths of each of the phonons (12 meV and 14 meV) at 10 K (fig. 4.12). So whereas some peaks shifts cannot be ruled out, a lineshape narrowing must occur on heating to 150 K.

This result confirms that the broadening at low temperatures is of electronic origin rather than due to disorder, because disorder increases above T_C and thus has an opposite temperature dependence. This behavior indicates that CE-type fluctuations condense into static short range distortions above T_C and no longer reduce the lifetime of the optic

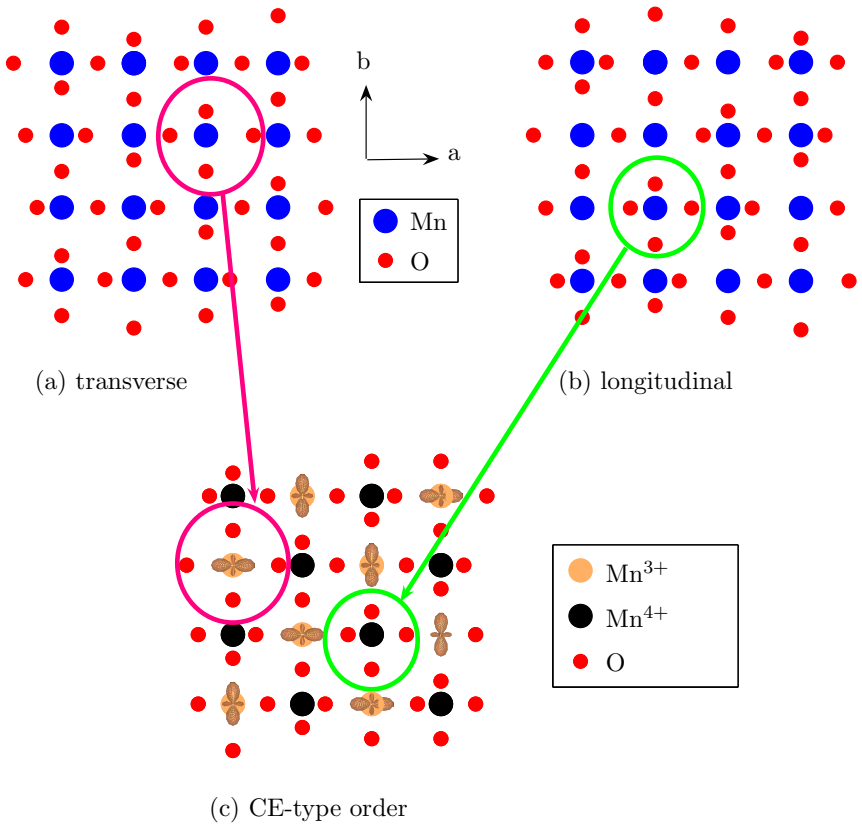

Figure 4.13: Elongation patterns of the (a) transverse and (b) longitudinal Mn-O bond stretching phonons at $\mathbf{q} = (0.25, 0.25, 0)$ as calculated from the shell model. Panel (c) shows the *CE-type* order as observed for $La_{2-2x}Sr_{1+2x}Mn_2O_7$, $x = 0.5$ [94]. For the Mn^{3+} ions the occupied e_g orbitals are depicted with their relative orientation. Magenta and green circles denote qualitatively similar surroundings of the respective Mn ions in the polarization patterns and the CE-type order.

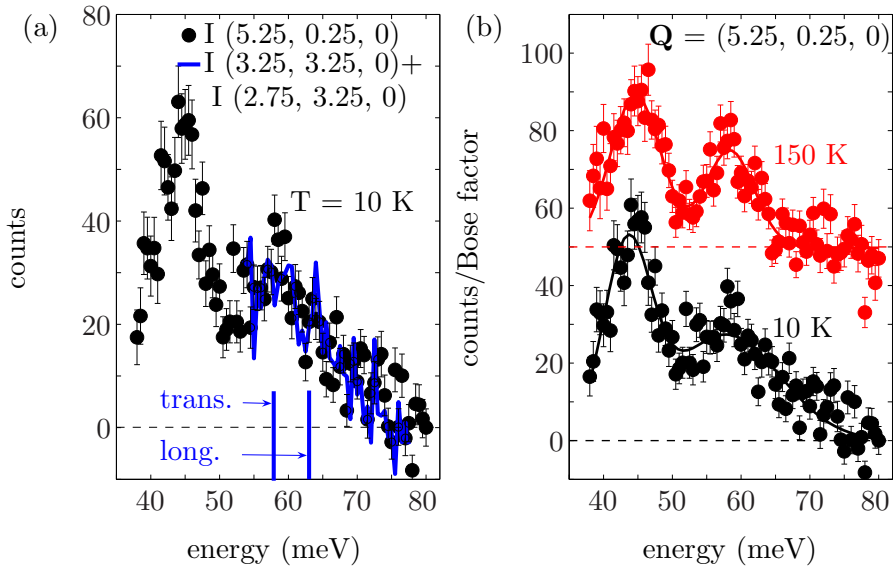

Figure 4.14: Background-corrected phonon spectra at $T = 10\,\mathrm{K}$ and $150\,\mathrm{K}$, respectively, measured at $\mathbf{Q} = (5.25, 0.25, 0)$. Temperature-dependence of the phonon linewidth was measured in the Brillouin zone adjacent to $\mathbf{Q} = (5, 0, 0)$ to increase the structure factor. Here both the longitudinal and transverse phonon intensities are superimposed. Data points in (a) show the the scattering intensity at $\mathbf{Q} = (5.25, 0.25, 0)$ whereas the line shows the sum of scattering intensities at $\mathbf{Q} = (2.75, 3.25, 0)$ and $\mathbf{Q} = (3.25, 3.25\ 0)$ scaled by an arbitrary factor. Vertical lines indicate the phonon frequencies of the transverse (58 meV) and longitudinal (63 meV) bond-stretching branches measured at $\mathbf{Q} = (2.75, 3.25, 0)$ and $\mathbf{Q} = (3.25, 3.25\ 0)$, respectively. Good agreement between the two data sets confirms that the phonon intensity above 50 meV comes from the scattering by longitudinal and transverse bond-stretching phonons, respectively. A comparison of the phonon scattering at $\mathbf{Q} = (5.25, 0.25, 0)$ at 10 K and 150 K is shown in (b). Strong broadening of the phonons on cooling is apparent only for $E > 45\,\mathrm{meV}$.

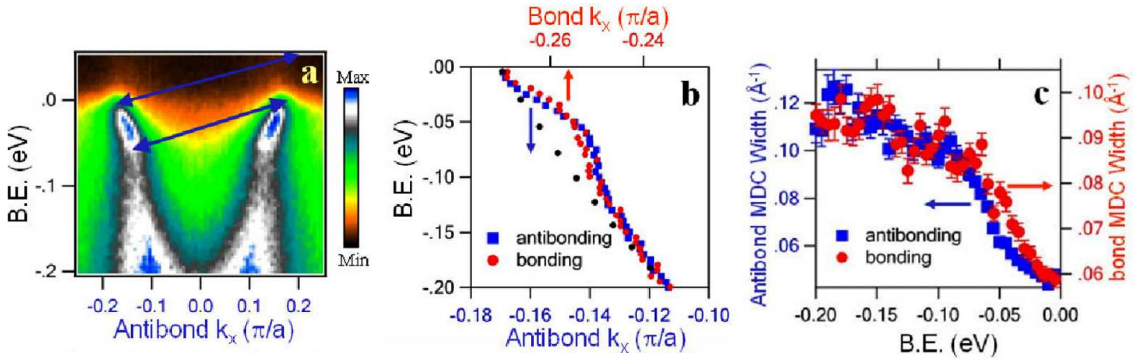

Figure 4.15: Data measured via ARPES in $La_{1.24}Sr_{1.76}Mn_2O_7$. (a) Energy versus momentum image plot of the antibonding electron band from the $k_y = 0.9\,\pi$ slice. (b) MDC derived energy versus momentum dispersion of antibonding states and bonding states compared to a parabolic fit to the deeper lying antibonding dispersion (black dots). (c) MDC full widths versus energy for antibonding and bonding states. Figure is taken from ref. [111].

phonons.

4.3.3 Discussion

Quasiparticle-like peaks in $La_{2-2x}Sr_{1+2x}Mn_2O_7$ ($x \approx 0.4$) and the coupling to bosonic modes

Many-body interactions are thought to be strong in manganites and include electron-electron as well as electron-boson coupling. Angle resolved photo emission spectroscopy (ARPES) is, like inelastic neutron scattering, an energy and momentum space resolved technique and has provided a large body of experimental results suggesting that electron-phonon coupling is important in HTSC [112].
Fig. 4.15 shows ARPES data of $La_{1.24}Sr_{1.76}Mn_2O_7$, which were published in a letter [111] including phonon measurements of our own. The experimentators empirically found, that they could selectively measure the bonding and antibonding states by varying the photon energy. (a) shows the experimental result for the antibonding states with $k_y = 0.9\,\pi$. (b) and (c) shows the momentum distribution curve (MDC, equivalent to constant energy scan) derived dispersions and linewidths of the spectral function shown in (a) for the bonding (red dots) and antibonding (blue) states, respectively. The dispersions are compared to a parabolic fit to the deeper lying antibonding dispersion (black dots). A

s-shaped kink structure, deviating from the parabolic non-interacting dispersion (black dots), can be clearly seen for both bands in the MDC derived dispersion. Simultaniously, a dramatic increase of the MDC derived width of the bonding and antibonding states was observed around the same energies as the deviation of the observed dispersion from the bare band dispersion is maximum. Model calculations showed, that such a behavior can be introduced via the coupling to a specific bosonic mode (see fig. 2 (d)-(f) in ref. [112]). It was shown that the energy of the bosonic mode is marked by the energy of the dispersion kink and also by the sharp increase of the MDC derived width of the spectral function. A key point in the bilayer manganites is that the strongly nested Fermi surface [113] should be strongly couple to a mode with a momentum transfer equal to the nesting vector $\mathbf{q} \approx (0.17, 0, 0)$ or $(0.17, 0.17, 0)$ for the antibonding band and $\mathbf{q} \approx (0.27, 0, 0)$ or $(0.27, 0.27, 0)$ for the bonding band. Following this reasoning, the energy and momentum positions of the bosonic modes responsible for the observed effects could be identified as

- $\mathbf{q} = (0.17, 0, 0)$, $E = 60 - 70\,\mathrm{meV}$ for the antibonding states and
- $\mathbf{q} = (0.27, 0, 0)$, $E = 50 - 60\,\mathrm{meV}$ for the bonding states.

At these wave vectors, the excitation energy of magnons is around 30 meV [102], and orbitons are larger than 100 meV over the entire zone [114] and so are in disagreement with the critical energy scales observed here. On the other hand, these wave vectors and energy scales coincide very well with the measured frequencies of the Mn-O bond stretching phonons in the (100) and the (110) direction (see figs. 4.10 and 4.12). The close match between the kink energies and nesting vectors on the one hand and the phonon frequencies and wave vectors on the other hand gives confidence that it is these phonons, which dominate the coupling to the quasiparticles. Especially important are the bond-stretching phonons, which should couple most strongly to the bonding and antibonding electrons (the bond-bending phonons may couple to the bonding electrons as well). The downward dispersion of the bond-stretching phonons is seen to match well with the electron kink data and is in contrast with that found for the upward-dispersive magnons [102]. In fact, the downward dispersion of the bond-stretching phonons in the (100) direction has long been considered an anomaly in manganites and other perovskites, as a simple shell-model predicts that the bond stretching phonons should have an upward dispersion [105] (see also fig. 4.10). The downward dispersion occurs at the same $\mathbf{q}$ values where the electron nesting occurs, so future studies might consider whether the coupling to the electrons renormalizes these phonon properties as well. As mentioned above, the coupling of electrons to the bond-stretching phonon branch has also been considered to be important in the cuprates [33]. The studies of electron-phonon coupling in manganites may provide opportunities to uncover the roles phonons play not only in the CMR effect but also in the pairing of electrons in HTSC cuprates.
In a previous paper, Manella et al. got similar ARPES results for the 40% doped bilayer manganite, but only for the (110) direction [115]. Their hypothesis is that the quasiparticles form a 'nodal Fermi liquid' of such a generic origin that it transcends both cuprates and manganites. The observation of strong quasiparticle-like peaks in the

antinodal regime in ref. [111] indicates that the $x = 0.36$ and $x = 0.38$ samples cannot be classified as a nodal Fermi liquid.
Unfortunately, no evaluation of the width of the quasiparticle function was published by Manella et al.. Nonetheless, the observed dispersion of the quasiparticle-like peak enables the extraction of the mode energy to which the electronic excitations couple. The evaluated energy is in a similar range as observed in ref. [111], i.e. $50 - 60\,\mathrm{meV}$. We note that the dispersion of the bond-stretching modes is quite universal for perovskite oxides and approximately independent of doping level [105, 107, 116]. Raman spectra have also proven that phonons in $La_{2-2x}Sr_{1+2x}Mn_2O_7$ ($0.38 < x < 1$) are not very sensitive to doping [117]. Therefore, neutron measurements on $x = 0.38$ samples should be a fairly good approximation for $x = 0.4$ samples. Thus, both ARPES results for quasiparticle-like peaks combined with our phonon measurements are in favor of Mn-O bond stretching phonons as the most probable candidates for the bosonic coupling counterpart.

Groundstate of $La_{1.24}Sr_{1.76}Mn_2O_7$: a polaronic metal?

Current consensus is that the dominant mechanism of resistivity increase at T_C is the competition between DE and electron-lattice interactions of the JT type, i.e. a competion of delocalization and localization of the e_g electrons of the Mn^{3+} ion. The DE interaction favors a metallic FM state, whereas the JT interaction inherited from undoped compounds favors lattice distortions that trap conduction electrons and dramatically raise the resistivity. These distortions show up in the neutron and x-ray scattering spectra as broad elastic or quasielastic peaks appearing abruptly above the FM-PM transition temperature T_C [118, 119]. Below the transition temperature average atomic positions appear to be unaffected by the JT effect. Fig. 4.16 shows a comparison of measured integrated intensities of the broad elastic peak at $\mathbf{q} \approx$ (- 1/4, 1/4, 0) across the transition temperature in $La_{1.24}Sr_{1.76}Mn_2O_7$. We compare previous measurements by Argyriou et al. [120] and new ones by our own, both on the same sample of $La_{1.24}Sr_{1.76}Mn_2O_7$, which was used throughout the present work. The integrated intensitiy abruptly decreases below $T_C = 115\,\mathrm{K}$. The inset shows elastic neutron scans in momentum space above and below T_C. The observed peaks are broadened by an intrinsic linewidth indicating a finite correlation length of the polarons.
The question is, what happens to the short range polarons present above T_C in the low temperature metallic state of $La_{1.24}Sr_{1.76}Mn_2O_7$?
Only recently, the accepted view of the groundstate of the FM bilayer manganite as a normal DE metal without strong correlations has been questioned. The electron-phonon coupling constant λ, derived from ARPES measurements [111, 115], indicates relatively strong electron-phonon coupling even at temperatures as low as $T = 20\,\mathrm{K}$ [111]. An absolute value of $\lambda = 1$ is in the intermediate−to−strong coupling regime and is such that a minor perturbation in parameters giving a small increase in the coupling strength may lead to polaronic localization. Therefore, these couplings may likely be responsible for the MI transition, which is at the heart of the CMR problem.
As discussed above, photoemission measurements [113] demonstrated that the Fermi

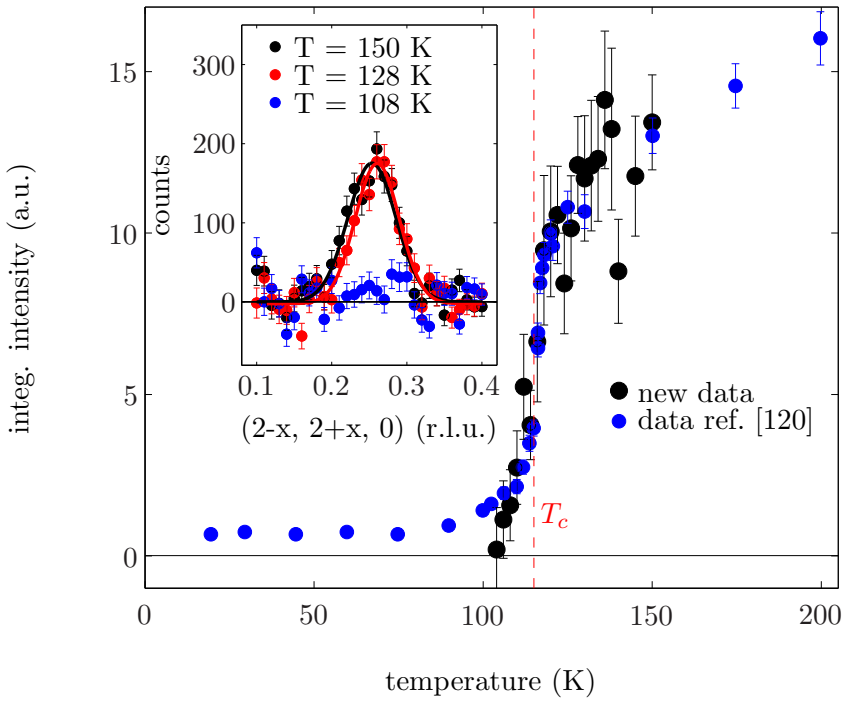

Figure 4.16: Integrated neutron intensities of the polaron peak at $\mathbf{q} \approx$ (- 1/4, 1/4, 0) in $La_{1.24}Sr_{1.76}Mn_2O_7$. New data are compared with measurements by Argyriou et al. [120]. The inset shows elastic scans in momentum space above and below the *FM M-I* transition temperature $T_C = 115\,\mathrm{K}$.

surface is very strongly nested in bilayer manganites with one of the nesting wave vectors around $\mathbf{q} = (0.25, 0.25, 0)$. This is very near the wave vectors where the phonon renormalization is at a maximum implying that the phonon effect may result from Fermi surface nesting rather than from polaron fluctuations. The simplest way to understand this possible relationship is through the standard electron-phonon coupling theory where the enhanced phonon renormalization results from increased availability of electronic decay channels. In fact it was found recently that the coherent quasiparticle spectral weight near the Fermi surface decreases towards T_C (= 120 K for that sample) and disappears at above 90 K [121]. This appears to be consistent with the narrowing of the phonons observed at 150 K. However, we found that the 90 K phonon lineshape is virtually identical to the 10 K one (data not shown), whereas the quasiparticle spectral weight decreases by a factor of two between 10 K and 90 K. Furthermore, the phonon anomaly should be much narrower in $\mathbf{q}$ space if it came from the Fermi surface nesting than is actually observed (see fig. 4.12). Thus phonon renormalization in the (110) direction is dominated not by the quasiparticles observed in photoemission, but results from a different fluctuation of the CE-type, which we assign to CE-type dynamic polaron. This fluctuation exists below T_C and then condenses into the static or quasistatic order at higher temperatures.

Therefore the metallic state in this manganite is best viewed as that of a polaronic metal as opposed the more conventional DE metal. This exotic phase combines quasiparticles with a Fermi surface with collective modes inherited from the polaronic insulator above T_C. A quantitative theory of such a system is still to be developed. Here one cannot avoid invoking similarities with the underdoped cuprates in which charge fluctuations in the form of stripes show a similar phonon renormalization along the (100) direction [110]. It is intriguing that the magnitudes of both the real and imaginary parts of the phonon self-energies in cuprates at $\mathbf{q} \approx (0.25\ ,\ 0,\ 0)$ and in the manganites at $\mathbf{q} \approx (0.25,\ 0.25,\ 0)$ at low temperatures are very similar, implying very similar mechanisms of electron-phonon coupling. This similarity indicates that dynamic charge stripes in the cuprates are in some respects similar to the fluctuating CE polarons in the manganites. Exploring this connection further may shed light on many unresolved questions for both classes of compounds.

4.4 Reduction of lattice coherence associated with the magnetic transition

In ref. [79] Millis et al. calculated the temperature dependent resistivity using the double exchange hamiltonian and found a clear underestimation of the experimentally observed effects across the FM transition temperature T_C. The authors proposed a 'polaronic' picture as was discussed in sect. 4.1.3. They pointed out that a measurement of the temperature dependence of the atomic mean-square displacements $\langle\widehat{u}^2\rangle$ (r^2 in inset of fig. 4.5 [80]) allows a stringent test of their model.
The highest FM transition temperatures, which are indicative of relatively weak electron-phonon coupling in Millis' theory, are found in the $La_{1-x}Sr_xMnO_3$ series for $x = 0.3$. Due to this current interpretation of the value of the transition temperatures in CMR manganites and the fact, that for $La_{0.7}Sr_{0.3}MnO_3$ no short-range order has been observed like in the Ca doped compounds, no detailed measurement of the atomic mean square displacements as function of temperature was made in $La_{0.7}Sr_{0.3}MnO_3$. The view that the polaronic picture does not apply to $La_{0.7}Sr_{0.3}MnO_3$ is supported by the fact that the change of the resistivity across T_C is small (fig. 4.3 (b)). In other words, $La_{0.7}Sr_{0.3}MnO_3$ was considered as a canonical DE compound. However, the strong renormalization of phonon frequencies at low temperatures and the observed intensity changes of phonons with large oxygen amplitudes in Sr doped cubic manganites (x=0.2, 0.3) [105, 106, 122] are evidence of a strong electron-phonon coupling in Sr doped manganites as well, similar to what was observed in the Ca doped compound [107].
We made elastic neutron powder diffraction measurements in order to obtain the anisotropic mean-square displacements $\langle\widehat{u}^2\rangle_{aniso}$ of the oxygen atom, which should show most clearly the lock-in of a JT type distortion of the MnO_6 octahedron. The atomic mean square displacements $\langle\widehat{u}^2\rangle$ can be determined from the Debye-Waller factor which describes the redistribution of elastic intensity due to static and dynamic displacements of the atoms from their equilibrium positions. The coherent elastic cross section is given as [5]

$$\left(\frac{d^2\sigma}{d\Omega\, dE'}\right)_{coh\,el} = \frac{\sigma_{coh}}{4\pi} N \times exp(-2W) \sum_l exp\,(i\overrightarrow{Q}\cdot\overrightarrow{l}\,)\,\delta(\hbar\omega) \tag{4.2}$$

$$\text{Debye-Waller factor } exp\{-2W(Q)\},\ 2W(Q) = \langle\{Q\cdot\widehat{u}\}^2\rangle \tag{4.3}$$

$$\text{mean square displacement } \langle\widehat{u}^2\rangle = \langle\widehat{u}^2\rangle_{stat} + \langle\widehat{u}^2\rangle_{dyn} \tag{4.4}$$

The dynamical contribution to the mean square displacement stems from phonons and the zero-point vibrations. The static part can originate from chemical disorder but also from polaronic or orbital order. In order to extract the additional contribution to $\langle\widehat{u}^2\rangle$ due to polaron formation, $\langle\widehat{u}^2\rangle_{JT}$, we extrapolate the values of $\langle\widehat{u}^2\rangle_{exp}$ at $T << T_C$ to higher temperatures based on a shell model calculation and assign any extra increase to $\langle\widehat{u}^2\rangle_{JT}$ that, according to the Millis theory, is responsible for CMR.

4.4.1 Rietveld refinement of neutron powder diffraction data

In this chapter, results of neutron powder diffraction measurements are presented. The experiment was done at the HMI on the fine resolution powder diffractometer 'FIREPOD' E9. The sample of high quality $La_{0.7}Sr_{0.3}MnO_3$ powder was mounted in a standard ^{4}He Orange cryofurnace which enabled us to make measurements up to $T = 530\,\mathrm{K}$. The diffraction patterns were analysed in an Rietveld refinement procedure using the programm package FULLPROF [123]. In this analysis we used the hexagonal basis of the rhombohedral structure of $La_{0.7}Sr_{0.3}MnO_3$, space group $R\overline{3}c$, as shown in fig. 4.1 (b). In addition to the crystallographic unit cell, a magnetic unit cell containing the Mn ions was used in the fitting procedure for $T \leq T_C$. Data were collected above and below the FM transition temperature $T_C = 358\,\mathrm{K}$ from $T = 43\,\mathrm{K}$ up to $530\,\mathrm{K}$. As monochromator we used a Ge(711) single crystal producing a neutron wave length $\lambda = 1.30782\,\text{Å}$. We used a relatively short wavelength instead of the standard one, $\lambda = 1.79764\,\text{Å}$ in order to maximize the influence of the Debye-Waller factor, which scales with $\mathbf{Q}^2$, the maximum value of which is limited by the wave length used.
In fig. 4.17 two diffraction patterns at $T = 43\,\mathrm{K}$ and $T = 530\,\mathrm{K}$ are shown. Blue dots are observed neutron-diffraction intensities, and the solid lines are calculated intensities using the programm package FULLPROF. Note the near disappearence of several peaks above the FM phase transition, for example the peak just below $2\Theta = 30^o$, because of the vanishing magnetic contribution. The following parameters are refined:

1. lattice constants a, b, c
2. magnetic moment
3. oxygen position $\mathbf{r} = (x,\, x,\, 0.25)$
4. isotropic $\langle \widehat{u}^2 \rangle$ for La/Sr and Mn ions
5. anisotropic $\langle \widehat{u}^2 \rangle_{oxygen}$

The results for the lattice constants and the magnetic moment are shown in fig. 4.18. The c-axis value (panel (a)) has no special behavior over the whole temperature range. Also the magnetic moment (panel (c)) shows the expected FM transition at $T_C = 358\,\mathrm{K}$, but the value $\mu_{43\,\mathrm{K}} = 3.22\,\mu_B$ is slightly smaller than the reported value of $\mu_{ref} = 3.5\,\mu_B$ [82]. Somewhat surprisingly, a spike-like behavior is observed for the axes of the hexagonal basal plane (panel (b)). The role of the oxygen ion in $La_{0.7}Sr_{0.3}MnO_3$ is somewhat different than in the Ca doped compound or in the bilayer manganite because there is only a single oxygen position in $La_{1-x}Sr_xMnO_3$, whereas in the other compounds there are 2 or even 3 inequivalent oxygen positions, respectively. Thus, in $La_{0.7}Sr_{0.3}MnO_3$ all positions of the oxygens in the unit cell can be calculated by symmetry operations from one original position, $\mathbf{r}_{oxygen} = (x,\, x,\, 0.25)$. The fit values of x are displayed in fig. 4.18 (d) in relative lattice constants (r.l.c.) versus temperature. For $T < T_C$ x stays nearly constant but strongly decreases for $T > T_C$. The latter two results indicate a strong lattice response to the phase transition. The isotropic mean square displacements of La,

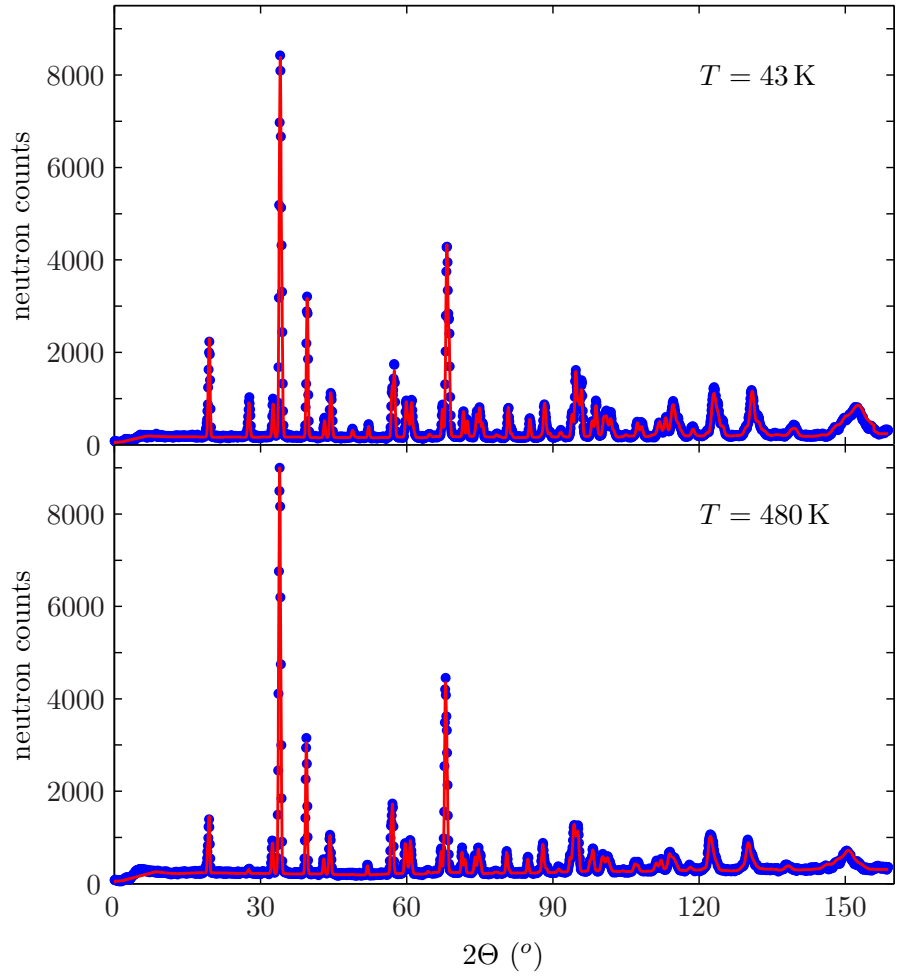

Figure 4.17: Rietveld refinement patterns for $La_{0.7}Sr_{0.3}MnO_3$ at 43 K and 480 K. Dots are observed neutron-diffraction intensities, and the solid lines are calculated intensities using the programm package FULLPROF [123].

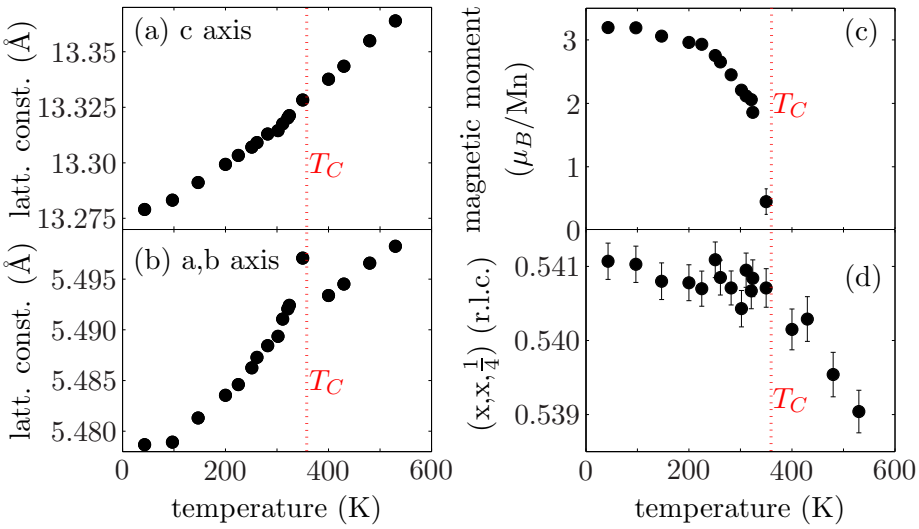

Figure 4.18: Lattice constants (a)+(b), magnetic moment (c) and oxygen position (d) of $La_{0.7}Sr_{0.3}MnO_3$ as a function of temperature as obtained from high-resolution neutron powder diffraction data. Error bars in (a)-(c) are smaller than the symbols. Dashed lines indicate the FM metal-insulator transition temperature $T_C = 358\,\mathrm{K}$.

Sr and Mn showed no response to the FM transition (not shown).

The reason for extracting not only an isotropic $\langle\widehat{u}^2\rangle_{iso}$ for the oxygen ion but anisotropic values is that the $\langle\widehat{u}^2\rangle$ along the Mn-O bond should be most affected if the electron-phonon coupling leads to a JT distortion. In the analysis, the anisotropic $\langle\widehat{u}^2\rangle$ are given as the three main axes of an ellipsoid. We emphasize that the orientation of the ellipsoid is not pinned during the fitting process. It is expected that the $\langle\widehat{u}^2\rangle$ along the Mn-O bond is the smallest one because the bond is hardest in this direction, as can be seen from the high frequencies of the Mn-O bond stretching phonons [105, 106].

Results for the anisotropic mean square displacemnts are shown in fig. 4.19. Blue and cyan dots are the values perpendicular to the Mn-O bond, $\langle\widehat{u}^2\rangle_{\perp,1}$ and $\langle\widehat{u}^2\rangle_{\perp,2}$, respectively. The smallest component of $\langle\widehat{u}^2\rangle$, black, is indeed along the Mn-O bond, $\langle\widehat{u}^2\rangle_{\parallel}$. Lines are shell model calculations (see sect. 4.2) representing the expected behavior in the harmonic approximation. Because we are mainly interested in the temperature dependent increase and not the absolute value at zero temperature, the shell model predictions include an offset in order to better visualize the different temperature dependencies.

The inset displays the original oxygen ion (red) at $\mathbf{r}$ = (x, x, 0.25) surrounded by two Mn ions (green). The dashed line indicates the Mn-O bond. Black arrows represent the obtained values and directions for the anisotropic mean square displacement ellipsoid. The largest component, $\langle\widehat{u}^2\rangle_{\perp,1}$, is in the (110) plane but perpendicular to the Mn-O bond (blue dots), the other component perpendicular to the bond, $\langle\widehat{u}^2\rangle_{\perp,2}$, lies in the

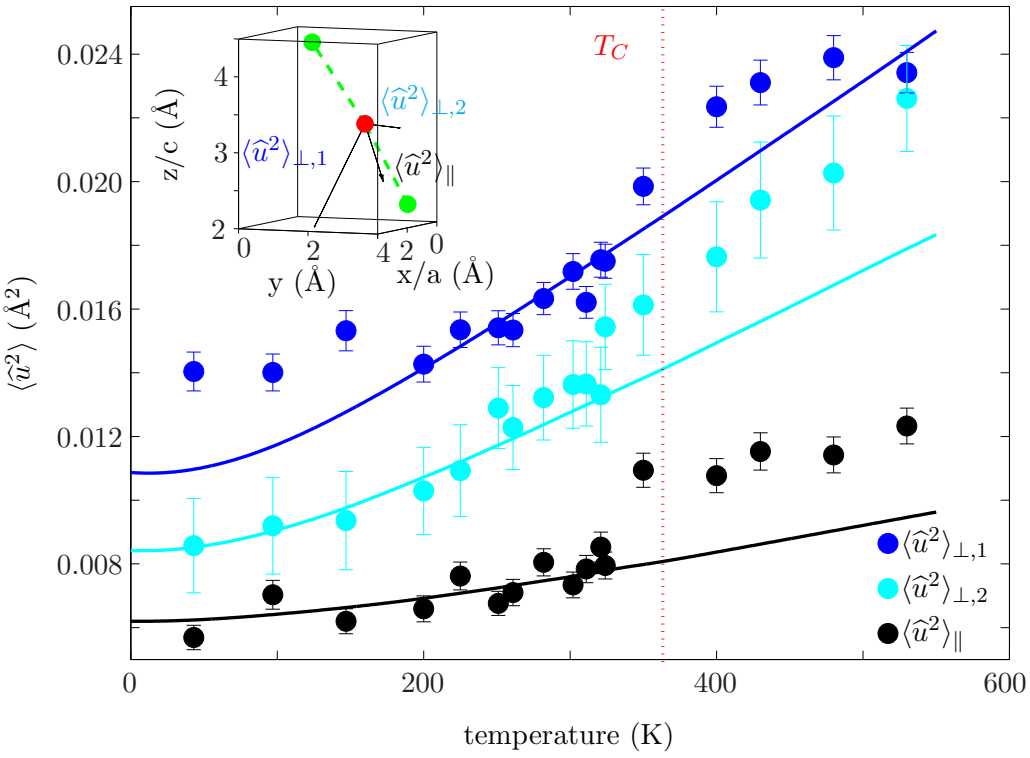

Figure 4.19: Anisotropic oxygen mean square displacements $\langle \hat{u}^2 \rangle$ in $La_{0.7}Sr_{0.3}MnO_3$ versus temperature as obtained from high-resolution neutron powder diffraction data. Lines are shell model calculations based on phonon measurements [106]. The inset shows an oxygen atom (red) surrounded by two Mn ions (green) in orthogonal axes x, y, z ($a = x$, $c = z$, but $b \neq y$). Dashed lines indicate the bond directions. Black arrows denote the obtained $\langle \hat{u}^2 \rangle$ parallel and perpendicular to the Mn-O bond.

(001) plane (cyan dots), while the shortest arrow, $\langle\widehat{u}^2\rangle_{\parallel}$, points along the bond direction $(1\overline{1}\frac{1}{2})$ (black dots). $\langle\widehat{u}^2\rangle_{\perp,1}$ and $\langle\widehat{u}^2\rangle_{\perp,2}$ points toward the next La/Sr site (La/Sr sites not shown).
For $\langle\widehat{u}^2\rangle_{\parallel}$ the temperature dependence is nearly the same as predicted below and above T_C. However, at $T = 350\,\mathrm{K}$ we see a step-like increase in the experimental data of $\Delta\langle\widehat{u}^2\rangle_{\parallel} = 0.003$ Å^2, which is 38% of the calculated value at T_C and nearly doubles the observed increase between $T = 0$ and $T = 325\,\mathrm{K}$, $\Delta\langle\widehat{u}^2\rangle_{0\to 325\,\mathrm{K}} = 0.0017$ Å^2. For $\langle\widehat{u}^2\rangle_{\perp,2}$ (cyan) we also observe good agreement below T_C and a sudden deviation from the model above T_C, though it is not as sharp and strong, $\Delta\langle\widehat{u}^2\rangle_{\perp,2} = 0.0023$ Å^2, as for $\langle\widehat{u}^2\rangle_{\parallel}$. For the largest component, $\langle\widehat{u}^2\rangle_{\perp,1}$, we observed the smallest change at T_C, while the whole temperature dependence, as expected, is strongest for this direction, indicating the relative softness of the bond in this direction.

4.4.2 Discussion

The starting point for the above described investigation was the current point of view that the magnitude of the mean square deviation from the average periodic structure $\langle\widehat{u}^2\rangle$ controls how strongly the electrons are trapped. In the theory $\langle\widehat{u}^2\rangle$ depends sensitively not only on the electron-phonon coupling strength, but also on the intersite hopping probability t: the longer the electron stays on the same site, the more time there is for the lattice to relax into the energetically favorable distorted configuration. Thus a modest reduction in t when ferromagnetism is destroyed above T_C (because of DE) leads to a large increase in $\langle\widehat{u}^2\rangle$, and a corresponding jump of the resistivity. Similarly, the variation of T_C with composition should scale with the electron-phonon coupling strength according to the theory [79,80,88]. Contrary to the expectation of this picture, we found that large changes in the strength of the CMR effect as a function of composition are not accompanied by an expected variation in the increase of $\langle\widehat{u}^2\rangle$ associated with T_C. It appears that the strength of CMR is not controlled by the magnitude of lattice distortions alone.
Fig. 4.20 illustrates this point. Here, we make a comparison of data for $La_{0.7}Sr_{0.3}MnO_3$ (a) with data for three other compounds, (b) $La_{1.2}Sr_{1.8}Mn_2O_7$, (c) $La_{0.75}Ca_{0.25}MnO_3$ and (d) $La_{0.65}Ca_{0.35}MnO_3$, all of them exhibiting much stronger CMR effects than $La_{0.7}Sr_{0.3}MnO_3$ (see tab. 4.1). Experimental data of (b), (c) and (d) are taken from Refs. [90–92], respectively. All solid lines are once more shell model calculations. However, only models for $La_{0.7}Sr_{0.3}MnO_3$ and $La_{1.24}Sr_{1.76}Mn_2O_7$ were developed in our group. Hence, lines in panel (c) and (d) represent calculations for $La_{0.7}Sr_{0.3}MnO_3$. In the lowest panel, the differences between observed and calculated $\langle\widehat{u}^2\rangle$ for the various compounds shown in panels (a) - (d) are plotted as a function of T/T_C.
First we see that all compounds show a strong increase of $\langle\widehat{u}^2\rangle_{exp} - \langle\widehat{u}^2\rangle_{model}$ at $T = T_C$. But while the increase is step-like for $La_{0.7}Sr_{0.3}MnO_3$ and $La_{1.24}Sr_{1.76}Mn_2O_7$, $\langle\widehat{u}^2\rangle_{exp} - \langle\widehat{u}^2\rangle_{model}$ of the Ca doped compounds starts to increase smoothly well below T_C. Above T_C, the results for all compounds are practically constant.
Most importantly, there is clearly no scaling of $\langle\widehat{u}^2\rangle_{exp} - \langle\widehat{u}^2\rangle_{model}$ above T_C with

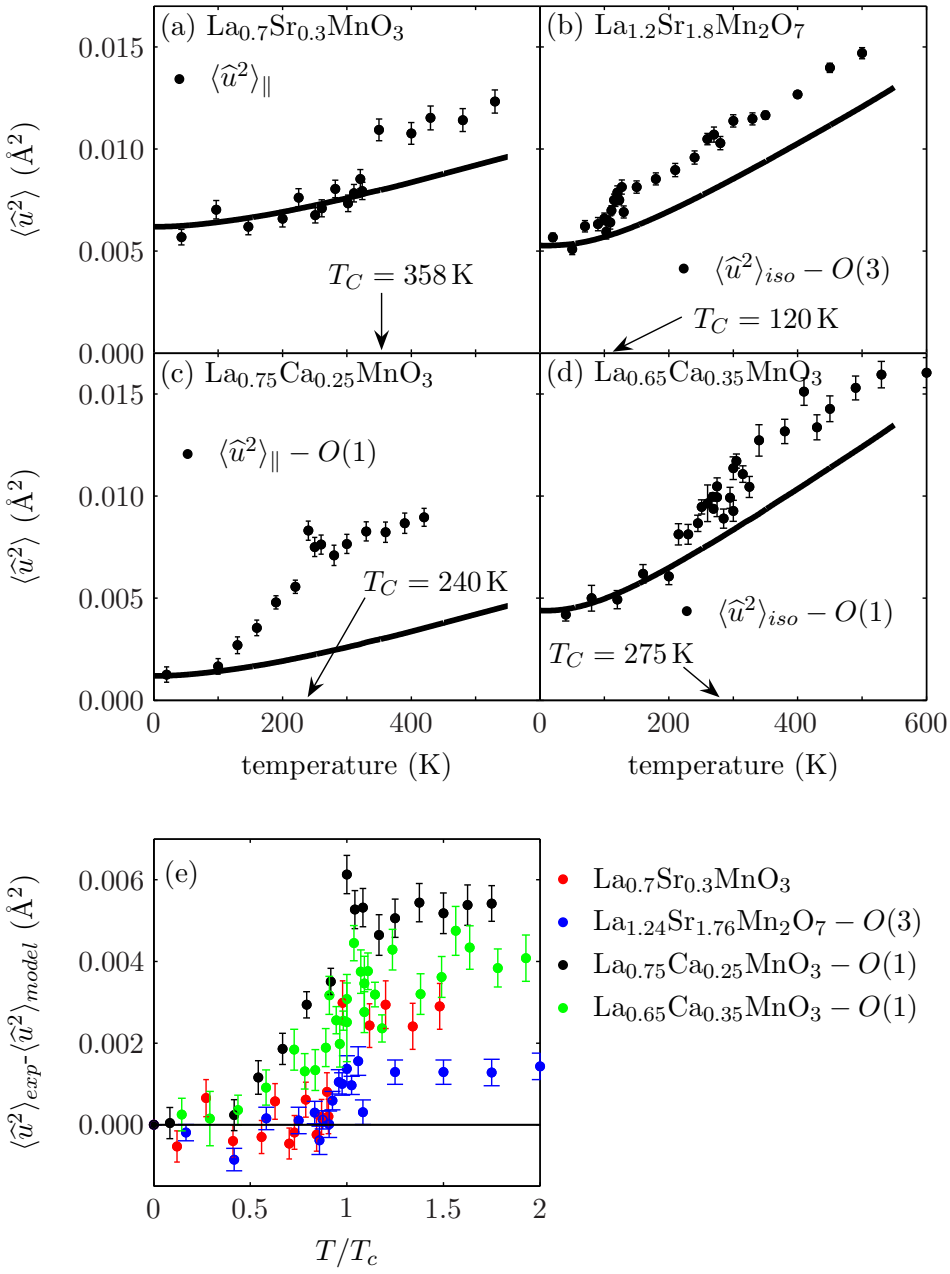

Figure 4.20: Mean square displacements of oxygen atoms in (a) $La_{0.7}Sr_{0.3}MnO_3$, (b) $La_{1.2}Sr_{1.8}Mn_2O_7$, (c) $La_{0.75}Ca_{0.25}MnO_3$ and (d) $La_{0.65}Ca_{0.35}MnO_3$. Lines are shell model calculations. Lines in (c) and (d) are the corresponding calculation for $La_{0.7}Sr_{0.3}MnO_3$ because no model data for $La_{0.75}Ca_{0.25}MnO_3$ and $La_{0.65}Ca_{0.35}MnO_3$ were available. In (e) the differences of the experimental data minus model values are shown. Experimental data of (b), (c), (d) are taken from Refs. [90–92], respectively. Oxygen positions are labelled as in the references.

the observed CMR effect. The values for the 'canonical' double exchange compound $La_{0.7}Sr_{0.3}MnO_3$ lie well above those for $La_{1.24}Sr_{1.76}Mn_2O_7$ and are in close vicinity to the values of $La_{0.65}Ca_{0.35}MnO_3$.

Another property, which is affected by the Debye-Waller factor and hence by $\langle \widehat{u}^2 \rangle$, is the intensity of coherent one-phonon scattering. A comparison of phonon intensities of high energy Mn-O bond stretching phonons in $La_{1.24}Sr_{1.76}Mn_2O_7$, $La_{0.7}Sr_{0.3}MnO_3$ and $La_{0.2}Sr_{0.2}MnO_3$ measured at $\mathbf{Q}$ = (4, 0, 0) and (4.95/5, 0, 0) is presented in ref. [122]. Although the T_C of the three compounds differ by a factor of three (115 K $\rightarrow$ 358 K), the renormalization of the Mn-O bond stretching phonon intensity is similar for all compounds.
Other studies have shown that there is relatively little variation in other anomalous properties between manganites with the FM ground state. For example magnon dispersion anomalies are similar in Sr and Ca-doped manganites at the same doping concentration, although the resistivity jump at T_C is much lower and the T_C is much higher in the former [124]. High energy phonon anomalies associated with T_C are also similar [105–107]. The latter clearly point to a universally strong electron-phonon coupling in the FM manganites irrespective of the strength of the CMR effect. Our results, combined with earlier studies, show that electron-phonon coupling is strong in all manganites with the FM ground state and its strength by itself determines neither the T_C nor the magnitude of the resistivity jump at T_C. Thus it is necessary to reexamine the current theoretical underpinning of the CMR phenomenon, which predicts a direct relationship between these quantities. We believe that the key to understanding CMR is in relatively subtle effects such as intersite correlations and/or dynamics of lattice distortions. These result in either dynamic or static short range CE order that appears above T_C in CMR compounds such as $La_{0.3}Ca_{0.3}MnO_3$ and does not appear in $La_{0.7}Sr_{0.3}MnO_3$ where the CMR is much smaller. We think that the rigidity of this CE order is the dominant force behind the resistivity increase above T_C. A successful theory must be able to derive this mechanism from materials' structure and chemistry.

5 Summary

YNi_2B_2C

The lattice dynamical properties of YNi_2B_2C were experimentally investigated over a large energy range in a variety of crystallographic directions. The aim was to check predictions of first-principles calculations. Quantitative agreement was found between the calculated and observed phonon frequencies, apart from the fact that the calculated frequencies are generally 3% too low.
Further, measurements of the phonon linewidths confirmed the calculated coupling strength quite satisfactorily. We found that the linewidths of some extremely strong coupling phonons are underestimated by theory indicating a somewhat higher value of the total electron-phonon coupling constant λ than the calculated $\lambda_{DFT} = 0.89$ [48]. This could explain the underestimation of the superconducting transition temperature by DFT ($T_{c,DFT} = 12.6\,\mathrm{K}$, $T_{c,exp} = 15.5\,\mathrm{K}$). In addition, it could be shown for the phonon anomaly at the M-point that it is associated with strong elongations of the light B and C atoms, which is unexpected for a low energy phonon branch. This result is important, because these light atoms contribute the dominant part to the electronic density of states at the Fermi level and thus are thought to be most important to strong electron-phonon coupling.

In the superconducting state, the temperature dependence of the superconducting gap, $2\Delta(T)$, was extracted from the temperature dependence of the lineshape of a single phonon for the first time. The analysis was based on a theory of P. B. Allen et al. [53], which describes the observed superconductivity-induced changes of the phonon lineshapes in a semi-quantitative way. We could show that there is no need to invoke the appearance of a 'new' peak in the superconducting state as was done in ref. [24]. Investigating phonons along the (100) direction up to the zone boundary, we showed that the superconductivity-induced changes of the phonon lineshapes look qualitatively different at different wavevectors, depending on the normal state linewidth and the ratio of the phonon frequency to 2Δ. However, this different behavior can be very well understood from Allen's theory.
Surprisingly, the analysis of phonons at different wave vectors yielded different gap values. This can be understood by the assumption that phonons can get the dominant contribution to their electron-phonon coupling strength from a rather narrow section of the Fermi surface. Thus, different phonons can in principle probe the anisotropy of the gap over the Fermi surface to a certain degree. Quantitatively, we found a lower limit of the gap anisotropy of $\Delta_{max}/\Delta_{min} \geq 1.58$. We note that the smallest gap value was

found for a phonon with $\mathbf{q} = (0.5, 0, 0)$, which has a very large electron-phonon coupling strength because of the Fermi-surface nesting.

Thus, our results for the superconducting state clearly support the presence of a strongly anisotropic gap function, but on the other hand, we do not see any need to invoke the hypothesis of a non-conventional pairing mechanism. The very good agreement between our experimental data and the DFT results clearly speaks in favor of a conventional pairing mechanism. In conclusion, YNi_2B_2C can be classified as an intermediate-to-strong coupling conventional superconductor.

Colossal magnetoresistive manganites

We choose the CMR bilayer manganite $La_{1.24}Sr_{1.76}Mn_2O_7$ for our phonon investigation because the samples are untwinned which greatly simplifies the interpretation of the inelastic neutron scattering data compared to previous phonon measurements on the cubic manganites [105, 106]. The phonon dispersions for the Mn-O bond stretching and bond bending branches were found to show very similar behavior compared to the dispersions in the cubic compounds. Our measurements of the Mn-O bond stretching phonons in the (100) direction provide evidence that phonons are responsible for the strong electron-boson coupling features seen in ARPES measurements [111].

Measurements of the bond stretching phonons in the (110) direction in the ferromagnetic state of $La_{1.24}Sr_{1.76}Mn_2O_7$ yielded evidence for the presence of dynamic polarons, which are correlated similar to the CE-type order (see p. 73) observed in half doped compounds. These polarons condense on heating into a static short-range order above the Curie temperature T_C. More specifically, we found steep downward dispersion of the Mn-O bond-stretching branches half way to the zone boundary, $\mathbf{q} \approx (\frac{1}{4}, \frac{1}{4}, 0)$. Both the longitudinal and transverse branches exhibit dramatic broadening with a broad maximum near the CE wavevector $\mathbf{q} = (\frac{1}{4}, \frac{1}{4}, 0)$. In our interpretation, the renormalization of the bond stretching phonons is caused by the appearance of strong charge/orbital fluctuations. The fact that they show up at the CE order wavevector provides evidence that these fluctuations are not single site Jahn-Teller polarons - which should couple most strongly to phonons at the zone boundary - but are correlated in the CE-type manner. The ferromagnetic metal-insulator transition may be understood in terms of a condensation of these fluctuations into a static short-range CE ordered state. This condensation is unusual in that it occurs on heating rather than on cooling.

Our neutron powder diffraction results for $La_{0.7}Sr_{0.3}MnO_3$ show that polarons form above T_C to the same extent as in other CMR compounds although the resistivity jump at T_C is rather small. It proves that electron-phonon coupling is strong in all manganites with the ferromagnetic ground state and its strength by itself determines neither T_C nor the magnitude of the resistivity jump at T_C. Thus it is necessary to reexamine the current theoretical underpinning of the CMR phenomenon, which predicts a direct relationship

between these quantities. We believe that the key to understanding CMR is in relatively subtle effects such as intersite correlations and/or dynamics of lattice distortions. These result in either dynamic or static short range CE order that appears above T_C in CMR compounds such as $La_{0.7}Ca_{0.3}MnO_3$ but does not appear in $La_{0.7}Sr_{0.3}MnO_3$ where the CMR is much smaller. The rigidity of this CE order is probably the dominant force behind the resistivity increase above T_C.

Bibliography

[1] H. K. Onnes. Commun. Phys. Lab. **12**, 120 (1911).

[2] J. Bardeen, L. N. Cooper and J. R. Schrieffer. *Theory of Superconductivity.* Phys. Rev. **108** (5), 1175–1204 (Dec 1957).

[3] Bacon G. E. *Fifty years of neutron diffraction: The advent of neutron scattering.* Bristol : A. Hilger 1986.

[4] Marshall and S. Lovesey. *Theory of Thermal Neutron Scattering.* Clarendon Press 1971.

[5] G. Squires. *Introduction to the Theory of Thermal Neutron Scattering.* Cambridge University Press 1978.

[6] Bruno Dorner. *Coherent inelastic neutron scattering in lattice dynamics.* Springer 1982.

[7] G. Shirane, S. Shapiro and J. Tranquada. *Neutron Scattering with a Triple-Axis Spectrometer.* Cambridge University Press 2002.

[8] B. N. Brockhouse. *Inelastic scattering of neutrons in solids and liquids.* International Atomic Energy Agency 1961.

[9] G. Ekspong. *Nobel Lectures in Physics 1991-1995.* World Scientific 1997.

[10] S. M. Shapiro, G. Shirane and J. D. Axe. *Measurements of the electron-phonon interaction in Nb by inelastic neutron scattering.* Phys. Rev. B **12**, 4899 (1975).

[11] N. W. Ashcroft and N. D. Mermin. *Solid state physics.* Itps Thomson Learning 2000.

[12] Ch. Mazumdar, R. Nagarajan, C. Godart, L. C. Gupta, M. Latroche, S. K. Dhar, C. Levy-Clement, B. D. Badalia and R. Vijayaraghavan. *Superconductivity at 12 K in Y-Ni-B system.* Solid State Commun. **87**, 413–416 (1993).

[13] R. J. Cava, H. Takagi, B. Batlogg, H. W. Zandbergen, J. J. Krajewski, W. F. Peck, R. B. van Dover, R. J. Felder, T. Siegrist, K. Mizuhashi, J. O. Lee, H. Eisaki, S. A. Carter and S. Uchida. *Superconductivity at 23 K in yttrium palladium boride carbide.* Nature **367**, 147 (1994).

[14] R. J. Cava, H. Takagi, H. W. Zandbergen, J. J. Krajewski, W. F. Peck, T. Siegrist, B. Batlogg, R. B. van Dover, R. J. Felder, K. Mizuhashi, J. O. Lee, H. Eisaki and S. Uchida. *Superconductivity in the quaternary intermetallic compounds $LuNi_2B_2C$.* Nature **367**, 252 (1994).

[15] T. Siegrist, H. W. Zandbergen, R. J. Cava, J. J. Krajewski and W. F. Peck. *The crystal structure of superconducting $LuNi_2B_2C$ and the related phase LuNiBC.* Nature **367**, 254 (1994).

[16] L. M. Dezaneti, Y. Y. Xue, Y. Y. Sun, K. Ross and C. W. Chu. *Direct identification of the 23 K superconducting phase in the Y-Pd-B-C system.* Physica C **334**, 123 (2000).

[17] H. Eisaki, H. Takagi, R. J. Cava, B. Batlogg, J. J. Krajewski, W. F. Peck, K. Mizuhashi, J. O. Lee and S. Uchida. *Competition between magnetism and superconductivity in rare earth nickel boride carbides.* Phys. Rev. B **50**, R647 (1994).

[18] B. K. Cho, P. C. Canfield and D. C. Johnston. *Onset of superconductivity in the antiferromagnetically ordered state of single-crystal $DyNi_2B_2C$.* Phys. Rev. B **52**, R3844 (1995).

[19] P. C. Canfield, B. K. Cho, D. C. Johnston, D. K. Finnemore and M. F. Hundley. *Specific heat and anisotropic superconducting and normal-state magnetization of $HoNi_2B_2C$.* Physica C **230**, 397–406 (1994).

[20] B. K. Cho, Ming Xu, P. C. Canfield, L. L. Miller and D. C. Johnston. *Magnetic and superconducting properties of single-crystal $TmNi_2B_2C$.* Phys. Rev. B **52** (5), 3676–3683 (Aug 1995).

[21] A. Kreyssig, O. Stockert, D. Reznik, F. M. Woodward, J. W. Lynn, H. Bitterlich, D. Souptel, G. Behr and M. Loewenhaupt. *Magnetic excitations of RNi_2B_2C single crystals with R =Tb and Ho.* Physica C **408-410**, 100–101 (2004).

[22] A. Kreyssig, O. Stockert, D. Reznik, F. M. Woodward, J. W. Lynn, H. Bitterlich, D. Souptel, G. Behr and M. Loewenhaupt. *Low-energy phonons in $TbNi_2B_2C$ and $HoNi_2B_2C$.* Physica B **350**, 69–71 (2004).

[23] P. Dervenagas, M. Bullock, J. Zarestky, P. C. Canfield, B. K. Cho, B. Harmon, A. I. Goldman and C. Stassis. *Soft phonons in superconducting $LuNi_2B_2C$.* Phys. Rev. B **52**, R9839 (1995).

[24] H. Kawano, H. Yoshizawa, H. Takeya and K. Kadowaki. *Anomalous phonon scattering below T_c in $YNi_2{}^{11}B_2C$.* Phys. Rev. Lett. **77**, 4628 (1996).

[25] C. Stassis, M. Bullock, J. Zarestky, P. Canfield and A. Goldman. *Phonon mode coupling in superconducting $LuNi_2B_2C$.* Phys. Rev. B **55**, R8678 (1997).

[26] H. Kawano, H. Yoshizawa, H. Takeya and K. Kadowaki. *Anomalous phonon properties in the intermetallic superconductor $YNi_2{}^{11}B_2C$.* Physica B **241-243**, 874–876 (1998).

[27] M. Bullock, C. Stassis, J. Zarestky, A. Goldman, P. C. Canfield, G. Shirane and S. Shapiro. *Inelastic neutron studies of the low-energy phonon excitations in the $ReNi_2B_2C$ superconductors (RE=Lu,Y,Ho,Er).* Physica B **241-243**, 798–801 (1998).

[28] C. Stassis, J. Zarestky, A. Goldman, P. Canfield, G. Shirane and S. Shapiro. *Anomalous phonons below Tc in superconducting RNi_2B_2C (R=Lu,Y).* Physica C **317-318**, 127–133 (1999).

[29] H. Kawano, H. Yoshizawa, H. Takeya and K. Kadowaki. *Anomalous phonon peak in the superconducting state of $ErNi_2{}^{11}B_2C$.* Phys. Rev. B **66**, 212503 (2002).

[30] H. Kawano-Furukawa, H. Takeshita, M. Ochiai, T. Nagata, H. Yoshizawa, N. Furukawa, H. Takeya and K. Kadowaki. *Weak ferromagnetic order in the superconducting $ErNi_2{}^{11}B_2C$.* Phys. Rev. B **65**, R180508 (2002).

[31] F. Gompf, W. Reichardt, H. Schober, B. Renker and M. Buchgeister. *Lattice vibrations and electron-phonon coupling in superconducting quarternary borocarbides: An inelastic neutron-scattering investigation.* Phys. Rev. B **55**, 9058 (1997).

[32] W. Reichardt, R. Heid and K.-P. Bohnen. *Phonons and electron-phonon coupling in nickel borocarbides.* J. Superconductivity **74**, 0896–1107 (2005).

[33] M. J. Cooper and R. Nathans. *The resolution function in neutron diffractometry. I. The resolution function of a neutron diffractometer and its application to phonon measurements.* Acta Crystallographica **23** (3), 357–367 (Sep 1967).

[34] D. R. Sanchez, H. Micklitz and E. M. Baggio-Saitovitch. *Influence of structural parameters on T_c in superconducting RNi_2B_2C compounds.* Phys. Rev. B **71** (2), 024509 (2005).

[35] L. F. Matheiss, T. Siegrist and R. J. Cava. *Superconductivity in the $LnNi_2B_2C$ intermetallics via boron A_{1g} phonons.* Solid State Commun. **91**, 587 (1994).

[36] V. G. Hadjiev, L. N. Bozukov and M. G. Baychev. *Raman scattering from phonons in YNi_2B_2C.* Phys. Rev. B **50** (22), 16726–16728 (Dec 1994).

[37] Hyun-Jung Park, Hye-Soo Shin, Hye-Gyong Lee, In-Sang Yang, W. C. Lee, B. K. Cho, P. C. Canfield and D. C. Johnston. *Raman modes of RNi_2B_2C (R=Lu, Ho, Y) single crystals.* Phys. Rev. B **53** (5), 2237–2240 (Feb 1996).

[38] J. Hartmann, F. Gompf and B. Renker. *Micro-Raman scattering investigations on borocarbides.* J. Low Temp. Phys. **105** (5), 1629 (Mar 1996).

[39] Stefano Baroni, Stefano de Gironcoli, Andrea Dal Corso and Paolo Giannozzi. *Phonons and related crystal properties from density-functional perturbation theory.* Rev. Mod. Phys. **73** (2), 515–562 (Jul 2001).

[40] R. Heid and K.-P. Bohnen. *Linear response in a density-functional mixed-basis approach.* Phys. Rev. B **60** (6), R3709–R3712 (Aug 1999).

[41] R. Heid, K.-P. Bohnen and Renker. *Electron-phonon coupling and superconductivity in MgB_2 and related diborides.* Adv. Solid State Phys. **42**, 293 (2002).

[42] P. Hohenberg and W. Kohn. *Inhomogeneous Electron Gas.* Phys. Rev. **136**, B864–B871 (Nov 1964).

[43] W. Kohn and L. J. Sham. *Self-Consistent Equations Including Exchange and Correlation Effects.* Phys. Rev. **140** (4A), A1133–A1138 (Nov 1965).

[44] Stefano Baroni, Paolo Giannozzi and Andrea Testa. *Green's-function approach to linear response in solids.* Phys. Rev. Lett. **58** (18), 1861–1864 (May 1987).

[45] Andrew A. Quong and Barry M. Klein. *Self-consistent-screening calculation of interatomic force constants and phonon dispersion curves from first principles.* Phys. Rev. B **46** (17), 10734–10737 (Nov 1992).

[46] Stefano de Gironcoli. *Lattice dynamics of metals from density-functional perturbation theory.* Phys. Rev. B **51** (10), 6773–6776 (Mar 1995).

[47] K.-P. Bohnen, R. Heid and M. Krauss. *Phonon dispersion and electron-phonon interaction for $YBa_2Cu_3O_7$ from first-principles calculations.* Europhysics Letters **64**, 104–110 (2003).

[48] W. Reichardt, R. Heid and K.-P. Bohnen. *Ab-initio lattice dynamics and electron-phonon coupling in borocarbides.* unpublished.

[49] P. B. Allen and R. C. Dynes. *Transition temperature of strong-coupled superconductors reanalyzed.* Phys. Rev. B **12** (3), 905–922 (Aug 1975).

[50] Joo Yull Rhee, Xindong Wang and B. N. Harmon. *Generalized susceptibility and magnetic ordering in rare-earth nickel boride carbides.* Phys. Rev. B **51** (21), 15585–15587 (Jun 1995).

[51] W. Reichardt. private Communication.

[52] J. D. Axe and G. Shirane. *Influence of the superconducting energy gap on phonon linewidths in Nb_3Sn.* Phys. Rev. Lett. **30**, 214 (1973).

[53] P. B. Allen, V. N. Kostur, N. Takesue and G. Shirane. *Neutron-scattering profile of $Q \neq 0$ phonons in BCS superconductors.* Phys. Rev. B **56**, 5552 (1997).

[54] P. B. Allen. *Neutron spectroscopy of superconductors.* Phys. Rev. B **6**, 2577 (1972).

[55] P. B. Allen and M. L. Cohen. *Superconductivity and phonon softening.* Phys. Rev. Lett. **29**, 1593 (1972).

[56] W. H. Butler, F. J. Pinski and P.B. Allen. *Phonon linewidths and electron-phonon interaction in Nb.* Phys. Rev. B **19**, 3708 (1972).

[57] M. Iavarone, G. Karapetrov, A. E. Koshelev, W. K. Kwok, G. W. Crabtree, D. G. Hinks, W. N. Kang, Eun-Mi Choi, Hyun Jung Kim, Hyeong-Jin Kim and S. I. Lee. *Two-Band Superconductivity in MgB_2.* Phys. Rev. Lett. **89** (18), 187002 (Oct 2002).

[58] S.V. Shulga, S.-L. Drechsler, G. Fuchs, K.-H. Mueller, K. Winzer, M. Heinecke and K. Krug. *Upper critical field peculiarities of superconducting YNi_2B_2C and $LuNi_2B_2C$.* Phys. Rev. Lett. **80**, 1730 (1998).

[59] M. Nohara, M. Isshiki, H. Takagi and R. J. Cava. *Magnetic field dependence of the low-temperature specific heat of the borocarbide superconductor $LuNi_2B_2C$.* J. Phys. Soc. Japan **66**, 1888–1891 (1997).

[60] Minoru Nohara, Masanobu Isshiki, Fumiko Sakai and Hidenori Takagi. *Quasiparticle Density of States of Clean and Dirty s-Wave Superconductors in the Vortex State.* J. Phys. Soc. Japan **68**, 1078–1081 (1999).

[61] T. Park, M. B. Salamon, E. M. Choi, H. J. Kim and S.-I. Lee. *Evidence for nodal quasiparticles in the nonmagnetic superconductor YNi_2B_2C via field-angle-dependent heat capacity.* Phys. Rev. Lett. **90**, 177001 (2003).

[62] E. Boaknin, R. W. Hill, C. Proust, C. Lupien, L. Taillefer and P. C. Canfield. *Highly anisotropic gap functions in borocarbide superconductor $LuNi_2B_2C$.* Phys. Rev. Lett. **87**, 237001 (2001).

[63] T. Terashima, C. Haworth, H. Takeya, S. Uji, H. Aoki and K. Kadowaki. *Small superconducting gap on part of the Fermi surface of YNi_2B_2C from the de Haas−van Alphen effect.* Phys. Rev. B **56** (9), 5120–5123 (Sep 1997).

[64] H. Nishimori, K. Uchiyama, S. Kaneko, A. Tokura, H. Takeya, K. Hirata and N Nishida. *First Observation of the Fourfold-symmetric and Quantum Regime Vortex Core in YNi_2B_2C by Scanning Tunneling Microscopy and Spectroscopy.* J. Phys. Soc. Japan **73**, 3247–3250 (2004).

[65] Kazumi Maki. *Quantum oscillation in vortex states of type-II superconductors.* Phys. Rev. B **44** (6), 2861–2862 (Aug 1991).

[66] M. J. Stephen. *Superconductors in strong magnetic fields: de Haas−van Alphen effect.* Phys. Rev. B **45** (10), 5481–5485 (Mar 1992).

[67] T. Ekino, M. Kosugi H. Fuji and, Y. Zenitani and J. Akimitsu. *Superconducting energy gap in YNi_2B_2C.* Physica C **235-240**, 2529–2530 (1994).

[68] I. Vekhter, P. J. Hirschfeld, J. P. Carbotte and E. J. Nicol. *Anisotropic thermodynamics of d-wave superconductors in the vortex state.* Phys. Rev. B **59** (14), R9023–R9026 (Apr 1999).

[69] D. L. Bashlakov, Yu. G. Naidyuk, I. K. Yanson, G. Behr, S.-L. Drechsler, G. Fuchs, L. Schultz and D. Souptel. *Point-contact spectroscopy of the borocarbide superconductor YNi_2B_2C in the normal and superconducting state.* J. Low Temp. Phys. **147**, 335 (2007).

[70] R. Heid. private communication.

[71] J. G. Bednorz and K. A. Müller. *Possible high-T_c superconductivity in the La - Ba - Cu - O system.* Zeitschrift für Physik B: Condens. Matter **64**, 189 (1986).

[72] R. van Helmholt, J. Wecker, B. Holzapfel, L. Schultz and K. Samwer. *Giant negative magnetoresistance in perovskitelike $La_{2/3}Ba_{1/3}MnO_x$ ferromagnetic films.* Phys. Rev. Lett. **71**, 2331 (1993).

[73] S. Jin, T. H. Tiefel, M. McCormack, R. A. Fastnacht, R. Ramesh and L. H. Chen. *Thousandfold Change in Resistivity in Magnetoresistive La-Ca-Mn-O Films.* Science **264**, 413–415 (1994).

[74] T. Venketesan, M. Rajeswari, Z.-W. Dong, S. B. Ogale and R. Ramesh. *Manganite-based devices: opportunities, bottlenecks and challenges.* Phil. Trans. R. Soc. Lond. A **356**, 1661 (1998).

[75] C. Zener. *Interaction between the d shells in the transition metals.* Phys. Rev. **81**, 440 (1951).

[76] C. Zener. *Interaction between the d shells in the transition metals. II. Ferromagnetic compounds of manganese with perovskite structure.* Phys. Rev. **82**, 403 (1951).

[77] P. W. Anderson and H. Hasegawa. *Considerations on double exchange.* Phys. Rev. **100**, 675 (1955).

[78] P.-G. de Gennes. *Effects of double-exchange in magnetic crystals.* Phys. Rev. **118**, 141 (1960).

[79] A. J. Millis, P. B. Littlewood and B. I. Shraiman. *Double exchange alone does not explain the resistivity of $La_{1-x}Sr_xMnO_3$.* Phys. Rev. Lett. **74**, 5144 (1995).

[80] A. J. Millis, R. Mueller and B. I. Shraiman. *Dynamic Jahn-Teller effect and colossal magnetoresistance in $La_{1-x}Sr_xMnO_3$.* Phys. Rev. Lett. **77**, 175 (1996).

[81] J. F. Mitchell, D. N. Argyriou, A. Berger, K. E. Gray, R. Osborn and U. Welp. *Spin, charge, and lattice states in layered magnetoresistive oxides.* J. Phys. Chem. B **105**, 10731 (2001).

[82] A. Urushibara, Y. Moritomo, T. Arima, A. Asamitsu, G. Kido and Y. Tokura. *Insulator-metal transition and giant magnetoresistance in* $La_{1-x}Sr_xMnO_3$. Phys. Rev. B **51**, 14103 (1995).

[83] X. J. Chen, C. L. Zhang, C. C. Almasan, J. S. Gardner and J. L. Sarrao. *Small-polaron hopping conduction in bilayer manganite* $La_{1.2}Sr_{1.8}Mn_2O_7$. Phys. Rev. B **67**, 094426 (2003).

[84] Y. Moritomo, A. Asamitsu, H. Kuwahara and Y. Tokura. *Giant magnetoresistance of manganese oxides with a layered perovskite structure.* Nature **380**, 141–144 (1996).

[85] P. Schiffer, A. P. Ramirez, W. Bao and S.-W. Cheong. *Low temperature magnetoresistance and the magnetic phase diagram of* $La_{1-x}Ca_xMnO_3$. Phys. Rev. Lett. **75**, 3336 (1995).

[86] Y. Tokura. *Collossal magnetoresistive oxides.* Gordon and Breach science publishers 2000.

[87] A. J. Millis. *Lattice effects in magnetoresistive manganese provskites.* Nature **392**, 147–150 (1998).

[88] D. M. Edwards. *Ferromagnetism and electron-phonon coupling in the manganites.* Adv. Phys. **51**, 1259 (2002).

[89] A. C. M. Green. *Many-body CPA for the Holstein double-exchange model.* Phys. Rev. B **63** (20), 205110 (May 2001).

[90] P. Dai, J. Zhang, H. A. Mook, S.-H. Liou, P. A. Dowben and E. W. Plummer. *Experimental evidence for the dynamic Jahn-Teller effect in* $La_{0.65}Ca_{0.35}MnO_3$. Phys. Rev. B **54**, R3694 (1996).

[91] P. G. Radaelli, G. Iannone, M. Marezio, H. Y. Hwang, S.-W. Cheong, J. D. Jorgensen and D. N. Argyriou. *Structural effects on the magnetic and transport properties of perovskite* $A_{1-x}A'_xMnO_3$ *(x=0.25, 0.30).* Phys. Rev. B **56**, 8265 (1997).

[92] D. N. Argyriou, H. N. Bordallo, J. F. Mitchell, J. D. Jorgensen and G. F. Strouse. *Lattice displacements above* T_c *in the layered manganite* $La_{1.2}Sr_{1.8}Mn_2O_7$. Phys. Rev. B **60**, 6200 (1999).

[93] Th. Proffen, R. G. DiFrancesco, S. J. L. Billinge, E. L. Brosha and G. H. Kwei. *Measurement of the local Jahn-Teller distortion in* $LaMnO_{3.006}$. Phys. Rev. B **60**, 9973 (1999).

[94] Q. Li, K. E. Gray, H. Zheng, H. Claus, S. Rosenkranz, S. Nyborg Ancona, R. Osborn, J. F. Mitchell, Y. Chen and J. W. Lynn. *Reentrant Orbital Order and the True Ground State of* $LaSr_2Mn_2O_2$. Phys. Rev. Lett. **98** (16), 167201 (2007).

[95] J. B. Goodenough. *Theory of the role of covalence in the perovskite-type manganites* $La_{1-x}M(II)_xMnO_3$. Phys. Rev. **100**, 564 (1955).

[96] E. O. Wollan and W. C. Koehler. *Neutron diffraction study of the magnetic properties of the series of perovskite-type compounds* $La_{1-x}Ca_xMnO_3$. Phys. Rev. **100**, 545 (1955).

[97] Y. Tomioka, A. Asamitsu, H. Kuwahara, Y. Moritomo and Y. Tokura. *Magnetic-field-induced metal-insulator phenomena in* $Pr_{1-x}Ca_xMnO_3$ *with controlled charge-ordering instability.* Phys. Rev. B **53** (4), R1689–R1692 (Jan 1996).

[98] H. Kawano, R. Kajimoto, H. Yoshizawa, Y. Tomioka, H. Kuwahara and Y. Tokura. *Magnetic Ordering and Relation to the Metal-Insulator Transition in* $Pr_{1-x}Sr_xMnO_3$ *and* $Nd_{1-x}Sr_xMnO_3$ *with* $x \approx 0.5$. Phys. Rev. Lett. **78** (22), 4253–4256 (Jun 1997).

[99] B. G. Dick and A. W. Overhauser. *Theory of the Dielectric Constants of Alkali Halide Crystals.* Phys. Rev. **112** (1), 90 (Oct 1958).

[100] P. Brüesch. *Phonons: Theory and Experiments I.* Solid-state sciences 34. Springer-Verlag 1982.

[101] M. Jaime, P. Lin, M. B. Salamon and P. D. Han. *Low-temperature electrical transport and double exchange in* $La_{0.67}(Pb,Ca)_{0.33}MnO_3$. Phys. Rev. B **58** (10), R5901–R5904 (Sep 1998).

[102] K. Hirota, S. Ishihara, H. Fujioka, M. Kubota, H. Yoshizawa, Y. Moritomo, Y. Endoh and S. Maekawa. *Spin dynamical properties and orbital states of the layered perovskite* $La_{2-2x}Sr_{1+2x}Mn_2O_7$ *(*$0.3 \leq x < 0.5$*).* Phys. Rev. B **65** (6), 064414 (Jan 2002).

[103] J. van den Brink, P. Horsch and A. M. Oleś. *Photoemission Spectra of* $LaMnO_3$ *Controlled by Orbital Excitations.* Phys. Rev. Lett. **85** (24), 5174–5177 (Dec 2000).

[104] E. Saitoh, S. Okamoto, K. T. Takahashi, K. Tobe, K. Yamamoto, T. Kimura, S. Ishihara, S. Maekawa and Y. Tokura. *Observation of orbital waves as elementary excitations in a solid.* Nature **410**, 180 (2001).

[105] W. Reichardt and M. Braden. *Anomalous features in the bond stretching vibrations of* $La_{1-x}Sr_xMnO_3$. Physica B **263-264**, 416 (1999).

[106] D. Reznik and W. Reichardt. *Bond-bendig and bond-stretching phonons in ferromagnetic* $La_{0.7}Sr_{0.3}MnO_3$. Phys. Rev. B **71**, 092301 (2005).

[107] J. Zhang, P. Dai, J. A. Fernandez-Baca, E. W. Plummer, Y. Tomioka and Y. Tokura. *Jahn-Teller phonon anomaly and dynamic phase fluctuations in* $La_{0.7}Ca_{0.3}MnO_3$. Phys. Rev. Lett. **86**, 3823 (2001).

[108] W. Reichardt and M. Braden. unpublished.

[109] L. Pintschovius, D. Reznik and K. Yamada. *Oxygen phonon branches in overdoped* $La_{1.7}Sr_{0.3}CuO_4$. Phys. Rev. B **74** (17), 174514 (2006).

[110] D. Reznik, L. Pintschovius, M. Ito, S. Iikubo, M. Sato, H. Goka, M. Fujita, K. Yamada, G. D. Gu and J. M. Tranquada. *Electron-phonon coupling reflecting dynamic charge inhomogeneity in copper oxide superconductors.* Nature **440**, 1170 (2006).

[111] Z. Sun, Y.-D. Chuang, A. V. Fedorov, J. F. Douglas, D. Reznik, F. Weber, N. Aliouane, D. N. Argyriou, H. Zheng, J. F. Mitchell, T. Kimura, Y. Tokura, A. Revcolevschi and D. S. Dessau. *Quasiparticlelike peaks, kinks, and electron-phonon coupling in the* $(\pi, 0)$ *regions in the CMR oxide* $La_{2-2x}Sr_{1+2x}Mn_2O_7$. Phys. Rev. Lett. **97**, 056401 (2006).

[112] T. Cuk, D. H. Lu, X. J. Zhou, Z.-X. Shen, T. P. Devereaux and N. Nagaosa. *A review of electron-phonon coupling seen in the high-*T_c *superconductors by angle-resolved photoemission studies (ARPES).* phys. stat. sol. (b) **242**, 11–29 (2005).

[113] D. S. Dessau, T. Saitoh, C.-H. Park, Z.-X. Shen, P. Villella, N. Hamada, Y. Moritomo and Y. Tokura. *k-dependent elctronic structure, a large 'ghost' Fermi surface, and a pseudogap in a layered magnetoresistive oxide.* Phys. Rev. Lett. **81**, 192 (1998).

[114] T. Saitoh, D. S. Dessau, Y. Moritomo, T. Kimura, Y. Tokura and N. Hamada. *Temperature-dependent pseudogaps in colossal magnetoresistive oxides.* Phys. Rev. B **62** (2), 1039–1043 (Jul 2000).

[115] N. Manella, W. L. Yang, X. J. Zhou, H. Zheng, J. F. Mitchell, J. Zaanen, T. P. Devereaux, N. Nagaosa, Z. Hussain and Z. X. Shen. *Nodal quasiparticles in pseudogapped colossal magnetoresistive manganites.* Nature **438**, 474 (2005).

[116] M. Braden, W. Reichardt, S. Shiryaev and S. N. Barilo. *Giant phonon anomalies in the bond-stretching modes in doped* $BaBiO_3$*: comparison to cuprates, manganites and nickelates.* Physica C **378-381**, 89–96 (2002).

[117] I. Guedes, J. F. Mitchell, D. Argyriou and M. Grimsditch. *Raman phonons in* $La_{2-2x}Sr_{1+2x}Mn_2O_7$. Journal of Raman Spectroscopy **31**, 1013–1015 (2000).

[118] L. Vasiliu-Doloc, S. Rosenkranz, R. Osborn, S. K. Sinha, J. W. Lynn, J. Mesot, O. H. Seeck, G. Preosti, A. J. Fedro and J. F. Mitchell. *Charge melting and polaron collapse in* $La_{1.2}Sr_{1.8}Mn_2O_7$. Phys. Rev. Lett. **83**, 4393 (1999).

[119] D. N. Argyriou, J. W. Lynn, R. Osborn, B. Campbell, J. F. Mitchell, U. Ruett, H. N. Bordallo, A. Wildes and C. D. Ling. *Glass transition in the polaron dynamics of colossal magnetoresisitive manganites.* Phys. Rev. Lett. **89**, 036401 (2002).

[120] D. N. Argyriou. *private communication.*

[121] Z. Sun, J. F. Douglas, A. V. Federov, Y.-D. Chuang, H. Zheng, J. F. Mitchell and D. S. Dessau. *A local metallic state in globally insulating $La_{1.24}Sr_{1.76}Mn_2O_7$ well above the metalinsulator transition.* nature physics **3**, 248 (2007).

[122] F. Weber, D. N. Argyriou, O. Prokhnenko and D. Reznik. *Reduction of lattice coherence associated with the magnetic transition uncorrelated with the magnitude of magnetoresistance in ferromagnetic manganites.* will be published soon.

[123] Juan Rodriguez-Carvajal. *FULLPROF.* Technical report Laboratoire Léon Brillouin, CE Saclay, France 2001.

[124] P. Dai, H. Y. Hwang, J. Zhang, J. A. Fernandez-Baca, S.-W. Cheong, C. Kloc, Y. Tomioka and Y. Tokura. *Magnon damping by magnon-phonon coupling in manganese perovskite.* Phys. Rev. B **61**, 9553 (2000).